

CHARACTERIZATION AND MODELING OF THE EFFECT OF ENVIRONMENTAL
DEGRADATION ON FLEXURAL STRENGTH OF
CARBON/EPOXY COMPOSITES

by

SNEHA ANIL CHAWLA

A THESIS

Submitted in partial fulfillment of the requirements
for the degree of Master of Science
in the Department of Aerospace Engineering
in the Graduate School of
The University of Alabama

TUSCALOOSA, ALABAMA

2009

Copyright Sneha Anil Chawla 2009
ALL RIGHTS RESERVED

ABSTRACT

A mechanism-based modeling methodology has developed for prediction of long-term durability of composites for emerging facilities in different climatic zones. The objective of the research was to develop a predictive tool using the Arrhenius principles adapted to the TTS (Time Temperature Superposition) to measure degradation of carbon-fiber/epoxy composite under hygrothermal exposure and applied tensile stress. The hygrothermal conditions capture the synergistic effects of field exposure and extreme temperatures, viz., hot/dry, hot/wet, cold/dry, and cold/wet. Short term tests were performed to determine the flexural strength of environmentally aged composite specimens in accordance with ASTM D2344-84 and ASTM D7264 respectively. Carbon/epoxy specimens of $[0_2/90_2]_{2s}$ configuration were manufactured for flexure tests using Vacuum Assisted Resin Transfer Molding (VARTM). A unique strain fixture was designed to apply constant strain on the specimens during ageing and applied a simple methodology to eliminate excessive creep in the specimens.

A two-dimensional cohesive layer constitutive model with a cubic traction-separation law has being developed in order to predict the life of the composite under hygrothermal conditions. The model simulated the test conditions and predicted the progressive failure mechanism of the specimen as observed in the tests, under various loading conditions. The model also incorporated synergistic interactions between temperature, moisture and stress effects and predicted degradation in strength and stiffness as a function of different ageing conditions and ageing

times. Model predictions have been benchmarked using test data.

DEDICATION

This thesis is dedicated to everyone who helped me and guided me through the trials and tribulations of creating this manuscript. In particular, my family and close friends who stood by me throughout the time taken to complete this masterpiece.

LIST OF ABBREVIATIONS AND SYMBOLS

ASTM	American Society of Testing of Materials
CDS	Cold Dry Stressed
CDU	Cold Dry Unstressed
CERL	Construction Engineering Research Laboratory
CFRP	Carbon Fiber Reinforced Polymer
CWS	Cold Wet Stressed
CWU	Cold Wet Unstressed
ERDC	Engineer Research Development Center
FE	Finite Element
FEA	Finite Element Analysis
FRP	Fiber Reinforced Polymer
HDS	Hot Dry Stressed
HDU	Hot Dry Unstressed
HWS	Hot Wet Stressed
HWU	Hot Wet Unstressed
kips	kilo pounds
MPa	Mega Pascal
PC	Personal Computer
RVE	Representative Volume Element

SCET	Stress coupled Exposure Test
SQRT	Square Root
STTR	Small Business Technology Transfer
TTS	Time Temperature Superposition
UTTS	Ultimate Tensile Transverse Strength
VARTM	Vacuum Assisted Resin Transfer Molding
γ_{\max}	Maximum shear strain of lamina at initial failure
$\epsilon_{\max C}$	Maximum longitudinal compressive strain of lamina at initial failure
$\sigma_{\max C}$	Maximum longitudinal compressive strength of lamina
$\epsilon_{\max T}$	Maximum longitudinal tensile strain of lamina at initial failure
$\sigma_{\max T}$	Maximum longitudinal tensile strength of lamina
τ_{\max}	Maximum shear strength of lamina

ACKNOWLEDGEMENTS

I would like to thank all the people who have helped and inspired me during my Master's program.

Foremost, I would like to express my sincere gratitude to my advisor, Dr. Samit Roy, for his continuous support during my Master's study and research at the University of Alabama. His perpetual energy and enthusiasm in research along with his patience and immense knowledge motivated me tremendously. In addition, he was always accessible and willing to help with my research work. I could not have imagined having a better advisor and mentor for my Master's study.

I was delighted to have Dr. Anwarul Haque as my co-advisor. His insights into composite manufacturing and experimental procedures enabled me to overcome many hurdles in the experimental stage of my research.

I would also like to thank Dr. Jialai Wang for serving on my committee and providing me with insightful inputs and comments.

My sincere appreciation goes out to everyone in the engineering services department, and in particular Ken Dunn, Jim Edmonds, Sam Tingle, James Yarbrough for their help in cutting the specimens and manufacturing the stress fixtures and Tim Connell for all his help in setting up the equipment and electrical supply and a number of miscellaneous tasks that I could not have completed without his help.

In addition, I would like extend my gratitude to the entire faculty and staff in the Aerospace Engineering Department at the University of Alabama for their assistance in my course work and research.

I also want to thank the U.S. Army and Dutta Technologies Inc. for providing us with the project and Dr. Piyush Dutta for helping me through important steps of drafting the report.

This thesis would not have been possible without the help and guidance I received from my fellow colleagues-Abilash Nair, Sushil Singh, Avinash Akepatti, Kameshwaran Narasimhan and Rezwanur Rahman for the stimulating discussions, for the sleepless nights we were working together before deadlines, and for all the fun we have had in the last two years.

And finally, I would like to thank my family and friends for their undying love and support through my entire Master's program without which this would not have been possible.

CONTENTS

ABSTRACT.....	ii
DEDICATION.....	iv
LIST OF ABBREVIATIONS AND SYMBOLS	v
ACKNOWLEDGEMENTS	vii
LIST OF TABLES	xii
LIST OF FIGURES	xiv
1. INTRODUCTION	1
2. LITERATURE REVIEW	4
2.1 Influence of Moisture	5
2.1.1 Moisture Absorption	6
2.1.2 Effect on Static Strength and Stiffness	8
2.1.3 Effect of Tensile Properties	8
2.2 Influence of Temperature	8
2.2.1 Effect of Elevated Temperature on Strength and Stiffness	8
2.2.2 Effect of Low Temperature	10
2.3 Influence of Moisture/Temperature Interaction	11
2.4 Influence of Environment on Flexural Strength and Modulus	12

3. ENVIRONMENTAL AGEING AND MECHANICAL TESTING	13
3.1 Fabrication of Specimens	14
3.1.1 Materials	14
3.1.2 VARTM Process	16
3.2 Accelerated Environmental Ageing	18
3.2.1 Panel Description	18
3.2.2 Environmental Conditions	19
3.2.3 Constant Strain Aging Test Fixture	21
3.3 Test Method	24
3.3.1 Test Specimen Description	24
3.3.2 Test Description	26
3.3.3 Flexural strength determination	27
4 MODELING	29
4.1 Cohesive Layer Modeling	29
4.2 Mechanism-based Micromechanics Model	31
4.3 Multi-scale Mechanism Based Model Development	34
4.3.1 Cohesive Layer Approach	34
4.3.2 General Framework for Modeling Damage and Failure	35
4.4 Modeling Procedure	36
4.4.1 Specimen Geometry and Mesh Generation	36
4.4.2 Boundary Conditions	39
4.4.3 Elastic Material Properties	40
4.4.4 Cohesive material Properties	40

4.4.5 Cohesive Layer Constitutive Equations	41
4.5 Direct Micromechanical model for 3-D Local Strains from 2-D Global Strains	45
4.5.1 Boundary Conditions of Hexagonal Unit Cell	47
5 EXPERIMENTAL RESULTS AND DISCUSSIONS	49
5.1 Environmental Ageing	49
5.1.1 Moisture Desiccation	49
5.1.2 Moisture Absorption	50
5.2 Test Results	53
6 MODEL CALIBRATION AND BENCHMARKING	67
6.1 Modeling Results	67
6.1.1 Control Specimens	67
6.1.2 Aged Specimens	71
6.2 Results and Discussions	86
7 SUMMARY AND CONCLUSIONS	90
7.1 Experimental Conclusions	91
7.2 Modeling Conclusions	92
7.3 Summary	92
REFERENCES	94

LIST OF TABLES

3.1	Test matrix for accelerated ageing of cross ply flexure specimen.....	14
3.2	Test Specimen Nomenclature and number of panels required	20
3.3	Ageing time for flexure specimens	21
3.4	Number of specimens aged using the constant strain fixture	24
3.5	Number of test specimens for each condition.....	25
4.1	Load and displacement values for different mesh sizes.....	38
4.2	Periodic boundary conditions for the hexagonal unit cell for the application of unit magnitude of various strain components.....	47
4.3	Local 3D strains at three critical locations (1, 2, 3) from periodic boundary conditions .	48
5.1	Diffusivity and M_{inf} from Ficks law fit.....	51
5.2	Flexural strength of specimens tested at ageing time t_1 and displacement rate R_1	64
5.3	Flexural strength of specimens tested at ageing time t_2 and displacement rate R_1	65
5.4	Flexural strength of specimens tested at ageing time t_3 and displacement rate R_1	65
5.5	Flexural strength of specimens tested at ageing time t_1 and displacement rate R_2	65
5.6	Flexural strength of specimens tested at ageing time t_2 and displacement rate R_2	65
5.7	Flexural strength of specimens tested at ageing time t_3 and displacement rate R_2	66
5.8	Experimental strains at initial failure at R_1	66
5.9	Experimental strains at initial failure at R_2	66
6.1	Cohesive layer parameters for control flexure test simulation at R_1	68
6.2	Cohesive layer parameters for control flexure test simulation at R_2	70

6.3	Cohesive layer parameters for ageing time ‘ t_1 ’ for control flexure test simulation at R_1 .	72
6.4	Cohesive layer parameters for ageing time ‘ t_2 ’ for flexure test simulation at R_1	72
6.5	Cohesive layer parameters for ageing time ‘ t_3 ’ for flexure test simulation at R_1	73
6.6	Cohesive layer parameters for ageing time ‘ t_1 ’ for flexure test simulation at R_2	79
6.7	Cohesive layer parameters for ageing time ‘ t_2 ’ for flexure test simulation at R_2	80
6.8	Cohesive layer parameters for ageing time ‘ t_3 ’ for flexure test simulation at R_2	80
6.9	Comparison of experimental and NOVA-3D deflection at peak load for flexure test simulation at R_1	86
6.10	Comparison of experimental and NOVA-3D deflection at peak load for flexure test simulation at R_2	86
6.11	Comparison of experimental and NOVA-3D peak load of flexure test simulation at R_1 ..	87
6.12	Comparison of experimental and NOVA-3D peak load of flexure test simulation at R_2 ..	87
6.13	Comparison of experimental and NOVA-3D strains at initial failure of flexure test simulation at R_1	89
6.14	Comparison of experimental and NOVA-3D strains at initial failure of flexure test simulation at R_2	89

LIST OF FIGURES

1.1	Modeling and testing approach.....	2
2.1	Agents of composite degradation.....	4
2.2	Moisture Absorption by polymer composites.....	7
3.1	(a) Carbon fiber (b) Resin and hardener	16
3.2	Schematic of the VARTM setup.....	16
3.3	Actual VARTM setup	17
3.4	Unique constant strain fixture.....	19
3.5	Flexural Stress-coupled test fixture	22
3.6	Test specimens obtained from aged panel	25
3.7	Loading diagram for three-point bend test.....	26
3.8	Experimental setup for three-point bend test.....	27
4.1	Cubic cohesive traction-separation law	30
4.2	RVE of Micromechanics Model for Fiber-Matrix Degradation Simulation	32
4.3	Simulated stiffness and strength degradation with ageing time.....	34
4.4	Diffusion on flexure model for $[0_2/90_2]_{2s}$ laminated composite	34
4.5	Cubic traction-separation law	35
4.6	Partitioning of flexure specimen along length.....	36
4.7	Partitioning of flexure specimen in thickness direction.....	37
4.8	FEA macro-model of flexure specimen.....	38
4.9	Convergence study with different mesh sizes.....	39

4.10	Schematic of $[0_2/90_2]_{2s}$ specimen.....	40
4.11	2-D RVE for $[90]$ layer	42
4.12	2-D RVE for $[0]$ layer	44
4.13	Hexagonal packing and corresponding FEM mesh	46
4.14	Hexagonal unit cell 3-D mesh.....	46
4.15	Geometry of square and hexagonal unit cells	48
5.1	Desiccation of cross-ply flexure specimens.....	49
5.2	Moisture absorption of unstressed cross-ply flexure specimens.....	50
5.3	Moisture absorption of stressed cross-ply flexure specimens.....	51
5.4	Ficks law fit for HWU and CWU panels	52
5.5	Ficks law fit for HWS and CWS panels	52
5.6	Failed specimen	53
5.7	Comparison of R_1 and R_2 for ' t_1 ' testing of flexure specimens	55
5.8	Comparison of R_1 and R_2 for ' t_2 ' testing of flexure specimens	56
5.9	Comparison of R_1 and R_2 for ' t_3 ' testing of flexure specimens.....	56
5.10	Flexural strength degradation with time for $R_1=0.01$ in/min.....	57
5.11	Flexural strength degradation with time for $R_2=1.00$ in/min.....	57
5.12	Load-Deflection curves (a) CF00- R_1 (b) CF00- R_2 (c) HWU1- R_1 (d) HWU1- R_2 (e) CWU1- R_1 (f) CWU1- R_2	59
5.13	Load-Deflection curves (a) HWS1- R_1 (b) HWS1- R_2 (c) CWS1- R_1 (d) CWS1- R_2 (e) HDS1- R_1 (f) HDS1- R_2	60
5.14	Load-Deflection curves (a) CDS1- R_1 (b) CDS1- R_2 (c) HWU2- R_1 (d) HWU2- R_2 (e) CWU2- R_1 (f) CWU2- R_2	61

5.15	Load-Deflection curves (a) HDU2-R ₁ (b) HDU2-R ₂ (c) CDU2-R ₁ (d) CDU2-R ₂ (e) HDS2-R ₁ (f) HDS2-R ₂	62
5.16	Load-Deflection curves (a) CDS2-R ₁ (b) CDS2-R ₂ (c) HWU3-R ₁ (d) HWU3-R ₂ (e) HDU3-R ₁ (f) HDU3-R ₂	63
5.17	Load-Deflection curves (a) HDS3-R ₁ (b) HDS3-R ₂ (c) CDS3-R ₁ (d) CDS3-R ₂	64
6.1	Experimental and NOVA-3D load-displacement curve for control flexure specimen at R ₁	69
6.2	NOVA-3D contour plot for control flexure specimen at R ₁ =0.01in/min	69
6.3	Experimental and NOVA-3D load-displacement curve for control flexure specimen at R ₂ =1.00in/min	70
6.4	NOVA-3D contour plot for control flexure specimen at R ₁ =1.00in/min	71
6.5	Experimental and NOVA-3D load-displacement curve for (a) HWU1 (b) CWU1 (c) HWS1 (d) CWS1 at displacement rate R ₁ =0.01 in/min for flexure test simulation	74
6.6	Experimental and NOVA-3D load-displacement curve for (a) HDS1 (b) CDS1 (c) HWU2 (d) CWU2 at displacement rate R ₁ =0.01in/min for flexure test simulation.....	75
6.7	Experimental and NOVA-3D load-displacement curve for (a) HDU2 (b) CDU2 (c) HWS2 (d) CWS2 at displacement rate R ₁ =0.01 in/min for flexure test simulation	76
6.8	Experimental and NOVA-3D load-displacement curve for (a) HDS2 (b) CDS2 (c) HWU3 (d) CWU3 at displacement rate R ₁ =0.01in/min for flexure test simulation.....	77
6.9	Experimental and NOVA-3D load-displacement curve for (a) HDU3 (b) CDU3 (c) HWS3 (d) CWS3 at displacement rate R ₁ =0.01 in/min for flexure test simulation	78
6.10	Experimental and NOVA-3D load-displacement curve for (a) HWU1 (b) CWU1 (c) HWS1 (d) CWS1 at displacement rate R ₂ =1.00in/min for flexure test simulation	81

6.11	Experimental and NOVA-3D load-displacement curve for (a) HDS1 (b) CDS1 (c) HWU2 (d) CWU2 at displacement rate $R_2=1.00\text{in/min}$ for flexure test simulation.....	82
6.12	Experimental and NOVA-3D load-displacement curve for (a) HDU2 (b) CDU2 (c) HWS2 (d) CWS2 at displacement rate $R_2=1.00\text{in/min}$ for flexure test simulation	83
6.13	Experimental and NOVA-3D load-displacement curve for (a) HDS2 (b) CDS2 (c) HWU3 (d) CWU3 at displacement rate $R_2=1.00\text{in/min}$ for flexure test simulation.....	84
6.14	Experimental and NOVA-3D load-displacement curve for (a) HDU3 (b) CD3 (c) HDS3 (d) CDS3 at displacement rate $R_2=1.00\text{in/min}$ for flexure test simulation	85
6.15	Cohesive traction separation law	88

CHAPTER 1

INTRODUCTION

Composites provide numerous advantages over other materials in terms of strength, stiffness, low weight and design flexibility. Over the last 20 years, the use of composite materials in civil engineering constructions has shown considerable increase, particularly in the form of wraps for seismic upgrading and repairs. Their use is, however, limited due to the lack of long-term durability data. Several factors affect the durability of composites, viz., materials used, manufacturing process, void content, fiber matrix bonding, environmental conditions, mechanical loading etc. While in-depth study has been performed on the factors affecting durability, long term degradation of materials due to the environmental conditions has yet to be studied in detail. There are heightened concerns regarding the overall durability of these materials, especially related to their capacity for sustained performance under harsh and changing environmental conditions under load. They typically fail in a brittle and catastrophic manner with little forewarning.

Currently, no capability exists for reliably projecting future state and conditions of composites in various environments. The current research was aimed at developing a means of predicting the long-term performance of the composite materials, based on accelerated laboratory testing and degradation models. Loading conditions and mechanical properties of interest included shear, compressive and tensile properties, fatigue, ductility and impact resistance for each type of composite material depending on its application. The research work in this thesis

deals with compressive and tensile properties of carbon fiber/epoxy loaded in three point bend configuration.

The modeling and testing approach is summarized below

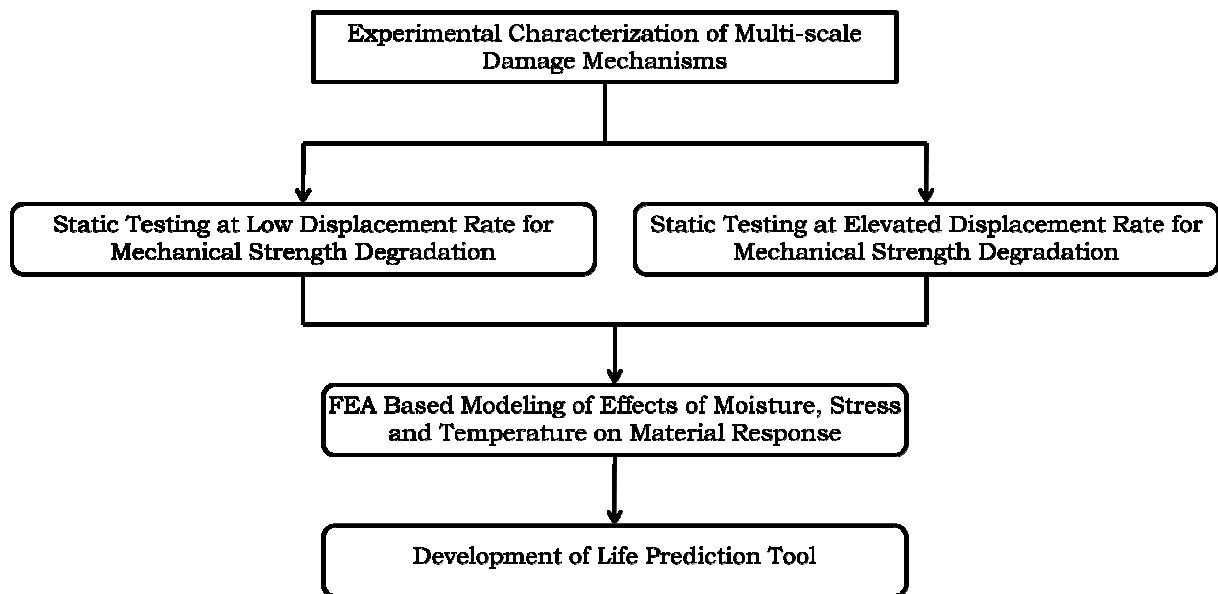


Figure 1.1: Modeling and testing approach

A basic predictive tool using the Arrhenius principles along with environmental exposure and mechanical tests to measure degradation of carbon fiber epoxy composite under hygrothermal and mechanical loading has been developed. The test captured the synergistic effects of field exposure and extreme temperatures, viz., hot/wet/unstressed, cold/wet/unstressed, hot/dry/unstressed, cold/dry/unstressed, hot/wet/stressed, cold/wet/stressed, hot/dry/stressed and cold/dry/stressed. The capacity loss from changes at the molecular level, such as hydrolysis, microcracks, chemical degradation, stress induced crack growth in fibers and fiber/matrix debond and effects of higher strain rates have been incorporated in the model using a unique finite-element (FE) based multi-scale, multi-mechanism degradation model. The failure has been

modeled using cohesive elements in the areas of expected crack growth. The environmental degradation is incorporated by changing the values of maximum stress and strain in the cohesive elements. This model successfully predicts the failure load and deflection for specimens under three point bend configuration and at various environmental conditions.

This research is aimed at developing a PC-based user friendly tool that will enable its users to predict the life of the composite under various environmental conditions and loading without the use of FEA. The input includes hygrothermal ageing conditions and point/uniformly distributed load in addition to structural geometry and other parameters and predicts interlaminar shear and flexural failure.

CHAPTER 2

LITERATURE REVIEW

Numerous mechanisms of composite degradation exist, which lead to matrix cracks, fiber-matrix debonding, erosion of matrix, delamination of different layers, hydrolysis and chemical degradation of the matrix, fiber slippage from matrix and fiber breakage. The various agents of degradation can be categorized into (i) environmental degradation, (ii) chemical degradation and (iii) mechanical degradation. Figure 2.1 shows a graphical representation of the degradation mechanisms.

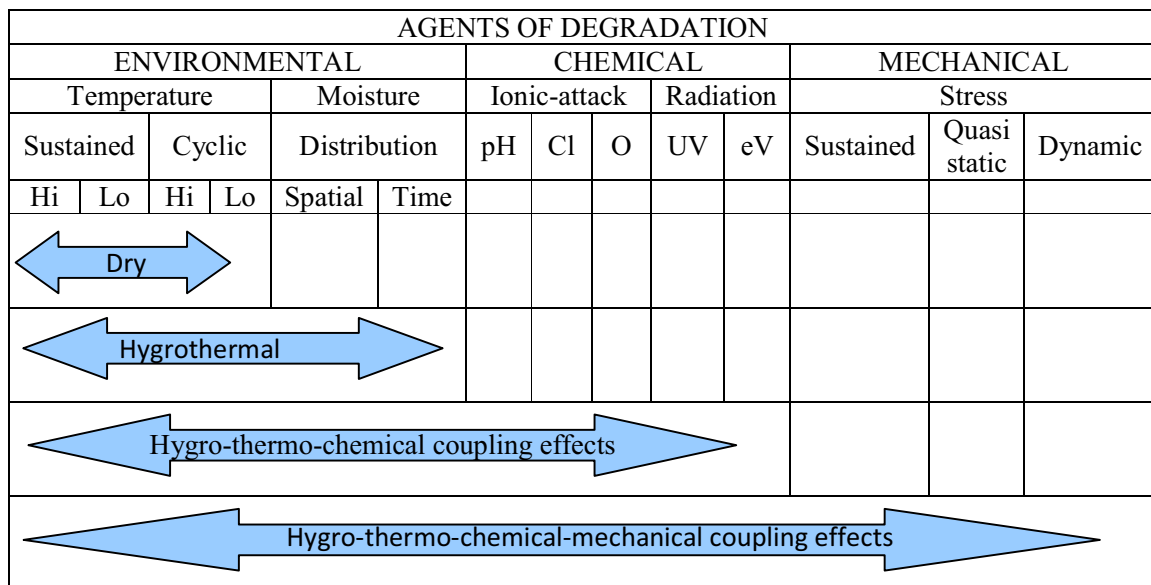


Figure 2.1: Agents of composite degradation

Extensive studies have been carried out on the effect of moisture and temperature on polymer matrix composites. It has been observed that current epoxy resins utilized in high performance structural composites absorb moisture from high humidity environment (McKague,1975; Shen,1976; McKague,1976; Browning,1977). The moisture absorption is mainly due to the moisture affinity of some functional groups in the cured resin. This leads to swelling and reduction in the glass transition temperature (T_g). As a result, moisture absorption affects the temperature range over which the matrix dominated composite properties remain stable. It has been documented that moisture absorption reduces the temperature at which degradation of the composite mechanical properties occur (Fried,1967; Browning,1974a,b). Also, composites are sensitive to temperature variations due to thermal stresses between fiber and resin owing to their different thermal expansion coefficients (Birger,1989; Massiv,1977; Myer,1983). The induced thermal stresses may be relieved by formation of cracks and in extreme cases, by fiber fracture. Unequal swelling stresses due to moisture absorption can also lead to the formation of microcracks (Zhang,1977; Chang,1981; Blikstad,1984; Dewumille,1983).

In order to utilize the full capability of the composite, its behavior under hygrothermal conditions and stress must be studied in detail. Ageing data obtained over many years is time consuming and impractical (Cirisciulli,1987; Demuts,1984). Hence, accelerated ageing tests are employed to simulate long term effects by exposing composites to aggressive environmental conditions.

2.1 Influence of Moisture

Extensive work has been carried out on the effect of moisture on polymer matrix composites. It has been observed that moisture plays a key role in the degradation of polymer

matrix composites. Based on the concept that amount of water absorption affects the mechanical properties of composites, research work has been performed on accelerated ageing of composites by varying length of exposure time, temperature, relative humidity and stress applied in order to achieve the predetermined water content in the composite (Joshi,1983; Allred,1981; Shen,1981).

2.1.1 Moisture Absorption

Moisture absorption data gives an insight into the mechanics of moisture absorption. Some explanation into the influence of moisture on composites can be gained by studying the plots of moisture absorption as a function of time. For example, in Figure 2.2, Curve C is indicative of significant interfacial degradation. Interfacial degradation creates room for water molecules to be absorbed and trapped in the region of degraded interface and hence, shows an increase in the weight. Bond strength between resin particles becomes weak on contact with water molecules and the resin starts to leach. Curve D is indicative of this behavior. Curves A and B represents typical, reversible, moisture absorption behavior, and curve E is classical Fickian moisture absorption (Weitsman,2000). The moisture absorption is dependent on the composite system, fluid, exposure condition and time. Fluid absorption that follows along curve A or curve B is typically thought to occur as a result of the competing rate processes of water diffusion and polymer relaxation (Zhou,1999).

The diffusion of free water is reversible, but the diffusion of bound water is not. As discussed by Xiao and Shanahan (Xiao,1997), in the initial stages of moisture absorption, the water reacts chemically, causing hydrolysis leading to chain scission. This chain scission leads to chemical addition of water and hence this water is unable to leave even upon drying. By assuming that water diffusion is approximately Fickian and that degradation of the resin is mainly caused by hydrolysis reactions, a theoretical model was developed to describe the water

absorption/desorption phenomena. The model developed by Xiao and Shanahan was able to estimate the average molecular weight of the intercrosslink chains after aging.

External factors can also influence composite moisture absorption. For example, applied stress has been shown to increase saturation moisture concentration (Weitsman,2000; Gillat,1976). Damage due to applied stress and/or moisture diffusion and temperature also plays a major role in composite absorption behavior. Some studies have reported increased diffusion but unchanged saturation concentration (Roy,2001; Obst1996) while others report unchanged diffusion but increased saturation concentration (Patel,2002). Roy et al. developed a damage mechanics based model to predict moisture absorption behavior as a function of transverse and longitudinal cracking. Other factors that influence diffusion and/or saturation concentration are temperature, fluid acidity, and exposure duration (Weitman,2000).These factors are all important in considering the composite durability issues in hot and humid environment.

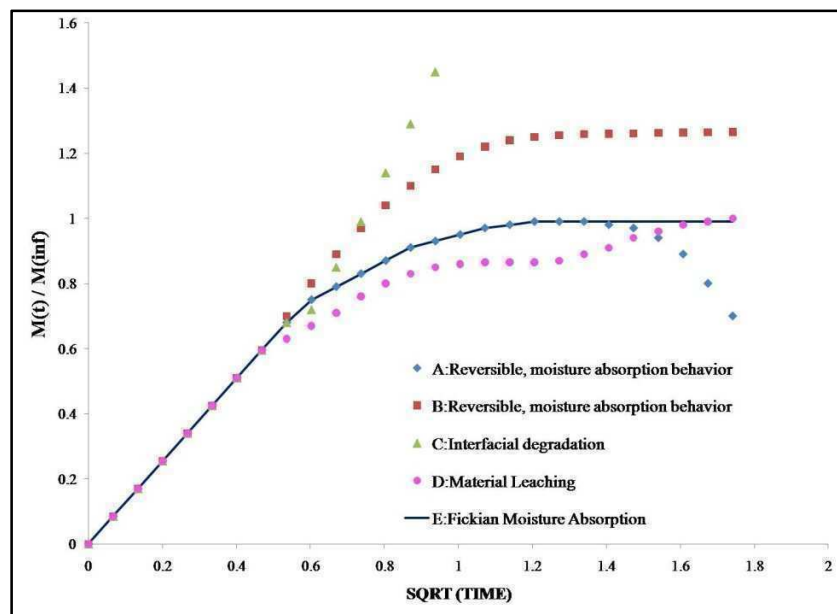


Figure 2.2: Moisture Absorption by polymer composites

2.1.2 Effect on Static Strength and Stiffness

The matrix and interfacial properties largely determine the mechanical response of carbon/polymer laminates since carbon fibers are insensitive to moisture as opposed to glass fibers which are known to degrade in the presence of moisture(Weitman,2000). A few of the possible effects of moisture are the formation of residual hygrothermal stresses, polymer and interfacial degradation, and polymer plasticization (Hahn,1976). Combined, these effects can act to enhance or degrade the fracture toughness of the material. Moreover, the plasticization can result in decreased glass transition temperature(Demonet,1989) which may affect behavior of the composite in elevated temperature environments.

2.1.3 Effect on Tensile Properties

The tensile properties of carbon/polymer composite laminates, particularly those with orientations other than $[90]_n$, are generally considered to be insensitive to moisture. However, at moisture contents above 1%, 0° and 45° degree laminates have shown up to 20% decrease in tensile strength (Shen,1981).

2.2 Influence of Temperature

The effects of temperature on carbon/epoxy composites are similar to the effects of moisture. The changes in the composite in response to temperature are dependent on changes in the matrix and interfacial regions. Carbon fibers tend to be unaffected up to temperatures of 600°C (McLaughlin,1996).

2.2.1 Effect of Elevated Temperature on Strength and Stiffness

Though carbon fiber composite tensile strength and modulus are generally only minimally affected by temperature alone, distinct strength changes may sometimes occur even

below the glass transition temperature. Matrix dominated properties and interfacial properties are mainly affected by temperature, and degradation in these leads to overall change in composite strength and stiffness, especially in fatigue.

Takeda and Ogihara (Takeda,1994) studied the microscopic failure processes of two graphite/epoxy cross-ply composite laminates at room temperature and at 80°C. Experimentally, it was found that tensile strength increased with temperature for the thinnest laminate (6-ply), but decreased slightly for the thicker laminates. They observed that, in the toughened epoxy composite system the crack density decreased with temperature while the first crack strain increased with temperature. SEM images of failure surfaces indicated that little or no additional interfacial debonding took place at elevated temperature than at room temperature.

Detassis et al. (Detassis,1995) used fragmentation testing on single-fiber model composites to study the interfacial shear strength on carbon/epoxy composites as a function of temperature. The study considered both sized and de-sized fibers, and the epoxy was a low T_g variety (T_g=39°C). While interfacial shear strength values were found to decrease with temperature in single fiber composites, sized and de-sized, the values of the sized single-fiber composites were generally much higher than that of the de-sized single fiber. Moreover, the de-sized single fiber composite interfacial shear strength values were very similar to matrix shear strength values.

Data given by Reifsnider and Case (Reifsnider,1995) show that, in some cases, tensile strength may actually increase with temperature. Moreover, it is shown that the increase in strength may come as a result of degradation in interfacial properties. The interfacial properties affect the ineffective length at a fiber break, or the axial distance from the plane of the fiber break it takes for the fiber to regain full load bearing capacity.

Roy and Singh (Roy,2008) presented a simple methodology for transitioning from a micro-mechanics (RVE)-based kinetic model to the macro-scale structural level, through the use of continuum damage mechanics. A model was developed to predict the debond growth in G30-500/PMR-15 unidirectional laminates in different thermo-oxidative environments. Using Darcy's law, oxygen permeation in the porous region at fiber/matrix interface was modeled to develop shrinkage induced permeation-controlled debond growth. A cohesive layer model was used for debond initiation and growth and the damage parameters obtained were used to predict long-term behavior of the laminate in a thermo-oxidative environment.

2.2.2 Effect of Low Temperature

Significant changes are seen in composites when exposed to extreme temperatures. Most materials expand when the temperature rises. In fiber-reinforced polymer matrix composites, the coefficient of thermal expansion of the matrix is usually an order of magnitude greater than that of the fibers. This is especially true for carbon composites, which have a negative coefficient of thermal expansion, meaning that as the matrix contracts due to low temperature, the fibers tend to elongate. A decrease in temperature due to cooling during the fabrication process or low-temperature operating conditions will cause the matrix to shrink. Contraction of the matrix is resisted by relatively stiff fibers through fiber/matrix interface bonding, setting up residual stresses within the material microstructure. The magnitude of the residual stresses is proportional to the difference in curing and operating temperatures of the composite material. Except for extremely cold environments, the induced residual stresses are not of much concern. Where large temperature differentials exist, sufficiently large stresses may induce micro-cracking in the material. These micro-cracks in turn can reduce the stiffness of the composite, increase the

permeability, and increase the water ingress along the fiber/matrix interface, thus contributing to and sometimes accelerating degradation (Dutta,1996;Dutta 1992; Dutta 1994).

Another important effect of low temperatures is the accompanying change in matrix strength and stiffness. Most resin matrix materials become stiffer and stronger as they cool. Glass fiber reinforced polymer composite (GFRP) materials have been used for cryogenic temperature applications with good performance. These matrix changes can influence the modes of failure. At the low temperature the compressive strength of cylindrical specimens increased, but the material failed more violently. The energy absorption before failure at low temperature is higher than at room temperature.

2.3 Influence of Moisture/Temperature Interaction

Various studies examined the effect of the moisture/temperature combination on composite tensile strength and modulus. Almen et al. (Almen,1989; Asp,1990) presented results showing degradation of a variety of carbon fiber reinforced epoxy woven composite properties in hot/wet environments. Shen and Springer (Shen,1981) found moisture related degradations in tensile strength and stiffness of 0° and 45° carbon/epoxy composites to be independent of temperature. On the other hand, tensile properties of 90° laminates were significantly affected by moisture and temperature.

A number of studies have been performed to determine how hygrothermal environments affect the strain energy release rates of carbon/epoxy composites. A review of these is given by Asp (Asp,1998). The combined results of the studies point to an ambiguity as to the effects of moisture and temperature on strain energy release rates, implying that each carbon/epoxy system must be examined individually.

2.4 Influence of Environment on Flexural Strength and Modulus

Shih and Ebert (Shih,1986) evaluated the fiber-matrix interfacial strength of unidirectional composites in bending. Controlled surface treatments of the fibers and hygrothermal ageing caused a reduction in strength and a change in the failure mode from pure tension to a mixed mode tension-compression or shear, and failure with the transition point shifting to higher values of L/H.

The effect of temperature on the flexural strength of graphite epoxy composites aged at 170°C for up to 626h was studied by Birger et.al.(Birger,1974). It was seen that at a constant L/H ratio, both flexural and shear strengths decrease. No degradation in properties was observed at short ageing durations, but degradation was observed at longer exposure times. Prolonged thermal ageing causes a shift in the transition point for failure to higher L/H ratios as well as a reduction in flexure properties. In some cases, transition point disappeared and failure occurred only by delamination. It was also seen that with increase in thermal exposure time, the fracture changed from ductile to more brittle. In addition, a considerable change in glass transition temperature of the graphite epoxy composite was also observed on exposure to hygrothermal conditions.

Singh et.al.(Singh,2008) observed a small increase in flexural modulus of carbon/epoxy composites exposed to UV and condensation and for fatigue at low stress levels. Specimens under compressive load during ageing showed considerable reduction in strength.

CHAPTER 3

ENVIRONMENTAL AGEING AND MECHANICAL TESTING

Long term environmental ageing and testing of carbon/epoxy specimens was conducted and the data was used for model calibration and verification. The work involved performing an extensive array of accelerated ageing tests. The accelerated ageing test matrix is shown in Table 3.1. Ageing temperatures of 50°C (cold) and 70°C (hot) were selected based on the specific extreme application profile, with 10 to 20 degrees added to accelerate the ageing process based on the Arrhenius 10-degree rule. Four specimens were tested at each condition. The aged specimens were tested at regular time intervals for flexure strength in three point bend configuration at two crosshead speeds $R_1=0.01$ in/min and $R_2=1.00$ in/min. Elevated strain rate experiments were performed to simulate impact and seismic loads. The failed specimens were observed under optical microscope for accurate determination of failure modes and failure mechanisms, viz, fiber fracture, matrix cracking, fiber-matrix interfacial debond, chemical degradation etc. The test data are used as input for a finite element based computational model. Results from the FE model will be implemented into the Field Usable Design Tool to predict composite durability of carbon/epoxy specimens when exposed to different ageing conditions.

Table 3.1: Test matrix for accelerated ageing of cross ply flexure specimens

Test Type	Temperature	Relative Humidity	Stress Level	Material property Characterized	No. of replicate specimens	
					R ₁	R ₂
Flexure test	T ₁ (Cold-50°C)	Dry (0% RH)	Unstressed	Bending stiffness, Compressive and Tensile strength	4	4
			Stressed (5% UTS)			
		Wet (100% RH)	Unstressed			
			Stressed (5% UTS)			
	T ₂ (Hot-70°C)	Dry (0% RH)	Unstressed		4	4
			Stressed (5% UTS)			
		Wet (100% RH)	Unstressed			
			Stressed (5% UTS)			

3.1 Fabrication of specimens

Vacuum Assisted Resin Transfer Molding (VARTM) was used to manufacture cross-ply carbon/epoxy panels. VARTM provides significant advantages over other manufacturing methods, including, high fiber to resin ratio, low void content and relatively low vacuum and tooling requirements.

3.1.1 Materials

The fabric used was HMF Cu 160, obtained from SciArt, Canada. This is UNI WEB carbon fiber which consists of non woven sheets of unidirectional carbon fibers, held in position

by a fine spider web of polymer fibrils on one or both surfaces. The special polymer used is compatible with epoxy and polyester resins. The fibril or web system that bonds the reinforcement together allows the fabric to be easily trimmed or slit, giving clean edges with no fraying. The fibers lay flat and cannot shift or bunch up as is often seen in unstitched fabrics. Dry carbon fiber uniweb weighs 3.5 oz. / sq. yd and is 0.25mm thick. The resin system used is SC-780, a low viscosity, two-phase toughened epoxy supplied by Applied Poleramic Inc. The viscosity of the resin is 300cps at 160°F and its cured density is around 1.09gm/cc. Chemically, SC-780 consists of 60-70% diglycidylether of bisphenol A, 10-20% aliphatic diglycidylether and 10-20 % epoxy toughener. The hardener consists of 70-90% aliphatic amine and 10-20% triethylenetetramine. The mixing ratio of resin to hardener is 100 to 22 by weight or 4 to 1 by volume. The glass transition temperature (Tg) of the cured resin is 200°F. The resin is specifically designed for Vacuum Assisted Resin Transfer Molding (VARTM) process. The pot life and viscosity have been tailored to allow infusion at 77°F. SC-780 can be cured at room temperature or at elevated temperature to achieve maximum properties. This resin works well in structural and ballistic applications that require damage resistance. Figure 3.1 shows the materials used for manufacturing the composite panels.

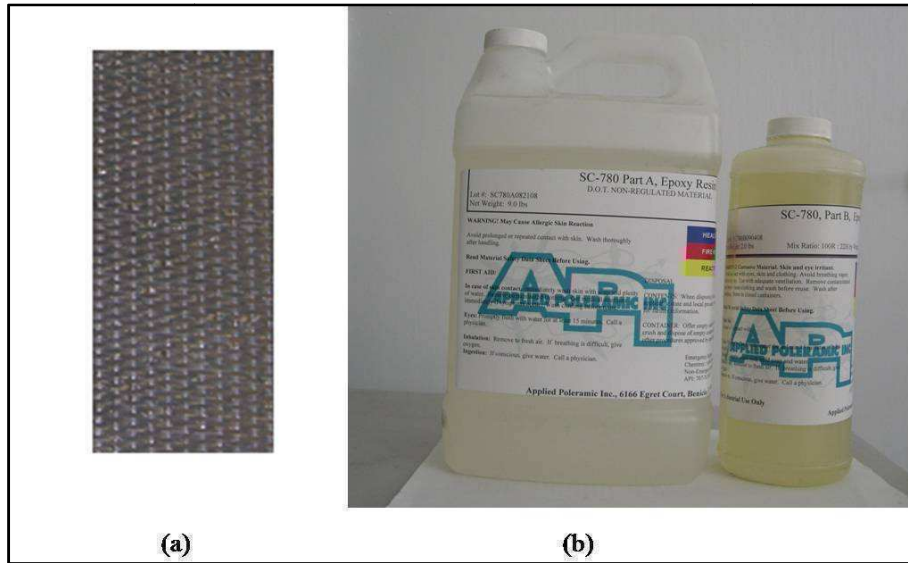


Figure 3.1: (a) Carbon fiber (b) Resin and hardener

3.1.2 VARTM Process

An Aluminum flat plate was used as the mold to prepare the composite laminates using VARTM. Figure 3.2 shows a schematic of the VARTM setup and Figure 3.3 shows the actual setup.

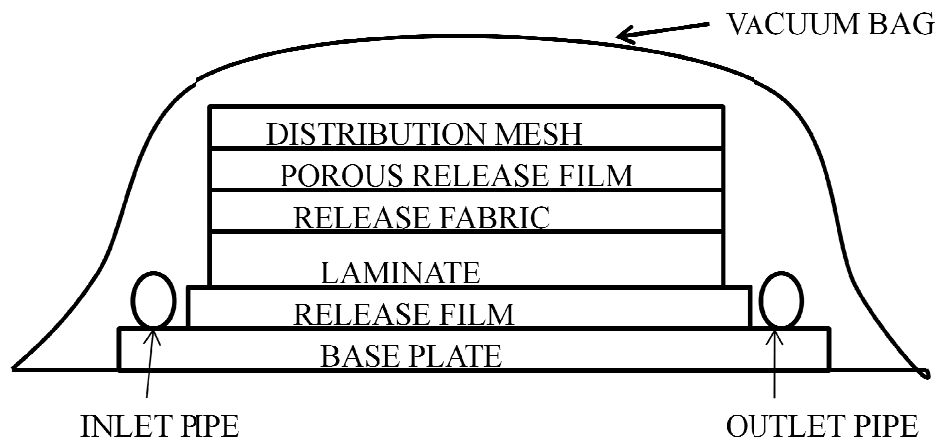


Figure 3.2: Schematic of VARTM setup



Figure 3.3: Actual VARTM setup

The mold was thoroughly cleaned with acetone and Freekote liberally applied on the surface and allowed to dry. A release film was placed on the mold and the dry carbon fiber was carefully placed on it in the $[0_2/90_2]_{2S}$ configuration as desired. A porous release film was placed on the fiber followed by a distribution mesh. The porous release film permits easy removal of the laminate on curing. The distribution mesh was used to channel the resin flow through the length of the fiber. The distribution mesh should be placed approximately 25.4mm from the end of the fabric. This allows the resin to flow to the bottom layer of the laminate. It was observed that when the distribution mesh extended to the end of the laminate length, the resin flow on the mesh was fast and it started to flow out through the outlet pipe. This led to wetting of only the top layers of the fabric, while the lower layers remained dry (Song, 2003). A spiral tube attached to a clear vinyl tube was placed on the inlet and outlet sides of the setup. The spiral tube was of 12.7mm inner diameter and the vinyl tube was of 6.35mm inner diameter. The outlet pipe was connected to a vacuum pump and the inlet pipe was held in a resin beaker. The entire setup was

vacuum-bagged and debulked for 1 hour before resin infusion to release air pockets in the fabric and minimize void content. The resin flow through the laminate is purely under vacuum pressure. During resin infusion, the temperature was maintained at approximately 80°F to 85°F to optimize the resin flow and to ensure proper wetting of the laminate. Care must be taken to ensure no air bubbles enter the setup through the inlet pipe. Once the desired quantity of resin has been infused, the inlet pipe was clamped. The resin continued to flow through the laminate under vacuum pressure for approximately 90 minutes at 85°F. Thereafter, the outlet pipe was closed with a crocodile clamp and a rectangular plate of approximately 10kg was placed on the laminate. The weight was used to enhance the consolidation of the laminate. The entire setup was left for overnight cure in an oven at 85°F. Throughout the process, care must be taken so that no air enters the setup as this may slow down or even stop the resin flow through the laminate. After curing, the laminate was removed from the mold and kept on a flat plate to post-cure at 160°F for 6 hours. Post cure at this temperature results in approximately 95%-97% of cross-linking. In order to study the effect of temperature on strength of the material, the laminate was required to be post-cured for an additional 2 hours at 220°F to ensure complete cross-linking. An acid digestion test and C-scan were performed on the laminates to ensure quality. The laminates comprised approximately 53% fiber, 45% resin and 1.73% voids.

3.2 Accelerated Environmental Ageing

3.2.1 Panel description

All panels were of $[0_2/90_2]_{2s}$ configuration. Each panel subjected to ageing was 127mm × 127mm × 3mm in dimension. Holes were drilled in the two sides of the stressed panels in order

to fix them in the specially designed stress fixture (see next section for details). The holes were drilled such that the panel was stressed transverse to the center 90 layers.

3.2.2 Environmental conditions

Two temperature conditions, termed ‘hot’ (H:70°C) and ‘cold’ (C: 50°C), were selected for accelerated ageing. Accelerated moisture ageing of the specimens was carried out in environmental chambers at the two temperature conditions. In order to maintain 100% relative humidity (RH), the ‘hot wet’ and ‘cold wet’ specimens were immersed in a bath containing de-ionized water. Similarly, dry specimens were aged in an oven at 70°C for hot conditions and 50°C for cold conditions. An applied load equivalent to 5% of the ultimate tensile strength (UTS) of the material was applied to the ‘stressed’ specimens during environmental ageing using a unique constant strain fixture developed to avoid creep rupture of the specimens (Figure 3.4).

Depending on the ageing conditions, the specimens were designated as shown in Table 3.2, in which:

H represents ‘hot’ (70 °C)

C represents ‘cold’ (50 °C)

W represents ‘wet’ (100% RH)

D represents ‘dry’ (0% RH)

S represents ‘stressed’ (5% UTS)

U represents ‘unstressed’

1, 2, 3 represent the ageing time interval t_1 , t_2 and t_3

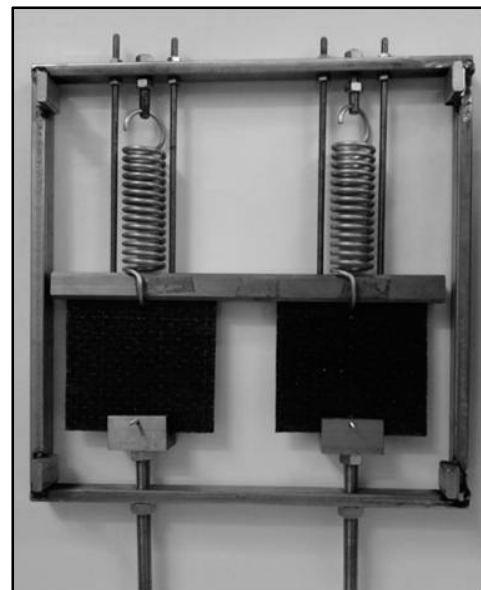


Figure 3.4: Unique constant strain fixture

Table 3.2: Test specimen nomenclature and number of panels required

Environmental Exposure condition	Nomenclature (Number of panels aged)			
	t₀	t₁	t₂	t₃
Unaged (Control)	CF00 (1)	CF01 (1)	CF02 (1)	CF03 (1)
HWU	-	HWU1 (1)	HWU2 (1)	HWU3 (1)
HDU	-	HDU1 (1)	HDU2 (1)	HDU3 (1)
CWU	-	CWU1 (1)	CWU2 (1)	CWU3 (1)
CDU	-	CDU1 (1)	CDU2 (1)	CDU3 (1)
HWS	-	HWS1 (2)	HWS2 (2)	HWS3 (2)
HDS	-	HDS1 (2)	HDS2 (2)	HDS3 (2)
CWS	-	CWS1 (2)	CWS2 (2)	CWS3 (2)
CDS	-	CDS1 (2)	CDS2 (2)	CDS3 (2)

Dimensions of all aged panels were 127mm × 127mm × 3mm. As Shown in Figure 3.6, eight flexure test specimens of 127mm length and 12.7mm width were cut from unstressed panel and four test specimens of 127mm length and 12.7mm width were cut from each stressed panels. Hence, only one panel was required to be aged for unstressed condition for each time interval while the stressed conditions required two. It was ensured that after machining, top and bottom 0° layers were along the span of the flexure test specimen. Table 3.3 shows the ageing times t₁, t₂ and t₃ for the flexure panels. The specimens immersed in water were weighed daily and were saturated once the moisture gain in them was negligible, i.e. the weight remained constant. The ageing times ‘t₁’ were decided based on complete saturation of the wet panels. The HWU1 specimen saturated at about 2544 hours. This aged specimen was then removed from the water bath and cut into test specimens. At approximately the same time, 2592 hours, the corresponding

dry specimen, i.e. HDU1, was removed from the oven and prepared for testing. 't₂' specimens were tested 750 hours after 't₁' and 't₃' were tested at 750 hours after 't₂'. Hence, HWU2 was tested at 3250 hours and HWU3 was tested at 4000 hours while HDU2 was tested at 3294 hours and HDU3 at 4044 hours. Similarly, the ageing times for other specimens was decided.

Table 3.3: Ageing time for flexure specimens

Environmental Exposure condition	Number of specimens (ageing time in hours)				
	t₀	t₁	t₂	t₃	Total
Unaged (Control)	0	2500	3250	4000	32
HWU	-	2544	3294	4044	24
HDU	-	2592	3342	4092	24
CWU	-	2688	3438	4188	24
CDU	-	2712	3462	4212	24
HWS	-	2304	3054	3804	24
HDS	-	2328	3078	3828	24
CWS	-	2376	3126	3876	24
CDS	-	2400	3150	3900	24

3.2.3 Constant Strain Aging Test Fixture

This section describes to a constant strain aging test fixture which can be used in a confined space, such as, an environmental chamber. The objective of the device is to apply a constant strain on a test specimen while it is undergoing exposure to aggressive environment, such as, high temperature and/or humidity, in order to evaluate the synergistic effects of applied strain, temperature and humidity on material durability. The fixture particularly applies to the long-term durability testing of polymers and polymer matrix composites, where the application of sustained load on a test specimen via stretched springs frequently result in premature failure of

the test specimen due to creep rupture. This fixture mitigates this problem by providing a simple methodology to eliminate creep during environmental aging, while enabling the application of a user-specified constant applied strain on the specimen. A specialized fixture is developed to apply loading on samples with the help of a spring on one end of the specimen and a U shaped specimen holder at the other end. In order to maintain constant applied strain, a beam of rectangular cross-section is placed on the top surface of the specimens and held to the frame with threaded rods. The beam width and thickness are calculated by approximating it to be in three-point bend configuration with the specimen at the bottom surface of the beam and threaded rods at the top. The AutoCAD drawing of the constant strain fixture developed for cross-ply flexure specimens is shown in Figure 3.5.

The test fixture comprises of a frame made of stainless steel bars welded together at the corners. Two springs are used to apply a constant continuous load/strain. Selection of the springs depends on the amount of strain to be applied on the specimens and the deflection of the spring required from load measurement perspective. The deflection of the spring plays an important role in the design due to

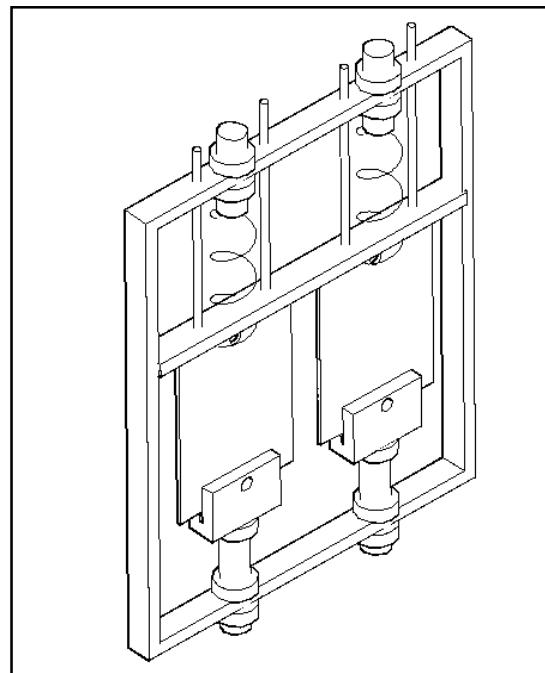


Figure 3.5: Flexural Stress-coupled test fixture

constraints on frame size. One end of the spring is fixed using a threaded rod and the other end of the spring is passed through a hole in the test specimen. The specimens have a hole drilled at the other end and are fixed to the frame with a U-shaped specimen holder as shown in the Figure 3.5. The holder is fixed to the frame with a

threaded rod and nut. As the nut is turned clockwise the rod travels downwards, thus elongating the specimen and extending the spring. The nut is turned continuously until the required spring deflection is achieved. The spring deflection is measured using a Vernier caliper. Once the frame is constructed, a steel beam is placed in the gap between the composite sample and the spring hook which passes through the specimen. The function of the beam is to restrain the specimen from further extending due to creep, thereby maintaining constant strain in the specimens thus preventing pre-mature specimen failure. The beam is held in place using threaded rods which are passed through the top frame and locked in place using nuts. The exact beam dimensions are calculated by assuming the beam to be in three-point bend loading with the loading provided by the spring-loaded specimen at the center of the beam and the supports provided by the threaded rods which hold the beam in place. The criterion for selection of the restraining beam dimensions is as follows: the dimensions of the beam must ensure that the deflection of the beam is less than 1% of specimen elongation under maximum spring load.

The specimens were stressed at approximately 5% UTS in the direction transverse to the center 90° layers. A total of 24 cross ply flexure specimens and 2 unidirectional specimens were aged using this fixture. No premature failure was observed in any of them during ageing, which proves the effectiveness of the fixture design. Details of the various specimens aged using the fixtures are shown in Table 3.4. The thickness 't' of the specimens varied between 2.5mm and 3.3mm.

Table 3.4: Number of specimens aged using the Constant Strain Fixture

Specimen Type	Layup	Dimensions (mm x mm x mm)	Number of Specimens				Approx. Ageing Time (hours)
			Ageing Condition				
			HWS	CWS	HDS	CDS	
Unidirectional	[0] ₁₅	127 × 127 × t	2	-	-	-	3000
Cross-ply	[0 ₂ /90 ₂] _{2s}	127 × 127 × t	6	6	6	6	2000

3.3 Test Method

3.3.1. Test Specimen Description

Four specimens were tested at each ageing condition at displacement rates $R_1 = 0.01$ in/min and $R_2 = 1.00$ in/min. The number of test specimens for each condition at t_1 , t_2 and t_3 and respective ageing time are tabulated below. As seen in Figure 3.6, four test specimens for R_1 and four for R_2 were obtained from each unstressed aged specimen. The stressed panel gives only four test specimens per panel. Hence, two stressed panels are required for each ageing condition. The test specimens from stressed panels are cut away from the drilled holes to avoid any effect of stress concentrations. The test specimens have dimensions 127mm × 12.7mm × 3mm. Tests were performed on both aged and un-aged specimens at two displacement rates in order to study the effect of various ageing conditions and strain rate on flexural strength. The number of test specimens required for each condition is shown in Table 3.5

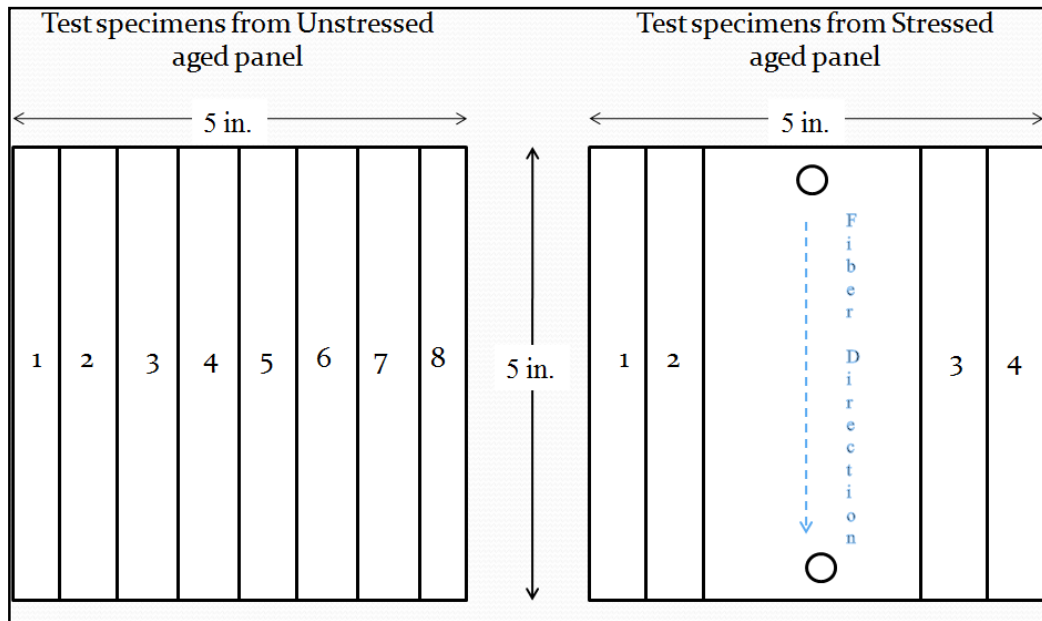


Figure 3.6: Test specimens obtained from aged panel

Table 3.5: Number of test specimens for each condition

Environmental Exposure condition	Number of test specimens				
	t_0	t_1	t_2	t_3	Total
Unaged (Control)	8	8	8	8	32
HWU	-	8	8	8	24
HDU	-	8	8	8	24
CWU	-	8	8	8	24
CDU	-	8	8	8	24
HWS	-	8	8	8	24
HDS	-	8	8	8	24
CWS	-	8	8	8	24
CDS	-	8	8	8	24
TOTAL					224

3.3.2 Test Description

Flexure test was performed according to ASTM D7264 in order to determine the flexural strength of composite specimens. Specimens of large span-to-depth ratio ($L/h > 32$) were considered in three-point bend loading to ensure flexural failure of the specimens. For flexural strength, the standard support span-to-thickness ratio is chosen such that failure occurs at the outer surface of the specimens, due to only the bending moment and is kept constant to avoid any shift in failure modes due to change in span length.

The flexure tests were performed in a 22kips servo-hydraulic testing machine at room temperature under ambient humidity. The rate of crosshead motion was maintained at 0.01 in/min for R_1 and elevated displacement rate at 1.00 in/min for R_2 . Figure 3.7 shows the schematic for the three-point bend test while Figure 3.8 shows the actual experimental setup.

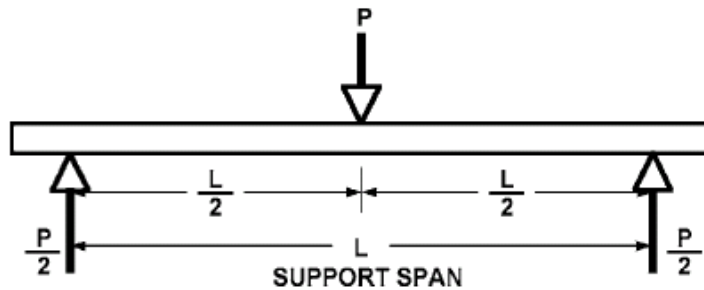


Figure 3.7: Loading diagram for three-point bend test

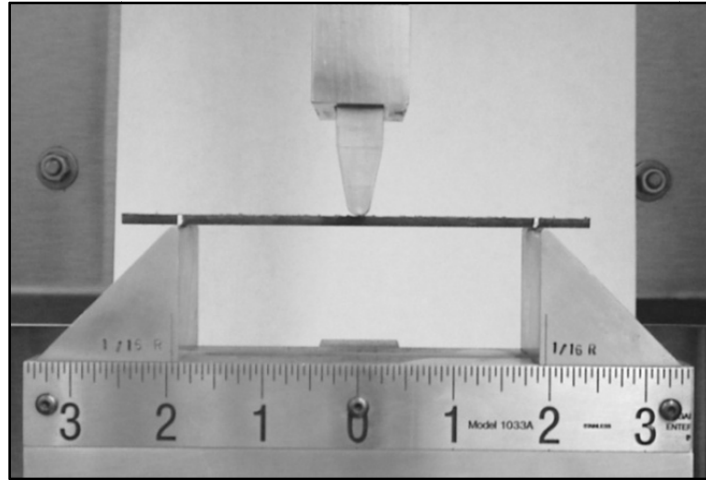


Figure 3.8: Experimental setup for three-point bend test

3.3.3 Flexural Strength Determination

To obtain valid flexural strength, it is necessary that the specimen failure occurs on either one of its outer surfaces, without a preceding interlaminar shear failure or a crushing failure under a support or loading nose. Failure on the tension surface may be a crack while that on the compression surface may be local buckling. Buckling may be manifested as fiber micro-buckling or ply-level buckling. Ply-level buckling may result in, or be preceded by delamination of the outer ply. The formulae used to calculate the maximum stress and strain of the beam are,

$$\sigma_x^{(k)} = -\frac{PLh\bar{Q}_{11}^{(k)}}{8bD_{11}} \quad (1)$$

where,

$\sigma_x^{(k)}$ = stress in the k^{th} layer, Mpa

P = applied force, N

L = support span of the beam, mm

b = width of the beam, mm

h =thickness of the beam, mm

D_{11} = bending stiffness of the beam, MPa

$\bar{Q}_{11}^{(k)}$ = reduced stiffness of the kth lamina in the 1-1 direction, MPa

$$\varepsilon_{xC}^{(k)} = -\frac{PLh}{8bD_{11}} \quad (2)$$

where,

ϵ = maximum strain at the outer surface, mm/mm

δ = mid-span deflection, mm

L =support span, mm

h =thickness of beam, mm

D_{11} = bending stiffness of the beam, MPa

The application of these formulae for flexural strength evaluation is discussed in the next chapter.

CHAPTER 4

MODELING

Arrhenius principle has been used in past work to predict life using accelerated ageing. However, it can only be used for a single mechanism and is unlikely to remain accurate when multiple mechanisms are present, viz. temperature, humidity and stress. A theoretical approach is needed to understand how multiple mechanisms of degradation can be incorporated in a single degradation model. Such multiple mechanisms involve moisture diffusion influenced by temperature, effects of stress, strain and also effects of wet and dry environments.

A theoretical development for life prediction based on irreversible thermodynamics and fundamental principles of continuum mechanics has been developed in the form of a finite element computer based model (NOVA-3D) by Roy et. al. A cohesive layer modeling approach has been used to model the tensile, shear delamination and compressive failure of flexure specimens.

4.1 Cohesive Layer Modeling

A two-dimensional cohesive layer constitutive model with a prescribed cubic traction separation law, constructed from basic principles of continuum mechanics and thermodynamics has been implemented in NOVA-3D. Figure 4.1 depicts the shape of the normalized cubic stress-strain law in the cohesive layer for the case of flexural loading under three point bend configuration. The cohesive law has been modified to include both compressive and tensile

failure of the flexure specimens. Hence, the difference in normalized peak stress in tension and compression.

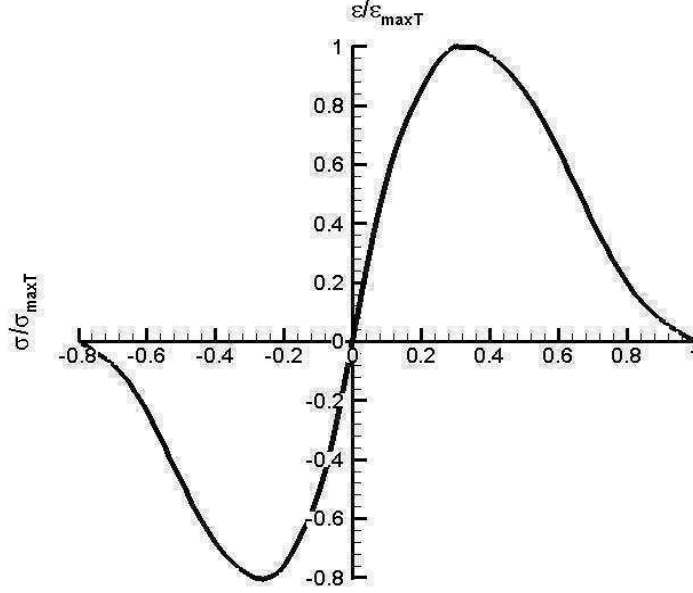


Figure 4.1: Cubic cohesive traction-separation law

For a two-dimensional cohesive layer of finite thickness, h , under quasi static plane-strain conditions, the Helmholtz energy per unit volume derived from irreducible integrity basis is given by equation 3 below,

$$\begin{aligned} \rho\varphi = & C_0(m, T, \sigma_a, \dot{\varepsilon}) + C_1(m, T, \sigma_a, \dot{\varepsilon})\varepsilon_{11} + C_2(m, T, \sigma_a, \dot{\varepsilon})\varepsilon_{22} + C_3(m, T, \sigma_a, \dot{\varepsilon})\varepsilon_{12} + C_4(m, T, \sigma_a, \dot{\varepsilon})\varepsilon_{11}^2 \\ & + C_5(m, T, \sigma_a, \dot{\varepsilon})\varepsilon_{22}^2 + C_6(m, T, \sigma_a, \dot{\varepsilon})\varepsilon_{12}^2 + C_7(m, T, \sigma_a, \dot{\varepsilon})\varepsilon_{11}\varepsilon_{12} \\ & + C_8(m, T, \sigma_a, \dot{\varepsilon})\varepsilon_{11}\varepsilon_{22} + C_9(m, T, \sigma_a, \dot{\varepsilon})\varepsilon_{12}\varepsilon_{22} + C_{10}(m, T, \sigma_a, \dot{\varepsilon})\varepsilon_{22}^3 \\ & + C_{11}(m, T, \sigma_a, \dot{\varepsilon})\varepsilon_{22}^2\varepsilon_{12} + C_{12}(m, T, \sigma_a, \dot{\varepsilon})\varepsilon_{12}^2\varepsilon_{22} + C_{13}(m, T, \sigma_a, \dot{\varepsilon})\varepsilon_{12}^3 \\ & + C_{14}(m, T, \sigma_a, \dot{\varepsilon})\varepsilon_{22}^4 + C_{15}(m, T, \sigma_a, \dot{\varepsilon})\varepsilon_{22}^3\varepsilon_{12} + C_{16}(m, T, \sigma_a, \dot{\varepsilon})\varepsilon_{22}^2\varepsilon_{12}^2 \\ & + C_{17}(m, T, \sigma_a, \dot{\varepsilon})\varepsilon_{22}\varepsilon_{12}^3 + C_{18}(m, T, \sigma_a, \dot{\varepsilon})\varepsilon_{12}^4 \end{aligned}$$

where C_i are material constants, that are, for quasi-static analysis, dependent on temperature (T), moisture concentration (m), applied stress (σ_a) and strain rate ($\dot{\varepsilon}$), ε_{ij} are components of mechanical strain tensor in the representative volume element(RVE). From the reduced entropy

inequality, the corresponding longitudinal stress is obtained by taking the derivative of the Helmholtz energy with respect to the longitudinal strain, yielding,

$$\begin{aligned}\sigma_{11(T)} = & \frac{27}{4} \bar{\sigma}_{MAX(T)} \left\{ \left[1 + \bar{C}(m, T, \sigma_a, \dot{\epsilon}) \Delta m + \tilde{C}_5(m, T, \sigma_a, \dot{\epsilon}) \Delta m^2 \right] \bar{\epsilon}_{11(T)} \right. \\ & - 2 \left[1 + \bar{C}_{10}(m, T, \sigma_a, \dot{\epsilon}) \Delta m + \tilde{C}_{10}(m, T, \sigma_a, \dot{\epsilon}) \Delta m^2 \right] \bar{\epsilon}_{11(T)}^2 \\ & \left. + \left[1 + \bar{C}_{14}(m, T, \sigma_a, \dot{\epsilon}) \Delta m + \tilde{C}_{14}(m, T, \sigma_a, \dot{\epsilon}) \Delta m^2 \right] \bar{\epsilon}_{11(T)}^3 \right\}\end{aligned}\quad (4)$$

$$\begin{aligned}\sigma_{11(C)} = & \frac{27}{4} \bar{\sigma}_{MAX(C)} \left\{ \left[1 + \bar{C}(m, T, \sigma_a, \dot{\epsilon}) \Delta m + \tilde{C}_5(m, T, \sigma_a, \dot{\epsilon}) \Delta m^2 \right] \bar{\epsilon}_{11(C)} \right. \\ & - 2 \left[1 + \bar{C}_{10}(m, T, \sigma_a, \dot{\epsilon}) \Delta m + \tilde{C}_{10}(m, T, \sigma_a, \dot{\epsilon}) \Delta m^2 \right] \bar{\epsilon}_{11(C)}^2 \\ & \left. + \left[1 + \bar{C}_{14}(m, T, \sigma_a, \dot{\epsilon}) \Delta m + \tilde{C}_{14}(m, T, \sigma_a, \dot{\epsilon}) \Delta m^2 \right] \bar{\epsilon}_{11(C)}^3 \right\}\end{aligned}\quad (5)$$

where, the maximum longitudinal tensile stress in the cohesive layer is $\bar{\sigma}_{\max(T)}$ and the maximum longitudinal compressive stress is $\bar{\sigma}_{\max(C)}$. $\bar{\epsilon}_{11(T)}$ and $\bar{\epsilon}_{11(C)}$ are the normalized strains in the tensile and compressive cohesive layers respectively. The material constants C_i can be evaluated through comparison of the area under the traction-separation curve.

Combining the mechanism-based stress prediction capabilities of NOVA-3D with the micromechanics based environmental degradation model enables us to predict the long term durability of composite structures with far greater accuracy than an empirically determined Arrhenius approach. The model has been benchmarked and validated using the experimental data.

4.2 Mechanism-Based Micromechanics Model

A finite element based micromechanics model of a fiber, matrix and fiber-matrix interface within a RVE is conceptually depicted in Figure 4.2

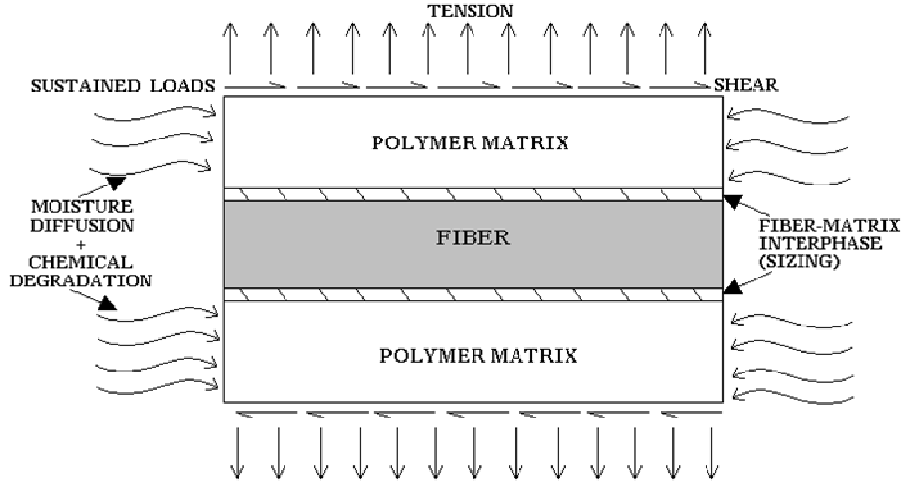


Figure 4.2: RVE of Micromechanics Model for Fiber-Matrix Degradation Simulation

As shown in the figure, the model incorporates synergistic interactions between temperature, moisture diffusion, chemical reaction and applied and residual stresses that arise due to matrix swelling and shrinkage. Environment assisted degradation is simulated using a unique cohesive layer debond model developed by Roy et. al. (Roy,2006) including environmental effects. Failure in the bulk matrix and/or fiber is predicted using an approach similar to the Strain Invariant Failure Theory by Tsai et. al. (Sihna,2005). Time dependent degradation effects in fiber and matrix due to accelerated diffusion and chemical reactions is simulated through the use of a modified diffusion-reaction equation of the form (Xiao, 1997)

$$\frac{\partial m_2}{\partial t} + \frac{\partial m_1}{\partial t} = \frac{\partial}{\partial X} \left(D_{11} \frac{\partial m}{\partial X} \right) + \frac{\partial}{\partial Y} \left(D_{22} \frac{\partial m}{\partial Y} \right) + \frac{\partial}{\partial Z} \left(D_{33} \frac{\partial m}{\partial Z} \right) \quad (6)$$

$$m_2 = r m_1 \quad (7)$$

where m_1 is the mobile phase concentration, m_2 is the bound phase concentration, D_{ij} are the orthotropic diffusivities that could depend on temperature, stress and moisture concentration and t is times. The diffusivities are characterized using weight-gain/loss data under different relative humidity conditions.

$$N(t) = N_0[Z * \exp(-m_2(t)/N_0) - (Z - 1)] \quad (8)$$

$$S_H(t) = N(t)/N_0 \quad (9)$$

where, N_0 = Number of network crosslinks per mole at time, $t=0$

N_t = Number of remaining network crosslinks per mole at any time, t

Z = Parameter determining the type of crosslink ($Z=3$)

$S_H(t)$ = internal state variable quantifying damage

Initially, at time $t=0$, there are N_0 number of crosslinks per mole in the resin. But as the specimens are aged in moisture, the bound moisture reacts with the crosslinks and breaks the molecular chains. Hence, the number of crosslinks in the polymer decrease as time progresses. $N(t)$ gives the number of crosslinks per mole of resin at any time t . $S_H(t)$ gives the ratio of $N(t)/N_0$ at any time t . $S_H(t)$ is the internal state variable that quantifies damage and it is used as a factor by which the resin properties are degraded due to moisture with time.

Although the RVE in Figure 4.2 depicts the special case of fiber-matrix debond failure, the cohesive layer approach has been adapted to predict compressive wrinkling, delamination and fiber fracture. The ultimate objective of the micromechanics based simulations is predicting the composite stiffness and strength degradation as a function of aging time, as schematically depicted in Figure 4.3. The exact shape of simulated curves is controlled by the environmental factors as well as specific failure modes. Results from the micro-scale model are used as input to a macro-scale model.

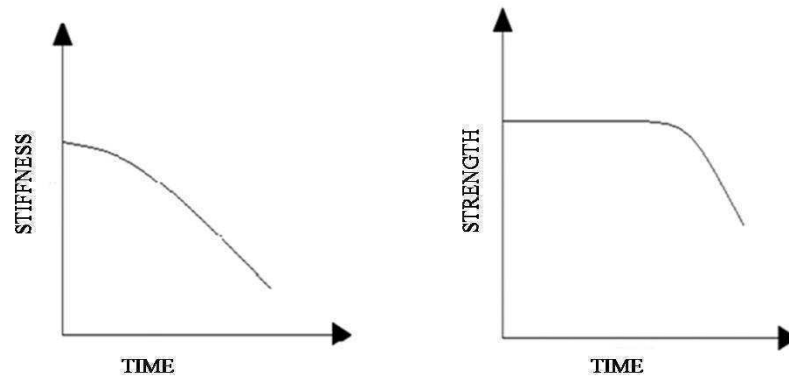


Figure 4.3: Simulated stiffness and strength degradation with ageing time

4.3 Multi-Scale Mechanism Based Model Development

A novel multi-scale model is developed for the life prediction of structures under hygrothermal and mechanical loading. The model is capable of assessing damage in the structure and predicting the ultimate strength under constant hygro-thermal and mechanical load P as shown in Figure 4.4.

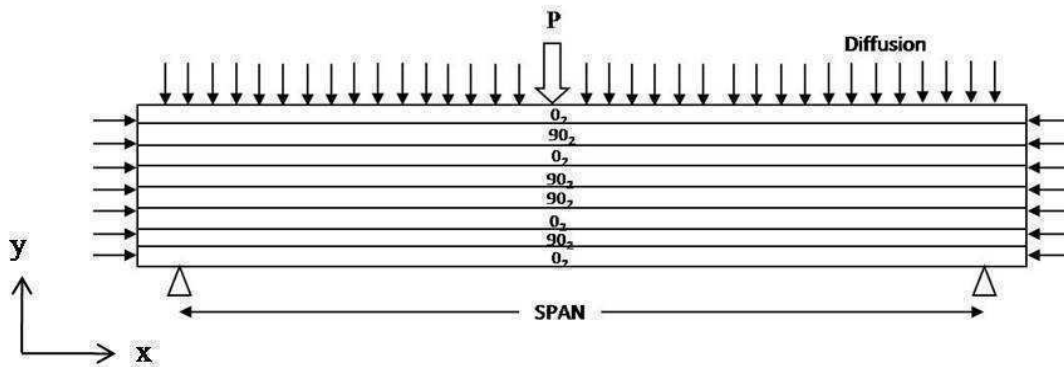


Figure 4.4: Diffusion on flexure model for $[0_2/90_2]_{2s}$ laminated composite

4.3.1 Cohesive Layer Approach

Ductile polymeric adhesive materials usually have a nonlinear normal and shear stress-strain response. On crack initiation and propagation, there exists a damage zone ahead of the

crack tip. Cohesive forces must be taken into account in order to capture the behavior of failing material in this zone. In order to model this non-linear behavior near the crack tip, cohesive elements are placed along the probable failure path in the material. The flexural specimen has cohesive elements placed in the region below the loading pin for compressive and tensile failures and in between adjacent layers for debonding and delaminations. Environmental degradation in the cohesive material is incorporated through the change in the cohesive layer material properties σ_{maxT} , σ_{maxC} , ε_{maxT} , ε_{maxC} , τ_{max} , γ_{max} where σ_{maxT} is the maximum tensile stress in the cohesive layer, σ_{maxC} is the maximum compressive stress, ε_{maxT} is the maximum tensile strain, ε_{maxC} is the maximum compressive strain, τ_{max} is the maximum shear stress and γ_{max} is the maximum shear strain in the cohesive layer.

4.3.2 General Framework for Modeling Damage and Failure

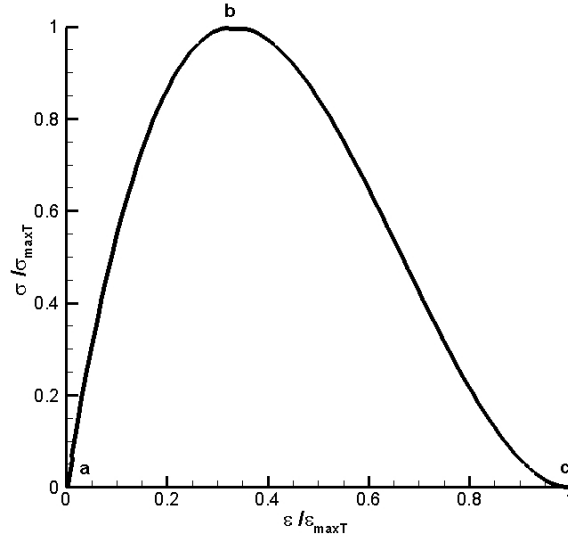


Figure 4.5: Cubic traction-separation law

Material failure refers to the complete loss of load-carrying capacity which results from progressive degradation of the material stiffness. The stiffness degradation process is modeled using damage mechanics. Figure 4.5 shows a typical cubic traction-separation law. The failure mechanism employed consists of four distinct parts:

- (i) Undamaged material response (a-b)
- (ii) Damage initiation criterion (point b)
- (iii) Damage progression law (b-c)
- (iv) Complete separation, element stiffness ≈ 0 upon failure (beyond point c)

4.4 Modeling Procedure

The procedure to model cross-ply flexure test in NOVA-3D code is as follows

4.4.1 Specimen geometry and mesh generation

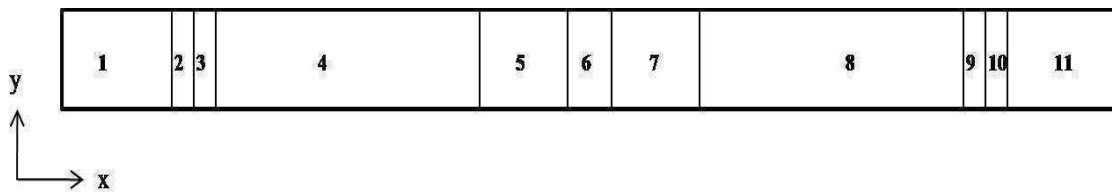


Figure 4.6: Partitioning of flexure specimen along length

Details of the mesh used in this study are outlined below. The beam is divided into 11 parts along the length of the specimen (Figure 4.6). Each part is meshed independently to achieve proper convergence. Regions 1 and 11 have coarse mesh and regions 2, 3, 9 and 10 have a finer mesh. Regions 5, 6 and 7 are the main regions that are studied for failure. Region 6 has a very fine mesh with all the elements of uniform length. Stress concentrations and failures are mostly observed in this section. Regions 5 and 7 have biased mesh of with coarseness increasing

as we move away from the center of the specimen. Mesh in regions 4 and 8 are also biased but relatively coarse. The displacement is applied at 3 center nodes on the top layer of region 6. Nodes on the bottom layer of regions 2 and 3 are fixed while nodes bottom layer nodes on 9 and 10 are fixed in x- direction.

For mesh along y-direction, the $[0_2/90_2]_{2s}$ beam is divided into 15 parts as in Figure 4.7. Parts 1, 5, 11 and 15 are for the $[0]_2$ layer while parts 3, 7, 9, and 13 are for $[90]_2$ layer. The layers 2, 4, 6, 8, 10, 12 and 14 work as the cohesive layer interface between the elastic layers. Each elastic layer has 3 elements in the y-direction.

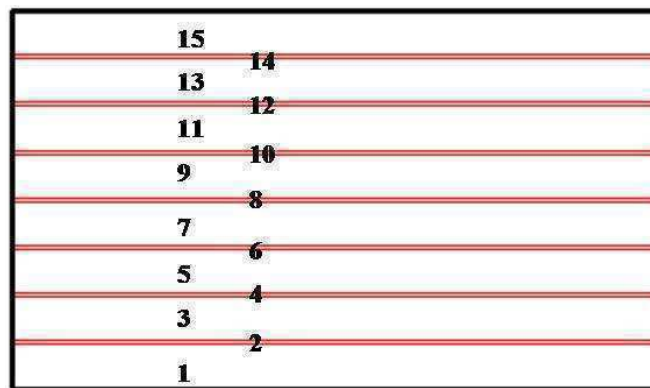


Figure 4.7: Partitioning of flexure specimen in thickness direction

Figure 4.8 shows the mesh used for the analysis with cohesive layers shown in dotted lines.

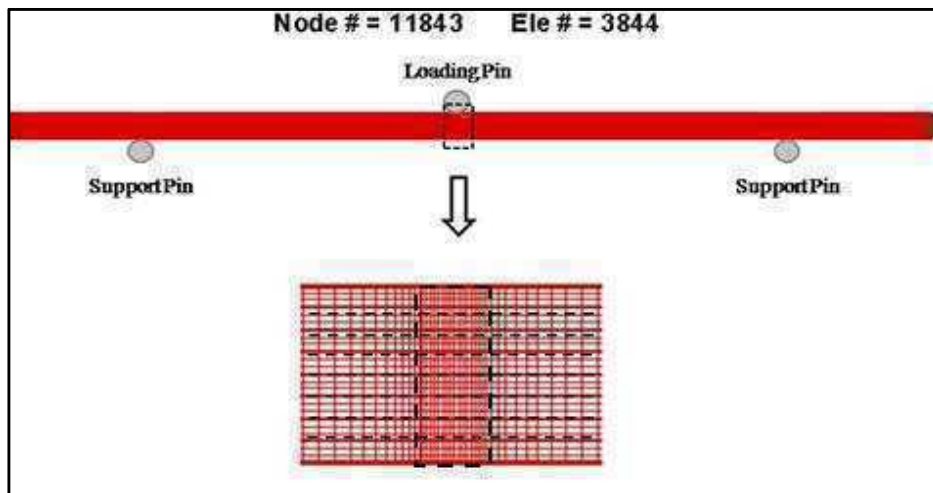


Figure 4.8: FEA macro-model of flexure specimen

A convergence study was carried out to achieve optimum mesh size. The load displacement curves for geometries with various mesh sizes are plotted below in Figure 4.9. Table 4.1 shows the load-displacement values for different mesh sizes. The mesh with 3780 elements was found to be optimum for the required geometry and layup.

Table 4.1: Load and displacement values for different mesh sizes

Total no. of elements	Max load (N)	Max displacement (mm)
2090	481.90	2.07
2584	444.12	1.90
2660	431.34	1.86
3780	394.05	1.71
4980	397.31	1.74
6000	376.78	1.69

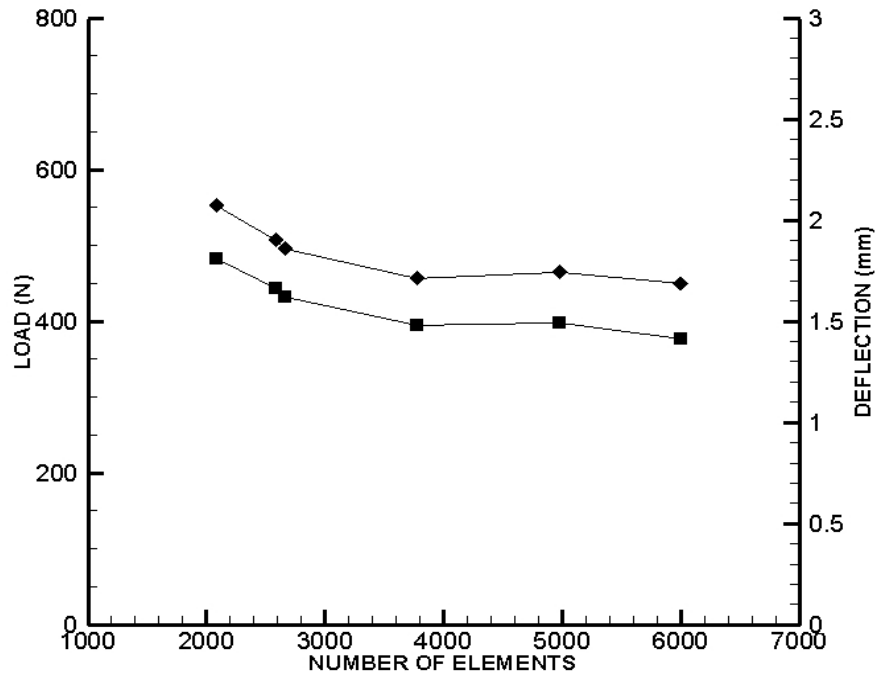


Figure 4.9: Convergence study with different mesh sizes

4.4.2 Boundary conditions

In order to simulate the experimental conditions, the NOVA-3D model is controlled using displacement as an input parameter with the load as the output. The displacement is incremented per load step to get two displacement rates, 0.01 in/min and 1.00 in/min. The displacement is applied to three nodes and average reaction at these nodes is calculated to determine the load carried by the beam. A study was conducted on the relation between the load and the number of nodes on which displacement is applied. The optimum number of nodes was found to be three. Using only one node gave higher values of load and five nodes gave lower value as compared to experimental results.

4.4.3 Elastic material properties

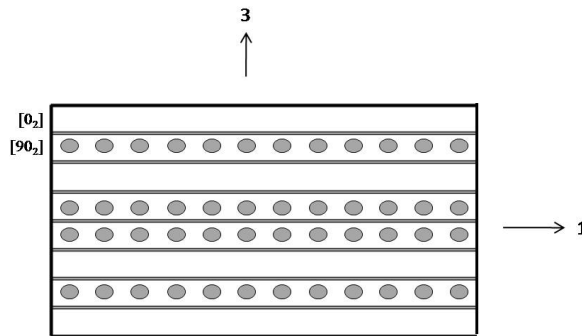


Figure 4.10: Schematic of $[0_2/90_2]_{2s}$ specimen

Material properties are assigned to the different layers of the composite beam in the global co-ordinate system (Figure 4.10). For the $[0]$ layer, the fiber is aligned with the 1-axis while for the $[90]$ layer the fiber is transverse to the 1-axis. For both cases, out-of-plane properties are assigned in the 3-direction. Shear modulus, volume fraction, Poisson's ratio and Young's modulus are the material properties required for the analysis. Keeping all other values constant for ease of computation, Young's modulus of the $[0]$ and $[90]$ layers are modified to match the bending stiffness of the modeled load-displacement plot with the experimental bending stiffness. The material properties for the unaged specimen are similar to those used by Camanho and Matthews (Camanho,1999)

4.4.4 Cohesive material properties

The stiffness of cohesive elements is same as the elastic elements before damage occurs. Once damage occurs in the material, the cohesive properties are degraded according to the specified cubic traction-separation law. This law is derived in the subsequent section. For the $[0]$ layer in compression, the stiffness is

$$C_{11C} = \begin{cases} \frac{27 \sigma_{maxC}}{4 \varepsilon_{maxC}} & 0 \leq \bar{\varepsilon}_{xC} < 0.3333 \\ \frac{27 \sigma_{maxC}}{4 \varepsilon_{maxC}} [1 - \delta(\bar{\varepsilon}_{xC} - \bar{\varepsilon}_{xC}^2)] & \text{if } 0.3333 \leq \bar{\varepsilon}_{xC} < 1 \\ 0 & 1 \leq \bar{\varepsilon}_{xC} \end{cases}$$

where $\bar{\varepsilon}_{xC}$ is normalized strain in the element

$\delta=1$ when $\bar{\varepsilon}_{xC} \geq 0.3333$

σ_{maxC} is the longitudinal compressive strength

ε_{maxC} is the maximum longitudinal compressive strain at initial failure

Similarly, the properties for tensile, compressive and shear elements for [0] and [90] layers are calculated.

4.4.5 Cohesive Layer Constitutive Equations

Based on fundamental principles of continuum mechanics, for two-dimensional case, a cubic cohesive layer constitutive relationship has been employed by Needleman (Needelman, 1987) for debond growth. The flexure specimens in consideration are cross-ply of $[0_2/90_2]_{2s}$ configuration. These specimens show progressive failure consisting of compressive fiber wrinkling, delaminations, matrix cracks and tensile failure. The cohesive layer model has been modified to incorporate compressive and tensile failures and shear delaminations. The derivation for constitutive equations for the [0] and [90] layer is as follows:

(i) For [90] cohesive layer

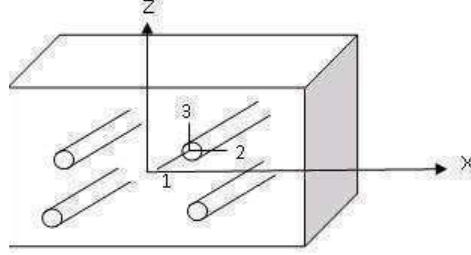


Figure 4.11: 2-D RVE for [90] layer

Assuming plane stress condition in RVE in the X-Z plane,

$$\begin{Bmatrix} \sigma_x \\ \sigma_z \\ \tau_{xz} \end{Bmatrix} = \begin{bmatrix} Q_{22} & Q_{23} & 0 \\ Q_{23} & Q_{33} & 0 \\ 0 & 0 & Q_{44} \end{bmatrix} \begin{Bmatrix} \varepsilon_x \\ \varepsilon_z \\ \gamma_{xz} \end{Bmatrix} ; \varepsilon_y \neq 0 \quad (10)$$

Where,

$$Q_{22} = \frac{E_2}{1 - \nu_{23}\nu_{32}} \quad (11)$$

$$Q_{33} = \frac{E_3}{1 - \nu_{23}\nu_{32}} = Q_{22} ; \quad (E_2 = E_3) \quad (12)$$

$$Q_{23} = \frac{\nu_{32}E_2}{1 - \nu_{23}\nu_{32}} \quad (13)$$

$$Q_{44} = G_{23} = \frac{E_2}{2(1 + \nu_{23})} = \frac{(1 - \nu_{23}^2)}{2(1 + \nu_{23})} Q_{22} = \frac{(1 - \nu_{23})}{2} Q_{22} \quad (14)$$

Assuming that the transverse matrix crack is detected in the 3-D RVE, then the cohesive layer model is invoked within the framework of the 2-D plane stress RVE as follows,

Assume

$$\sigma_x = \frac{27}{4} \sigma_{maxT} [\bar{\varepsilon}_x - \delta(2\bar{\varepsilon}_x^2 - \bar{\varepsilon}_x^3)] \quad (15)$$

Where $\delta=1$ indicates cohesive failure; $\delta=0$ indicates no failure.

Eqn(15) can be rewritten as,

$$\sigma_x = \frac{27}{4} \left(\frac{\sigma_{maxT}}{\varepsilon_{max}} \right) [1 - \delta(2\bar{\varepsilon}_x - \bar{\varepsilon}_x^2)] \varepsilon_x \quad (16)$$

Comparing eqn (16) with eqn (10) for the case of uniaxially loaded RVE without damage ($\delta=0$),

$$\sigma_x = Q_{22} \varepsilon_x = \frac{27}{4} \left(\frac{\sigma_{maxT}}{\varepsilon_{maxT}} \right) \varepsilon_x \quad (17)$$

From eqn (18),

$$\sigma_{maxT} = \frac{4}{27} \left(\frac{E_2}{1 - \nu_{23}\nu_{32}} \right) \varepsilon_{maxT} \quad (18)$$

After failure has been detected in 3-D RVE, the material stiffness matrix in the 2-D RVE is given by,

$$\begin{Bmatrix} \sigma_x \\ \sigma_z \\ \tau_{xz} \end{Bmatrix} = \frac{27}{4} \left(\frac{\sigma_{maxT}}{\varepsilon_{maxT}} \right) [1 - \delta(2\bar{\varepsilon}_x - \bar{\varepsilon}_x^2)] \begin{bmatrix} 1 & \nu_{23} & 0 \\ \nu_{23} & 1 & 0 \\ 0 & 0 & \frac{(1 - \nu_{23})}{2} \end{bmatrix} \begin{Bmatrix} \varepsilon_x \\ \varepsilon_z \\ \gamma_{xz} \end{Bmatrix}$$

Here, the underlying assumption is that transverse isotropy remains valid even after the onset of damage.

Evaluation of ε_{maxT} :

At the onset of damage,

$$\frac{d\sigma_x}{d\bar{\varepsilon}_x} = 0 \quad (19)$$

$$\frac{27}{4} \sigma_{max} [1 - 4\bar{\varepsilon}_{xD} + 3\bar{\varepsilon}_{xD}^2] = 0$$

$$\bar{\varepsilon}_{xD}^2 - 4\bar{\varepsilon}_{xD} + 1 = 0$$

$$\bar{\varepsilon}_{xD} = \frac{1}{3}$$

But

$$\bar{\varepsilon}_{xD} = \frac{\varepsilon_{3DFT}}{\varepsilon_{xmaxT}} = \frac{1}{3}$$

$$\varepsilon_{xmaxT} = \varepsilon_{x3DFT} \text{ (known from 3D RVE, described in section 4.5)} \quad (20)$$

(ii) For [0] cohesive Layer

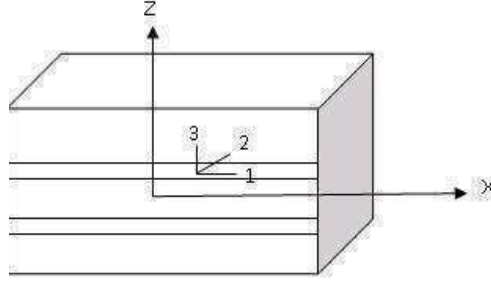


Figure 4.12: 2-D RVE for [0] layer

Assuming plane stress condition in RVE in the X-Z plane,

$$\begin{Bmatrix} \sigma_x \\ \sigma_z \\ \tau_{xz} \end{Bmatrix} = \begin{bmatrix} Q_{11} & Q_{13} & 0 \\ Q_{13} & Q_{33} & 0 \\ 0 & 0 & Q_{55} \end{bmatrix} \begin{Bmatrix} \varepsilon_x \\ \varepsilon_z \\ \gamma_{xz} \end{Bmatrix} ; \varepsilon_y \neq 0 \quad (21)$$

Where,

$$\left. \begin{aligned} Q_{11} &= \frac{E_1}{1 - \nu_{13}\nu_{31}} \\ Q_{33} &= \frac{E_3}{1 - \nu_{13}\nu_{31}} \\ Q_{13} &= \frac{\nu_{31}E_1}{1 - \nu_{13}\nu_{31}} \\ Q_{55} &= G_{13} \end{aligned} \right\} \quad (22)$$

Assuming longitudinal fiber fracture is detected in the 3-D RVE, the cohesive layer model is activated in the 2-D RVE as shown

$$\sigma_x = \frac{27}{4} \sigma_{maxL} [\bar{\varepsilon}_x - \delta(2\bar{\varepsilon}_x^2 - \bar{\varepsilon}_x^3)] \quad (23)$$

Where $\delta=1$ indicates failure; $\delta=0$ indicates no failure.

Similar to [90] layer, for uniaxial loading,

$$\begin{aligned}\sigma_x &= Q_{11}\varepsilon_x = \frac{27}{4} \left(\frac{\sigma_{maxL}}{\varepsilon_{maxL}} \right) \varepsilon_x \\ \sigma_{maxL} &= \frac{4}{27} Q_{11}\varepsilon_{maxL} = \frac{4}{27} \left(\frac{E_1}{1 - \nu_{13}\nu_{31}} \right) \varepsilon_{maxL}\end{aligned}\quad (24)$$

Evaluation of ε_{maxL} :

Similar to the transverse failure condition, at the onset of the tensile damage in the [0] layer,

$$\begin{aligned}\bar{\varepsilon}_{xD} &= \frac{\varepsilon_{x3DFL}}{\varepsilon_{xmaxL}} = \frac{1}{3} \\ \varepsilon_{xmaxL} &= 3\varepsilon_{x3DFL}\end{aligned}\quad (25)$$

Stress-Strain Relation for [0] layer

$$\begin{Bmatrix} \sigma_x \\ \sigma_z \\ \tau_{xz} \end{Bmatrix} = \begin{bmatrix} \frac{27}{4} \left(\frac{\sigma_{maxL}}{\varepsilon_{maxL}} \right) [1 - \delta(2\bar{\varepsilon}_x - \bar{\varepsilon}_x^2)] & \frac{\nu_{31}E_1}{1 - \nu_{13}\nu_{31}} & 0 \\ \frac{\nu_{31}E_1}{1 - \nu_{13}\nu_{31}} & \frac{E_3}{1 - \nu_{13}\nu_{31}} & 0 \\ 0 & 0 & \frac{27}{4} \left(\frac{\tau_{max}}{\gamma_{max}} \right) [1 - \delta(2\bar{\gamma}_x - \bar{\gamma}_x^2)] \end{bmatrix} \begin{Bmatrix} \varepsilon_x \\ \varepsilon_z \\ \gamma_{xz} \end{Bmatrix}$$

4.5 Direct Micromechanical Model for 3-D Local Strains from 2-D Global Strains

In order to incorporate the stress amplification due to the presence of micro-scale inhomogeneities, a finite element analysis based micromechanics method called Direct Micromechanical Model (DMM) was developed to investigate development of micro-cracks in a carbon/epoxy laminate. The unit cell of the composite was modeled using three-dimensional finite elements. Periodic boundary conditions were applied to the boundaries of the unit cell. The stresses in the fiber and matrix phases and along the fiber–matrix interface were calculated. When the laminated composite structure was subjected to combined thermal and mechanical loads, the macro-strains were computed from the global analysis. The macro-strains were then

applied to the unit hexagonal cell model to evaluate micro-stresses, which were used to predict the formation of micro-cracks in the matrix.

The microscopic image of a uniaxial fiber-reinforced laminate (Figure 4.13) shows that the fiber arrangement is quite random in reality. However, for analytical/numerical modeling, it is convenient to assume some repetitive pattern of fiber arrangement. The hexagonal pattern of unit cell, as shown in Figure 4.14 was used to model the RVE as it is closer to reality than square packing pattern, especially when the composite is fabricated with high fiber volume fraction. Theoretically, one can obtain a maximum fiber volume fraction of 91% with hexagonal RVE.

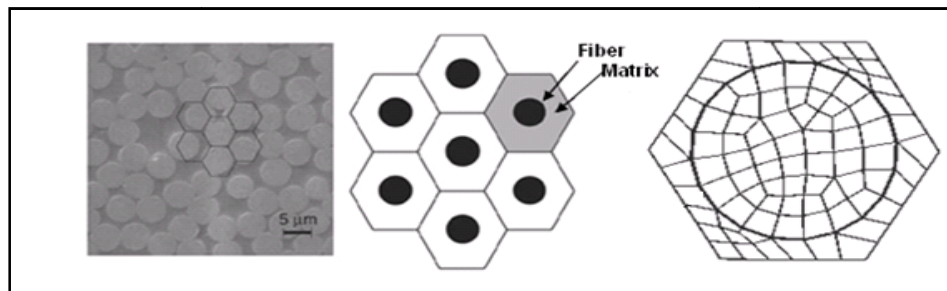


Figure 4.13: Hexagonal packing and corresponding FEM mesh

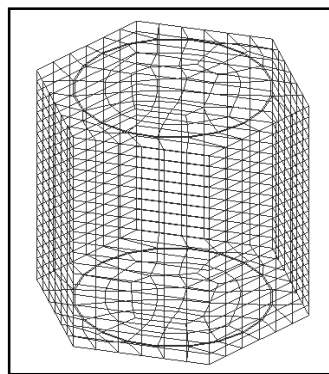


Figure 4.14: Hexagonal unit cell 3-D mesh

Periodic boundary condition was used for the hexagonal unit cell. The periodic boundary conditions ensure displacement compatibility and stress continuity on the opposite faces of the unit cell.

4.5.1 Boundary conditions of hexagonal unit cell

The unit cells were subjected to axial and shear displacements using periodic boundary conditions. The periodic boundary conditions maintain equal boundary displacements with the adjacent unit cells to satisfy the compatibility of displacements on opposite faces of the unit cell and enforce the continuity of stresses. The hexagonal unit cell was subjected to different strain components individually using the periodic boundary conditions shown in Table 4.2. The equations of periodic boundary conditions corresponding to individual unit strains were applied in ABAQUS to perform the FE analysis.

Table 4.2: Periodic boundary conditions for the hexagonal unit cell for the application of unit magnitude of various strain components

$\varepsilon_x=1$	$\varepsilon_y=1$	$\varepsilon_z=1$	$\gamma_{xy}=1$	$\gamma_{xz}=1$	$\gamma_{yz}=1$
$u_{a1} - u_{a0} = \sqrt{3}L/2$	$u_{a1} - u_{a0} = 0$	$u_{a1} - u_{a0} = 0$	$u_{a1} - u_{a0} = 0$	$u_{z1} - u_{z0} = 0$	$v_{z1} - v_{z0} = 0$
$u_{b1} - u_{b0} = \sqrt{3}L/2$	$u_{b1} - u_{b0} = 0$	$u_{b1} - u_{b0} = 0$	$u_{b1} - u_{b0} = 0$	$u_{c1} = 0$	$w_{c1} = L/2$
$v_{a1} - v_{a0} = 0$	$v_{a1} - v_{a0} = L/2$	$v_{a1} - v_{a0} = 0$	$u_{c1} = 0$	$u_{c0} = 0$	$w_0 = -L/2$
$v_{b1} - v_{b0} = 0$	$v_{b1} - v_{b0} = L/2$	$v_{b1} - v_{b0} = 0$	$u_{c0} = 0$	$v_{c1} = 0$	$w_{a1} - w_{a0} = L/2$
$v_{c1} = 0$	$v_{c1} = L/2$	$v_{c1} = 0$	$v_{a1} - v_{a0} = \sqrt{3}L/2$	$v_{c0} = 0$	$w_{b0} - w_{b1} = L/2$
$v_{c0} = 0$	$v_{c0} = -L/2$	$v_{c0} = 0$	$v_{b1} - v_{b0} = -\sqrt{3}L/2$	$w_{a1} - w_{a0} = \sqrt{3}L/2$	
$w_{z1} - w_{z0} = 0$	$w_{z1} - w_{z0} = 0$	$w_{z1} - w_{z0} = t$	$w_{z1} - w_{z0} = t$	$w_{b1} - w_{b0} = \sqrt{3}L/2$	

Local 3-D strains at three critical points 1, 2 and 3 (Figure 4.15) were detected using periodic boundary conditions applied on the hexagonal RVE. Transformation matrices obtained using periodic boundary condition at the three locations 1, 2, and 3 are shown in Table 4.3.

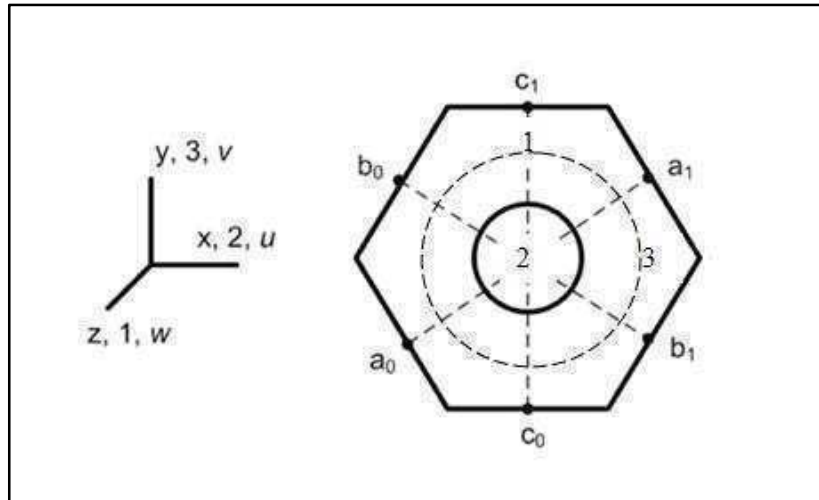


Figure 4.15: Geometry of hexagonal unit cells

Table 4.3: Local 3D strains at three critical locations(1,2,3) from periodic boundary conditions

Point 1						
	$e_{xx}=1$	$e_{yy}=1$	$e_{zz}=1$	$e_{xy}=1$	$e_{xz}=1$	$e_{yz}=1$
e11	0.0042	-0.0816	0.3284	0.0264	0	0
e22	0.0100	0.6787	0.3616	0.1292	0	0
e33	0	0	1	0	0	0
e12	0.0099	0.7911	-0.0031	0.2378	0	0
e13	0	0	0	0	0.0074	-0.0365
e23	0	0	0	0	-0.0070	1.1048
Point 2						
	$e_{xx}=1$	$e_{yy}=1$	$e_{zz}=1$	$e_{xy}=1$	$e_{xz}=1$	$e_{yz}=1$
e11	0.0049	-0.0021	0.3285	0.0003	0	0
e22	-0.0019	0.0052	0.3306	0.0002	0	0
e33	0	0	1	0	0	0
e12	0.0005	-0.0007	0	0.007	0	0
e13	0	0	0	0	0.0096	0
e23	0	0	0	0	0.0002	0.0097
Point 3						
	$e_{xx}=1$	$e_{yy}=1$	$e_{zz}=1$	$e_{xy}=1$	$e_{xz}=1$	$e_{yz}=1$
e11	0.0013	-0.0334	0.3650	0.0176	0	0
e22	-0.0080	0.0265	0.3336	0.0110	0	0
e33	0	0	1	0	0	0
e12	0.0309	0.0673	0.0154	0.2304	0	0
e13	0	0	0	0	0.1028	0.0159
e23	0	0	0	0	0.0044	0.0133

CHAPTER 5

EXPERIMENTAL RESULTS AND DISCUSSIONS

5.1 Environmental Ageing

5.1.1 Moisture Desiccation

The $[0_2/90_2]_{2s}$ cross-ply panels were placed in a desiccator with silica crystals at 160°F for approximately 15 days. Figure 5.1 shows desorption of the cross-ply panels. After losing approximately 1.12% moisture, the weight of the panel remained constant.

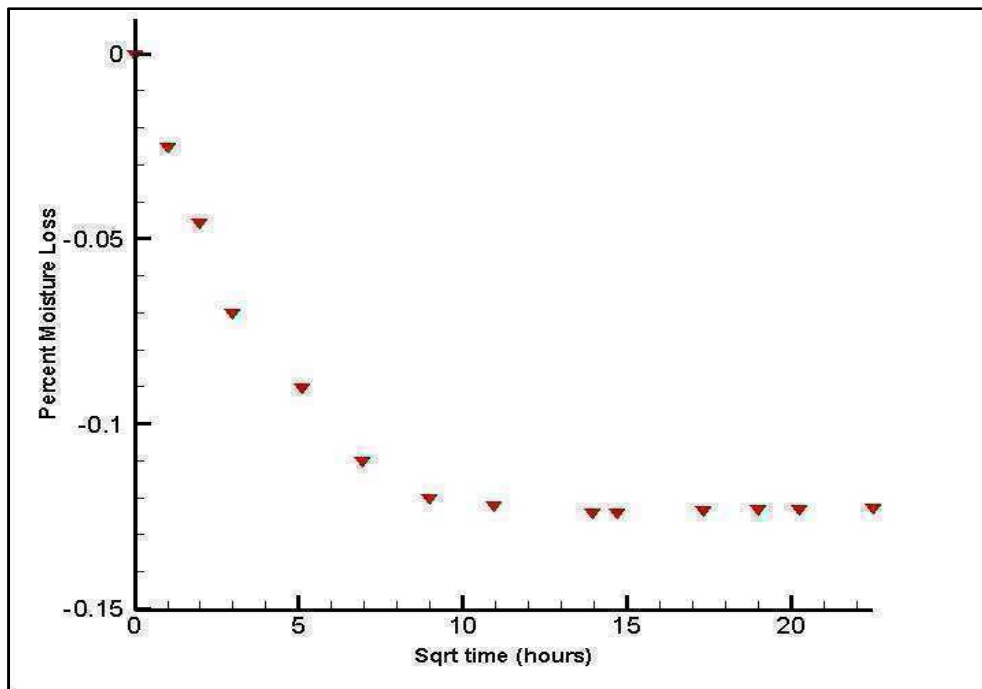


Figure 5.1 Desiccation of cross-ply flexure specimens

5.1.2 Moisture Absorption

After desiccation, the panels were aged under various ageing conditions as described in Chapter 3. Weight readings of the panels in wet (immersed) conditions were recorded at regular time intervals in order to calculate moisture weight gain in them. The dry panels were not weighed as the weight is assumed to remain constant throughout their ageing period. Figure 5.2 and Figure 5.3 show the moisture absorption of unstressed and stressed flexure specimens, i.e. HWU, CWU, HWS and CWS.

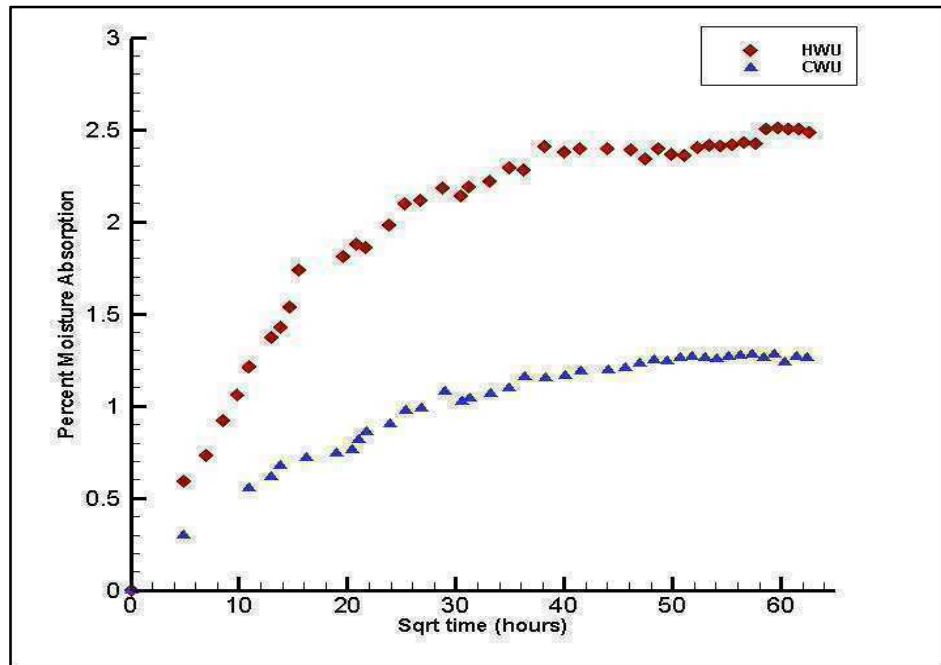


Figure 5.2: Moisture absorption of unstressed cross-ply flexure specimens

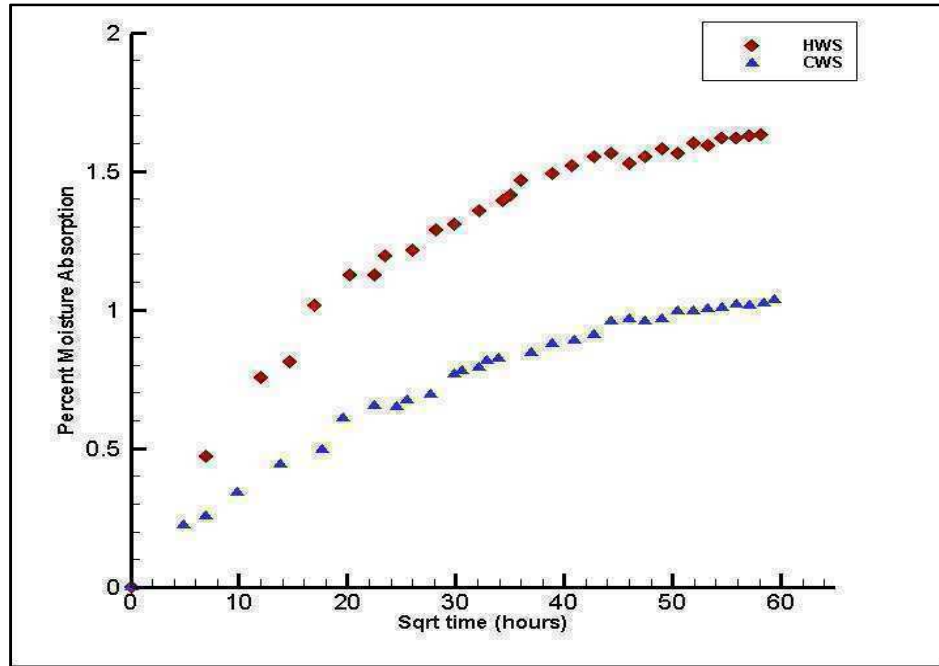


Figure 5.3: Moisture absorption of stressed cross-ply flexure specimens

Ficks law fit was applied to the moisture absorption data for all immersed cases to get values of diffusivity and maximum saturation content (M_{inf}). Figures 5.4 and 5.5 show the Fick's law fit for unstressed and stressed cases respectively. The values of diffusivity and M_{inf} are tabulated in Table 5.1.

Table 5.1: Diffusivity and M_{inf} from Ficks law fit

Ageing Condition	Diffusivity (10^{-9}) (cm^2/s)	M_{inf} (grams)
HWU	8.3672	1.5205
CWU	5.1205	0.7980
HWS	5.6107	0.9385
CWS	3.8635	0.6429

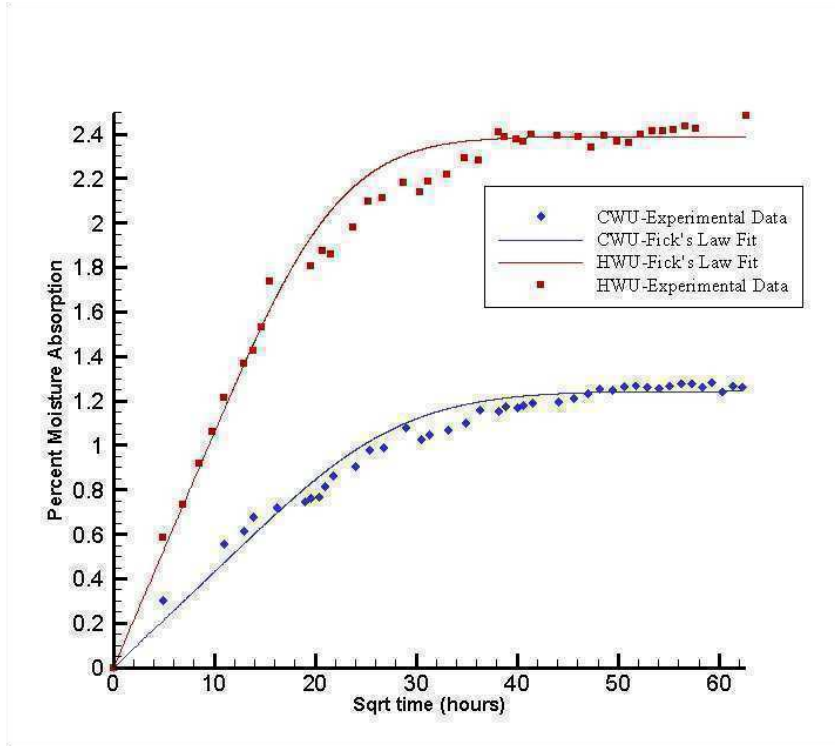


Figure 5.4: Ficks law fit for HWU and CWU panels

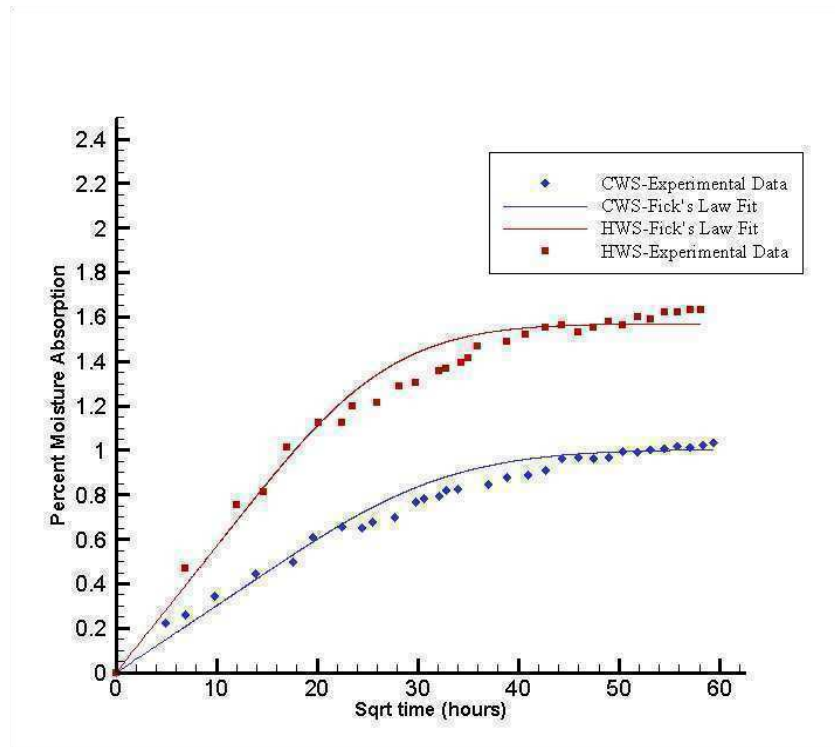


Figure 5.5: Ficks law fit for HWS and CWS panels

5.2 Test Results

Flexure tests were performed on cross-ply specimens at two displacement rates $R_1=0.01$ in/min and $R_2=1.00$ in/min, for all ageing conditions. The specimens are loaded till complete failure in order to observe the progressive failure of cross-ply specimens. The initial failure was observed due to fiber wrinkling in the outermost ply which was under compression. The failure was observed to progress in the form of delamination and matrix cracks in the middle 90 layers. Finally, failure of the outer $[0^\circ]$ tensile layer led to the ultimate failure of the specimen. Figure 5.6 shows all the failure modes of an unaged specimen loaded in three-point bend configuration.

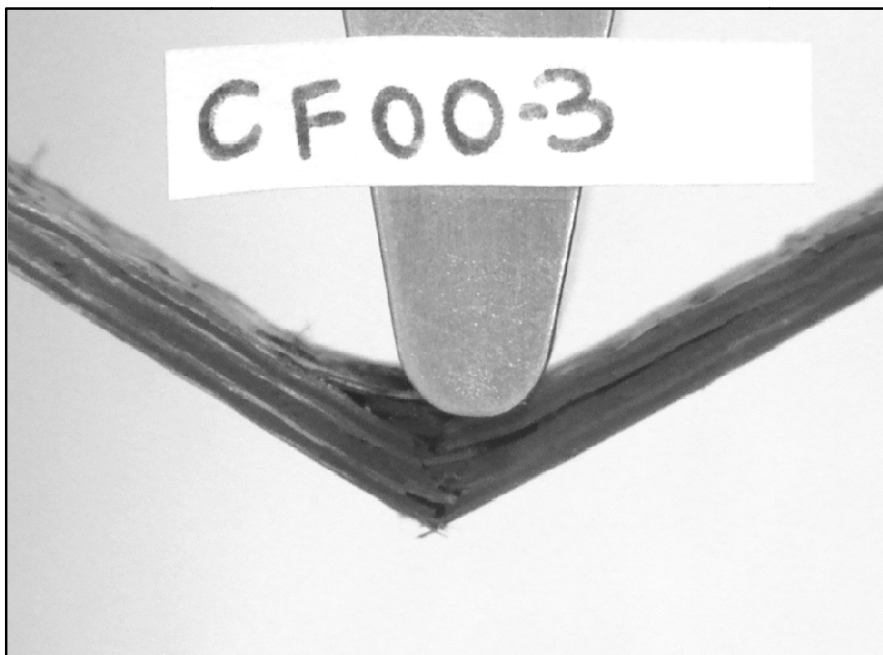


Figure 5.6: Failed specimen

Tests at ageing time ' t_1 ' were performed on the specimens when they reached complete saturation. The HWU panels reached saturation at approximately 2544 hours. The HDU panels were also removed at this time for ageing. The CWU panels reached saturation at approximately

2680 hours and the CWU and CDU panels were synchronously removed for testing. Similarly, the ageing times for the remaining panels were also decided based on saturation.

Figure 5.7 shows the percentage change in flexural strength compared to the control unaged panels. It can be seen that the HWU1 specimens had maximum strength reduction, approximately 26% while the CWU1 specimens lost approximately 22% strength compared with the baseline specimen. The HDU1 and CDU1 specimens showed degradation of approximately 45% and showed delamination of the top layers before compressive failure. A number of possible reasons were found which led to this change in failure mode, some of which were fiber misalignment, large number of voids in the specimens and poor inter-lamina compaction, i.e. poor sample quality and hence, the data of these samples were discarded. The HWS1 and CWS1 specimens saturated at approximately 2300 hours which shows that the rate of diffusion increased due to the stress applied, however, the total moisture uptake does not seem to be affected by the stress applied. The degradation in strength for the HWS1 and CWS1 cases is approximately 22% and 19%. The dry specimens showed loss of approximately 6% for HDS1 and 2% for CDS1.

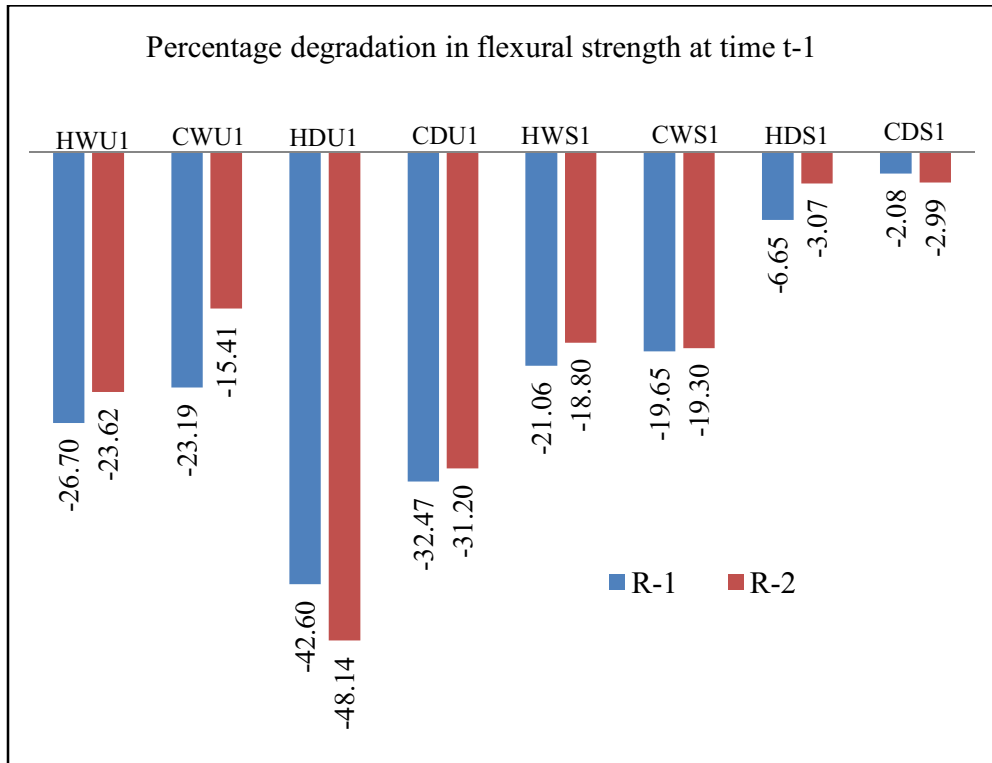


Figure 5.7: Comparison of R₁ and R₂ for 't₁' testing of flexure specimens

Tests at ageing time 't₂' were performed approximately 750 hours after t₁ and t₃ tests were performed approximately 750 hours after t₂. Figures 5.8 and 5.9 show percentage degradation in flexural strength as compared to control unaged specimens. Figures 5.10 and 5.11 summarize flexural strength degradation of all aged specimens with respect to time. Maximum decrease in strength was seen in t₁ samples, while the strength showed little or no degradation at t₂ and t₃. A clear separation in strength of wet and dry specimens is seen. This establishes the fact that although temperature had some effect on the degradation, moisture played a key role in the degradation mechanism. No significant synergistic effect of stress induced degradation was observed in the tests performed.

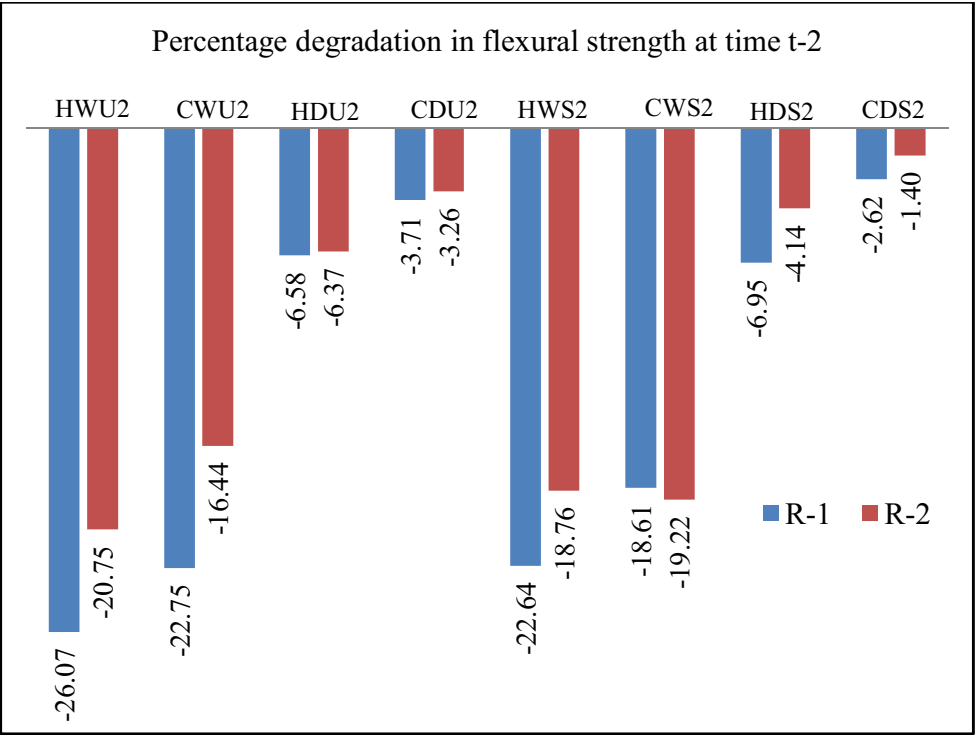


Figure 5.8: Comparison of R₁ and R₂ for 't₂' testing of flexure specimens

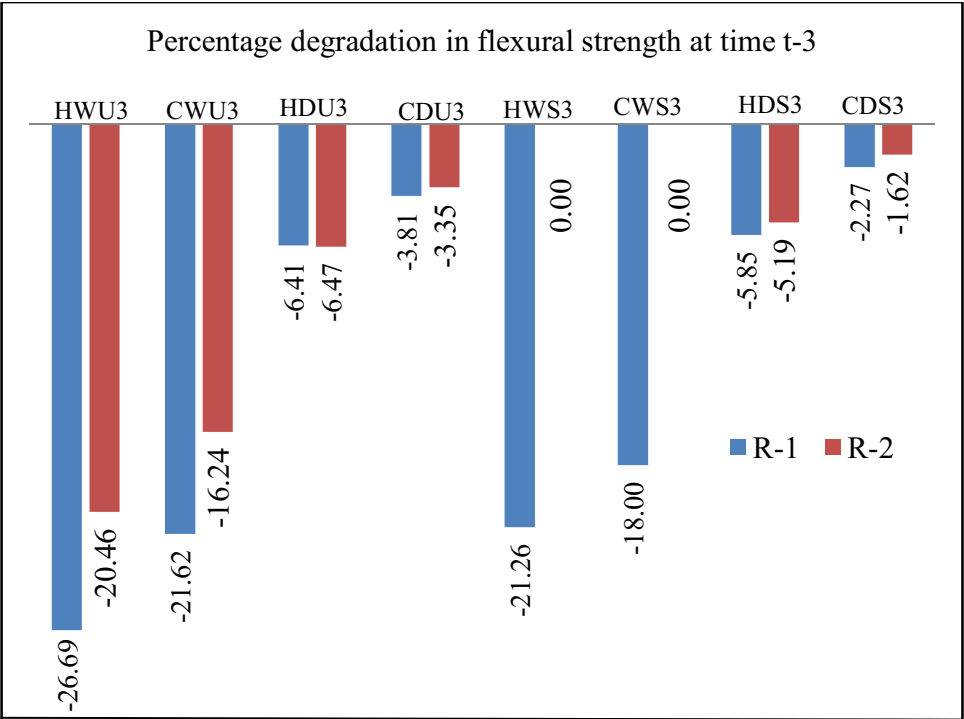


Figure 5.9: Comparison of R₁ and R₂ for 't₃' testing of flexure specimens

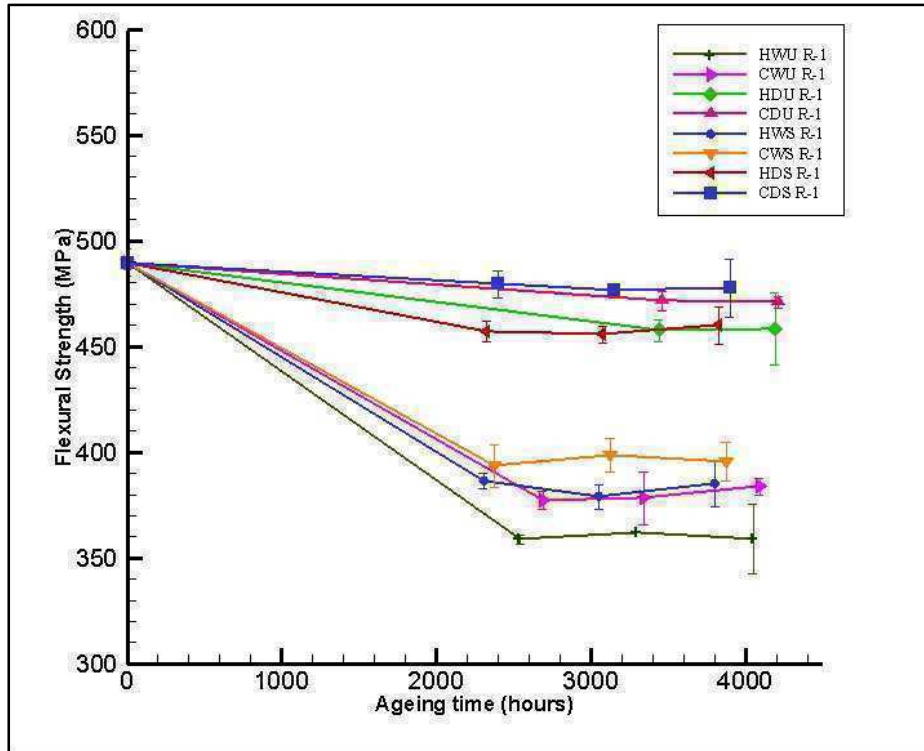


Figure 5.10: Flexural strength degradation with time for $R_1=0.01\text{in/min}$

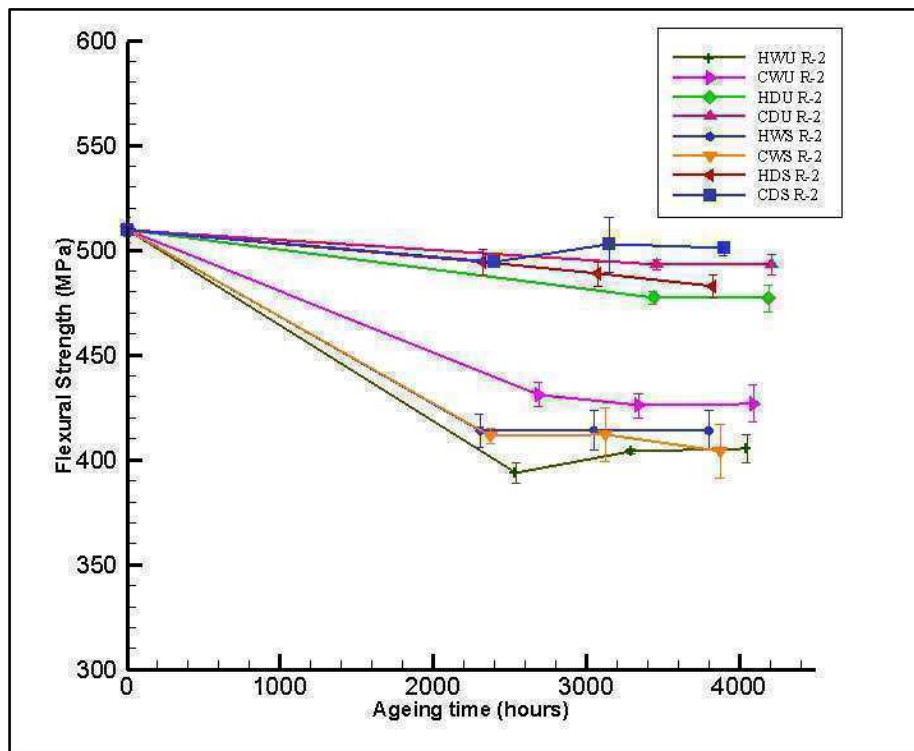
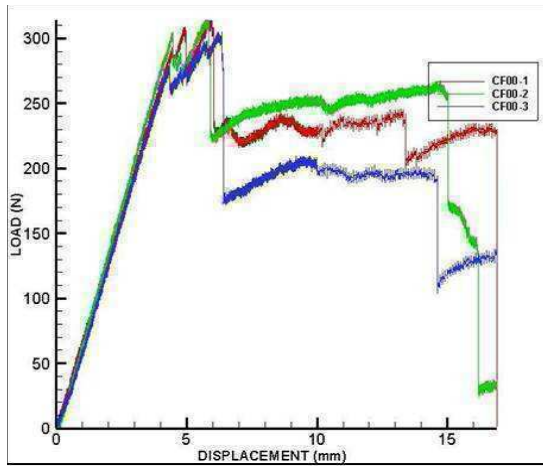


Figure 5.11: Flexural strength degradation with time for $R_2=1.00\text{in/min}$

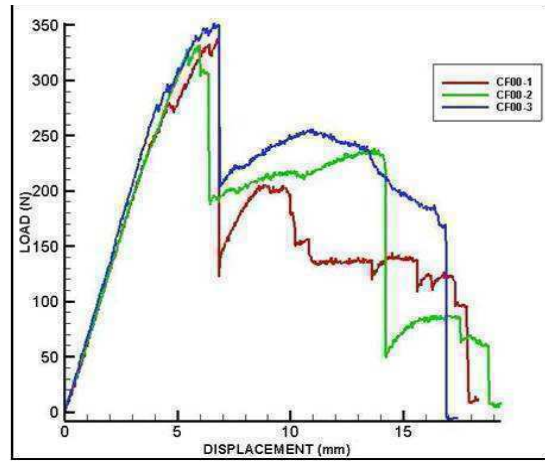
Figures 5.12-5.17 show the load-deflection curves for the specimens. It is worth noting that the thickness of the samples tested was not exactly uniform and varied from one sample to another due to manufacturing anomalies and swelling due to moisture absorption. Hence, degradation is not calculated based on change in load carrying capability of the specimen, but on the basis of flexural strength. Flexural strength takes into consideration the dimensional variability in the samples and hence, strength degradation is used to study the synergistic effect of environmental conditions on the degradation of carbon/epoxy composites.

The flexure strength of the specimens was slightly higher when tested at elevated strain rate. As can be seen from figures 5.7-5., at high strain rate the flexure specimens showed approximately 6% higher strength for some conditions while for others, the strength difference was only 0.5%. The progressive failure mechanism remained similar. The results from the tests are tabulated in Tables 5.2-5.7.

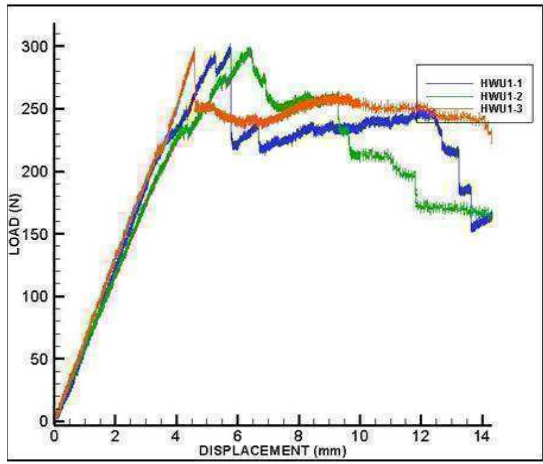
The critical wrinkling strain at which failure initiated on the compressive side of the flexure specimens is tabulated in Table 5.8 for all ageing conditions. The wrinkling initiation strain will subsequently be employed to predict failure initiation in composite laminates using a life prediction software.



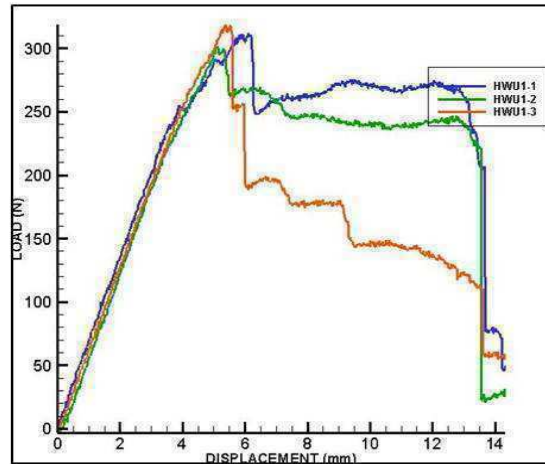
(a)



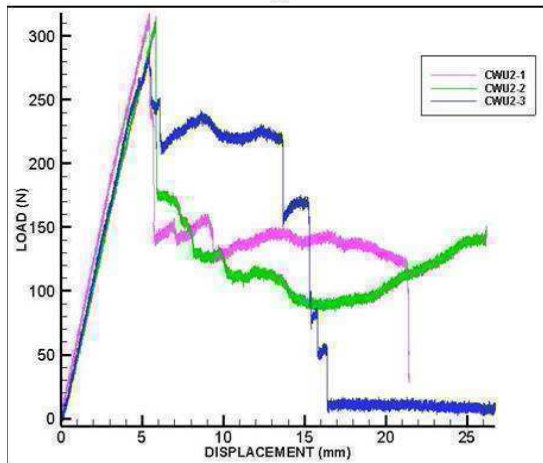
(b)



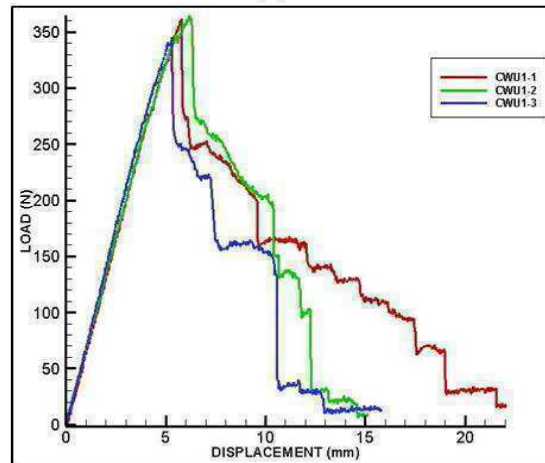
(c)



(d)



(e)



(f)

Figure 5.12: Load-Deflection curves (a)CF00-R₁ (b) CF00-R₂ (c) HWU1-R₁ (d) HWU1-R₂ (e) CWU1-R₁ (f)

CWU1-R₂

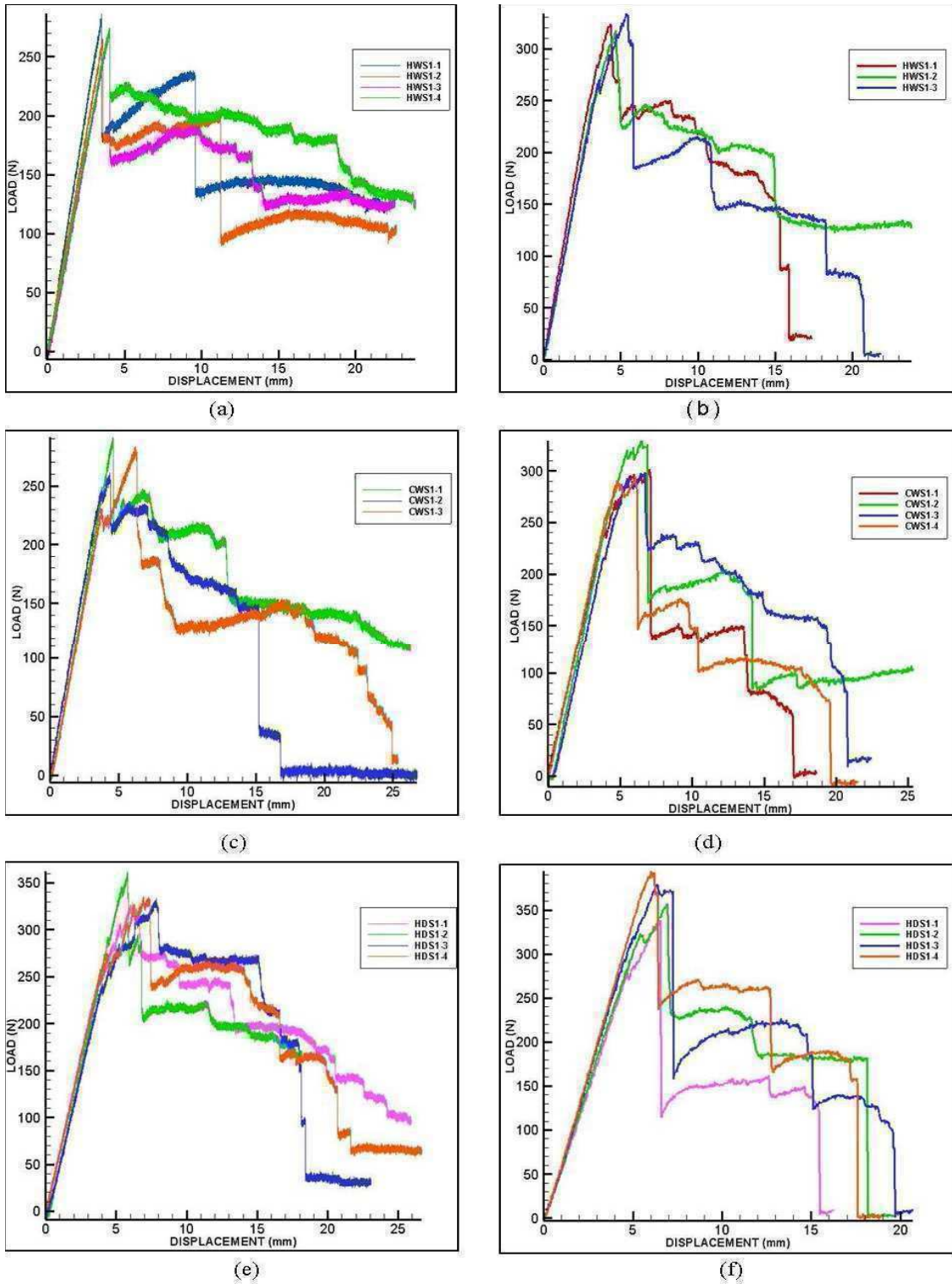


Figure 5.13: Load-Deflection curves (a) HWS1-R₁ (b) HWS1-R₂ (c) CWS1-R₁ (d) CWS1-R₂ (e) HDS1-R₁ (f)

HDS1-R₂

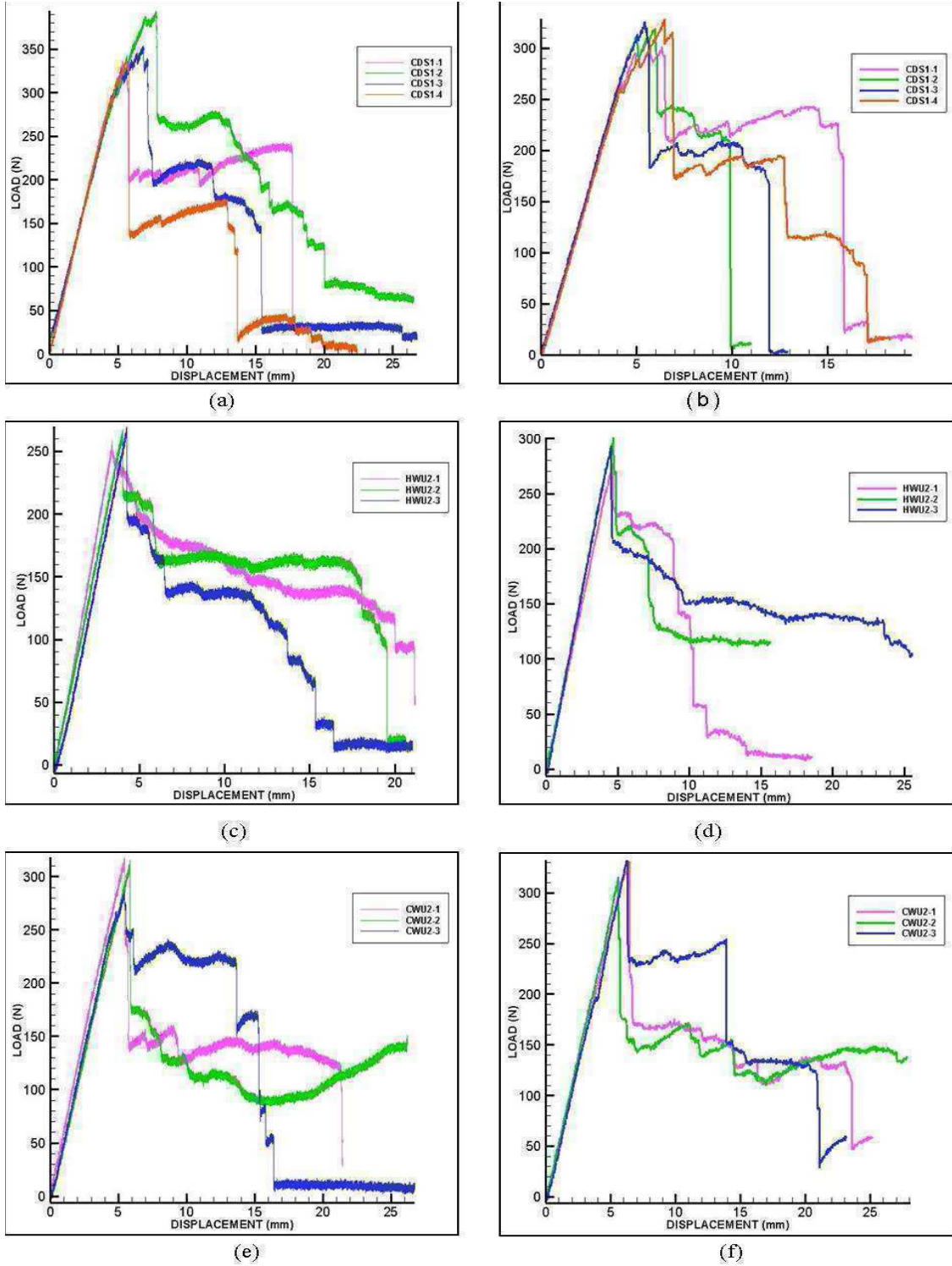


Figure 5.14: Load-Deflection curves (a) CDS1-R₁ (b) CDS1-R₂ (c) HWU2-R₁ (d) HWU2-R₂ (e) CWU2-R₁ (f) CWU2-R₂

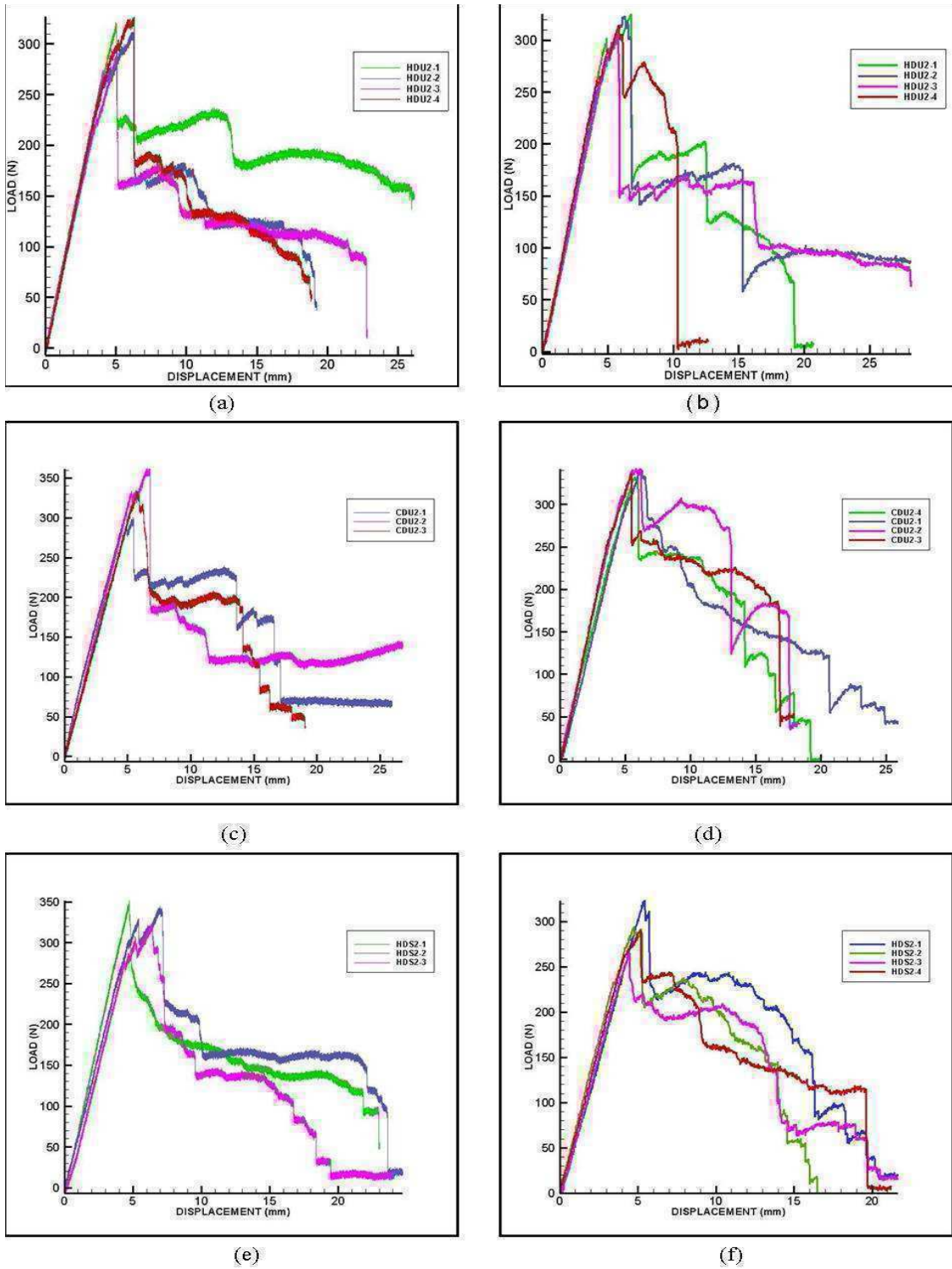
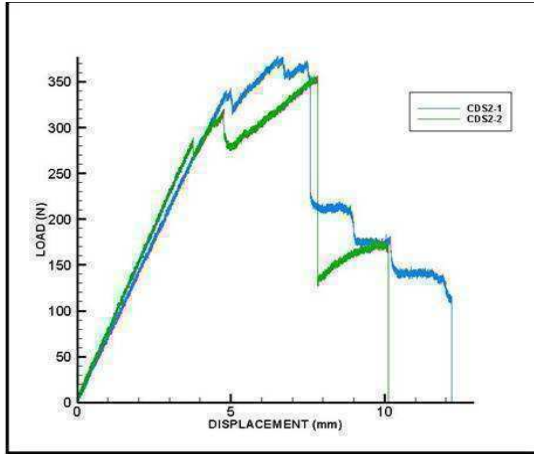
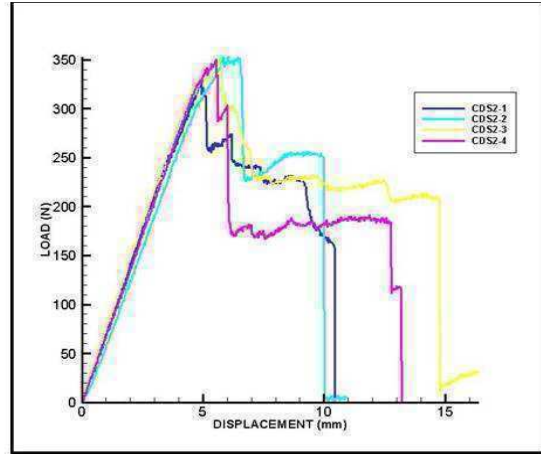


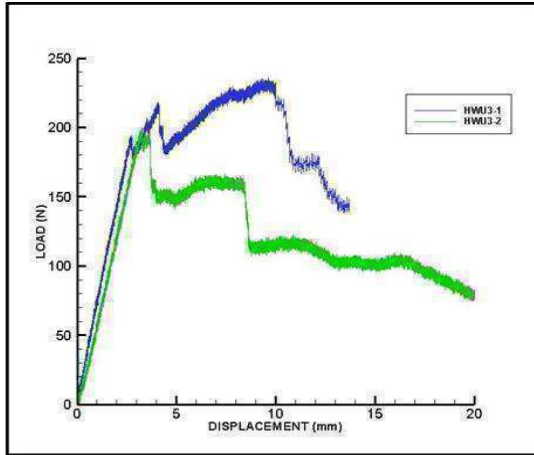
Figure 5.15: Load-Deflection curves (a) HDU2-R₁ (b) HDU2-R₂ (c) CDU2-R₁ (d) CDU2-R₂ (e) HDS2-R₁ (f) HDS2-R₂



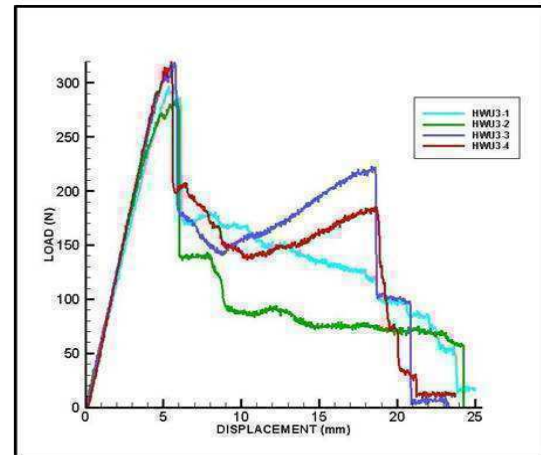
(a)



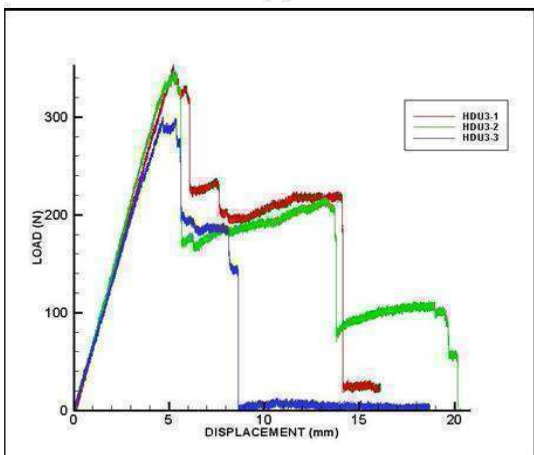
(b)



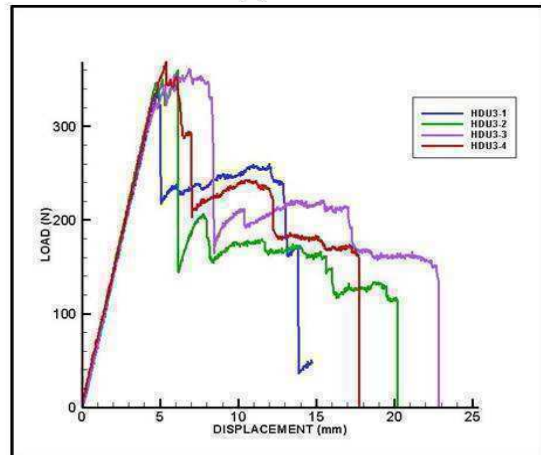
(c)



(d)



(e)



(f)

Figure 5.16: Load-Deflection curves (a) CDS2-R₁ (b) CDS2-R₂ (c) HWU3-R₁ (d) HWU3-R₂ (e) HDU3-R₁ (f) HDU3-R₂

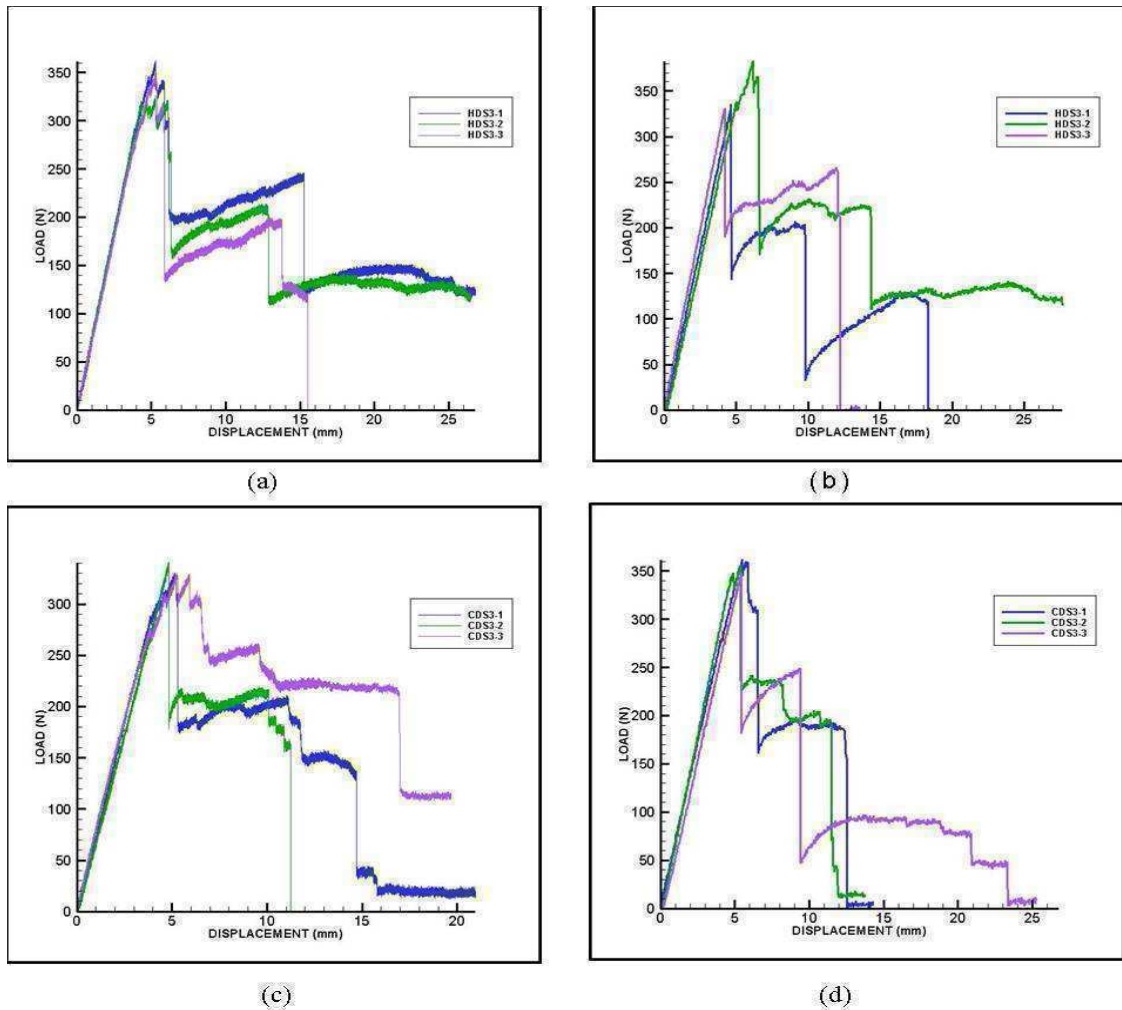


Figure 5.17: Load-Deflection curves (a) HDS3-R₁ (b) HDS3-R₂ (c) CDS3-R₁ (d) CDS3-R₂

Table 5.2: Flexural strength of specimens tested at ageing time t_1 and displacement rate R_1

	$t_1 - R_1$								
	CF00	HWU1	CWU1	HDU1	CDU1	HWU1	CWU1	HDS1	CDS1
Ageing time (hours)	0	2544	2688	2544	2688	2304	2376	2328	2400
Avg Strength (Mpa)	489.6	358.9	376.1	-	-	386.5	393.4	457.1	479.4
% Std. dev	6.3	2.2	4.3	-	-	3.5	9.8	4.8	6.3
% Change in flexural strength	0.0	-26.7	-23.2	-	-	-21.1	-19.6	-6.6	-2.1

Table 5.3: Flexural strength of specimens tested at ageing time t_2 and displacement rate R_1

$t_2 - R_1$									
	CF00	HWU1	CWU1	HDU1	CDU1	HWU1	CWU1	HDS1	CDS1
Ageing time (hours)	0	3294	3438	3294	3438	3054	3126	3078	3150
Avg Strength (Mpa)	489.6	362.0	378.3	457.4	471.5	378.8	398.5	455.6	476.8
% Std. dev	6.3	0.3	12.6	5.1	4.4	5.8	8.0	4.1	1.0
% Change in flexural strength	0.0	-26.1	-22.7	-6.6	-3.7	-22.6	-18.6	-7.0	-2.6

Table 5.4: Flexural strength of specimens tested at ageing time t_3 and displacement rate R_1

$t_3 - R_1$									
	CF00	HWU1	CWU1	HDU1	CDU1	HWU1	CWU1	HDS1	CDS1
Ageing time (hours)	0	4044	4188	4044	4188	3804	3876	3828	3900
Avg Strength (Mpa)	489.6	359.0	383.8	458.3	471.0	385.5	401.5	461.0	478.5
% Std. dev	6.3	16.6	3.9	17.1	5.9	1.1	0.9	4.8	3.8
% Change in flexural strength	0.0	-26.7	-21.6	-6.4	-3.8	-21.3	-18.0	-5.9	-2.3

Table 5.5: Flexural strength of specimens tested at ageing time t_1 and displacement rate R_2

$t_1 - R_2$									
	CF00	HWU1	CWU1	HDU1	CDU1	HWU1	CWU1	HDS1	CDS1
Ageing time (hours)	0	2544	2688	2544	2688	2304	2376	2328	2400
Avg Strength (Mpa)	509.7	389.3	431.2	-	-	413.9	411.3	494.1	494.4
% Std. dev	6.1	4.8	6.0	-	-	8.0	3.6	6.1	1.6
% Change in flexural strength	0.0	-23.6	-15.4	-	-	-18.8	-19.3	-3.1	-3.0

Table 5.6: Flexural strength of specimens tested at ageing time t_2 and displacement rate R_2

$t_2 - R_2$									
	CF00	HWU2	CWU2	HDU2	CDU2	HWU2	CWU2	HDS2	CDS2
Ageing time (hours)	0	3294	3438	3294	3438	3054	3126	3078	3150
Avg Strength (Mpa)	509.7	403.9	425.9	477.2	493.1	414.1	411.7	488.6	502.6
% Std. dev	6.1	1.3	5.8	2.8	2.7	9.6	12.8	5.9	13.1
% Change in flexural strength	0.0	-20.8	-16.4	-6.4	-3.3	-18.8	-19.2	-4.1	-1.4

Table 5.7: Flexural strength of specimens tested at ageing time t_3 and displacement rate R_2

$t_3 - R_2$									
	CF00	HWU3	CWU3	HDU3	CDU3	HWU3	CWU3	HDS3	CDS3
Ageing time (hours)	0	4044	4188	4044	4188	3804	3876	3828	3900
Avg Strength (Mpa)	509.7	405.4	426.9	476.7	492.6	-	-	483.2	501.4
% Std. dev	6.1	6.6	14.0	3.0	4.8	-	-	9.1	2.7
% Change in flexural strength	0.0	-20.5	-16.2	-6.5	-3.4	-	-	-5.2	-1.6

Table 5.8: Experimental strains at initial failure at R_1

Ageing Condition	Experimental strain at initial failure		
	t_1	t_2	t_3
CF00	0.009		
	t_1	t_2	t_3
HWU	0.007	0.007	0.008
CWU	0.008	0.008	0.008
HDU	-	0.009	0.008
CDU	-	0.010	0.010
HWS	0.007	0.006	0.006
CWS	0.007	0.007	0.006
HDS	0.009	0.008	0.009
CDS	0.009	0.006	0.009

Table 5.9: Experimental strains at initial failure at R_2

Ageing Condition	Experimental strain at initial failure		
	t_1	t_2	t_3
CF00	0.010		
	t_1	t_2	t_3
HWU	0.009	0.008	0.010
CWU	0.008	0.009	0.006
HDU	-	0.011	0.008
CDU	-	0.010	0.011
HWS	0.009	0.009	-
CWS	0.008	0.008	-
HDS	0.011	0.010	0.007
CDS	0.009	0.009	0.009

CHAPTER 6

MODEL CALIBRATION AND BENCHMARKING

6.1 Modeling results

The flexure tests were modeled using NOVA-3D as discussed in chapter 4. The model was calibrated to match the experimental results as closely as possible. Various environmental conditions were simulated by modifying the values of the maximum stress and strain in the cohesive layers and bending stiffness of the beam. The simulations were performed using displacement control. Displacement boundary conditions were applied on the three center nodes of the top layer and the average reaction force was calculated. The rate of displacement is same as that used in the actual experiment.

6.1.1 Control Specimens

The flexure test on the unaged specimen was modeled in NOVA-3D and the stiffness of the beam was modified to match the slope of the experimental load deflection curve. The maximum stress and strain in the cohesive elements was adjusted to match the strength obtained from experiments, keeping the stiffness equal to that of the beam. The maximum stress and strain parameters in the cohesive layer of the unaged specimens at displacement rates R_1 and R_2 are tabulated in Tables 6.1 and 6.2 respectively. The experimental and simulated load-deflection curves for the control specimen at displacement rates 0.01 in/min and 1.00 in/min are shown in Figures 6.1 and 6.2 respectively. The figures show very good match between the slope of the

experimental and simulated load-displacement curves which indicates that the bending stiffness of the beam has been captured. The peak load and deflection at peak load also show good agreement with experimental results. The element deletion in the $[0^\circ]$ cohesive layer can be seen in Figures 6.2 and 6.4 for the two displacement rates. As the strain in the elements reaches the maximum value, the stiffness becomes zero and the elements are deleted from the model.

Table 6.1: Cohesive layer parameters for control flexure test simulation at $R_1=0.01\text{in}/\text{min}$

Ageing Condition	CF00-R_1	
Cohesive layer parameters	0°	90°
$\sigma_{\max T}$ (MPa)	1394	174
$\epsilon_{\max T}$	0.055	0.111
E_T (MPa)	171113	10578
$\sigma_{\max C}$ (MPa)	1268	219
$\epsilon_{\max C}$	0.05	0.14
E_C (MPa)	171113	10578
τ_{\max} (MPa)	110	44
γ_{\max}	0.13	0.09
G (MPa)	5712	3332

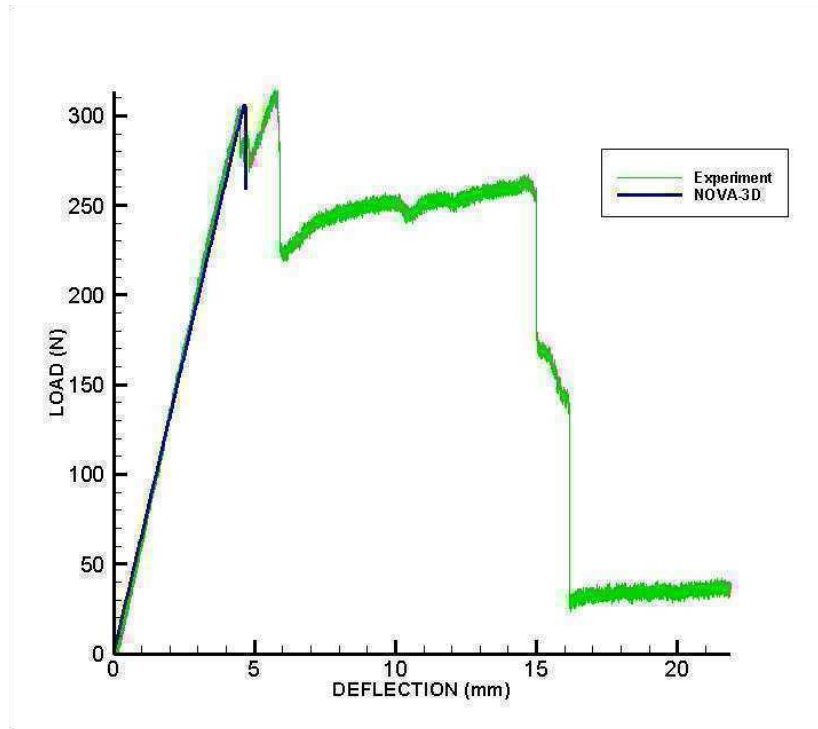


Figure 6.1: Experimental and NOVA-3D load-displacement curve for control flexure specimen at $R_1=0.01\text{in}/\text{min}$

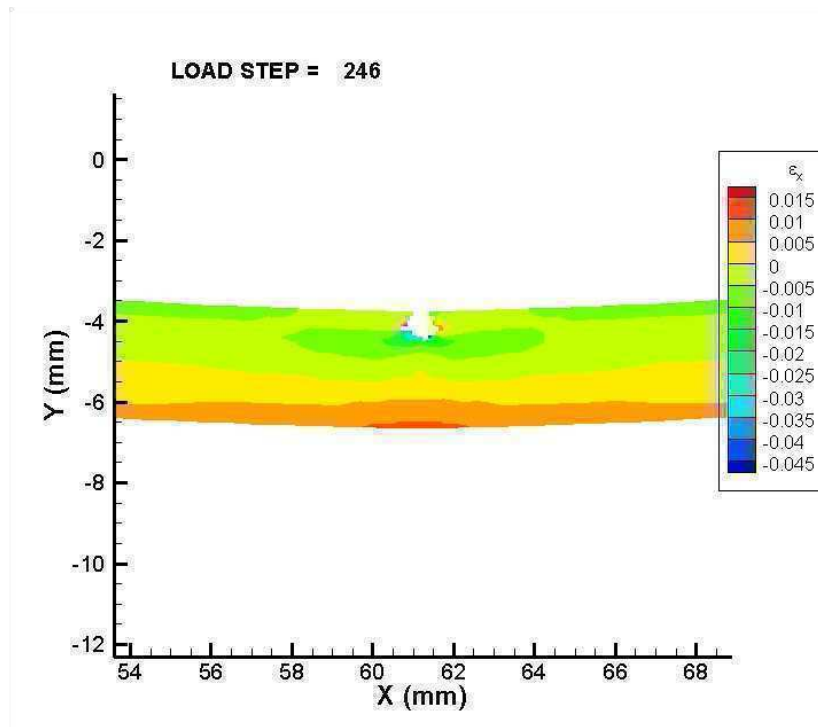


Figure 6.2: NOVA-3D contour plot for control flexure specimen at $R_1=0.01\text{in}/\text{min}$

Table 6.2: Cohesive layer parameters for control flexure test simulation at $R_2=1.00\text{in}/\text{min}$

Ageing Condition	CF00- R_2	
Cohesive layer parameters	0	90
$\sigma_{\max T}$ (MPa)	1394	174
$\epsilon_{\max T}$	0.055	0.111
E_T (MPa)	171113	10578
$\sigma_{\max C}$ (MPa)	-938	-219
$\epsilon_{\max C}$	-0.037	-0.14
E_C (MPa)	171113	10578
τ_{\max} (MPa)	110	44
γ_{\max}	0.13	0.09
G (MPa)	5712	3332

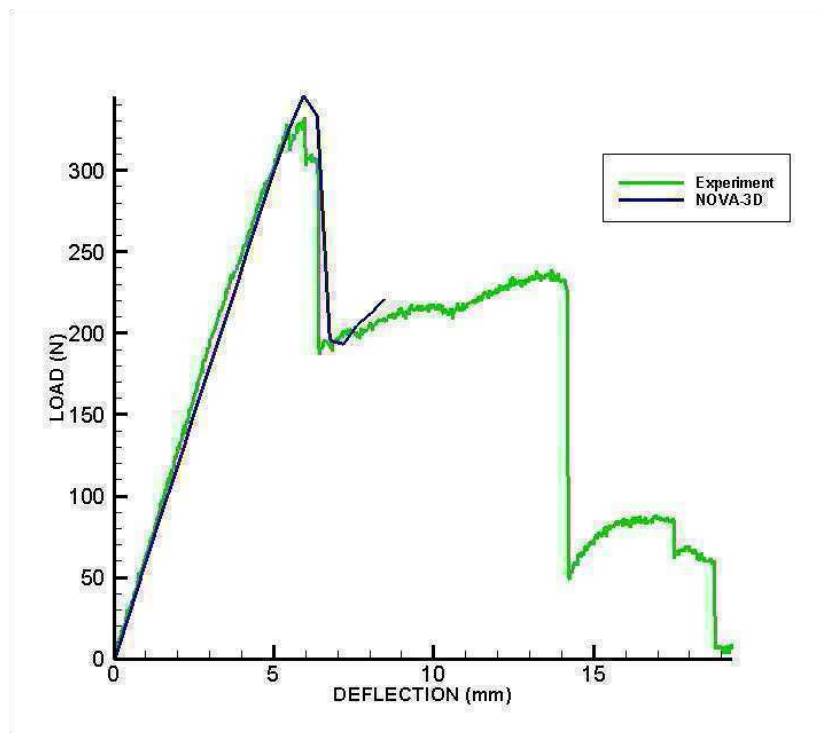


Figure 6.3: Experimental and NOVA-3D load-displacement curve for control flexure specimen at $R_2=1.00\text{in}/\text{min}$

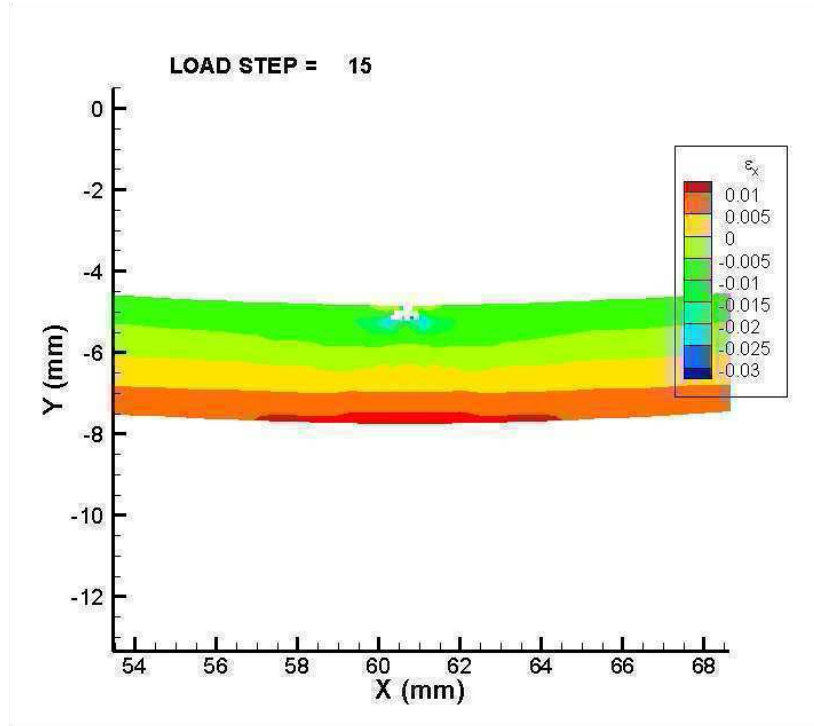


Figure 6.4: NOVA-3D contour plot for control flexure specimen at $R_1=1.00\text{in/min}$

6.1.2 Aged Specimens

The values of stress and strain in the cohesive layer for all ageing conditions at displacement rate 0.01in/min are shown in Tables 6.3 -6.5. In order to maintain a conservative approach, the stress and strain at initial failure i.e. compressive wrinkling of the outer fiber under the loading pin, was considered for the model. This implies that the input parameters of the $[0^\circ]$ cohesive layer in compression were adjusted to simulate damage initiation for each condition. The input parameters for $[90^\circ]$ layers were kept constant throughout the study. The experimental and simulated load-deflection curves for all eight ageing conditions at three time intervals at displacement rate $R_1=0.01\text{in/min}$ are shown in Figures 6.5 through 6.9.

Table 6.3: Cohesive layer parameters for ageing time ‘t₁’ for control flexure test simulation at R₁=0.01in/min

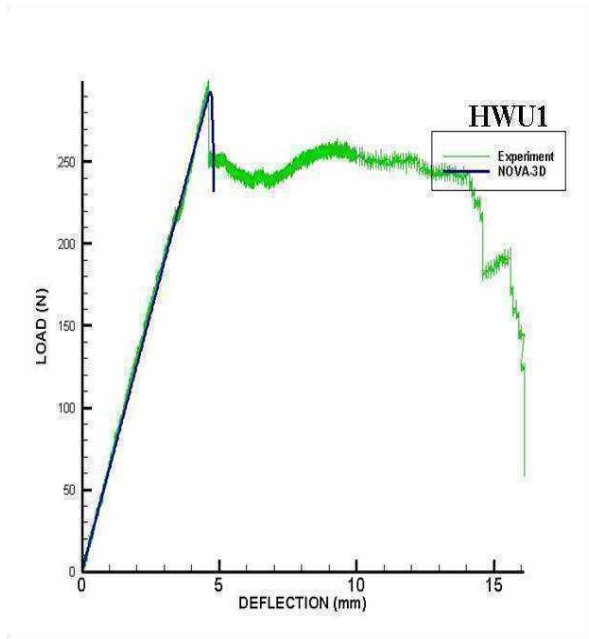
Condition	$\sigma_{\max T}$ (MPa)	$\epsilon_{\max T}$	E_T (MPa)	$\sigma_{\max C}$ (MPa)	$\epsilon_{\max C}$	E_C (MPa)	τ_{\max} (MPa)	γ_{\max}	G (MPa)
0									
HWU1	1697	0.055	208285	-1173	-0.038	208285	110	0.13	5712
CWU1	1697	0.055	208285	-1245	-0.038	221112	110	0.13	5712
HWS1	1883	0.055	231111	-1198	-0.035	231111	110	0.13	5712
CWS1	1639	0.055	201111	-1043	-0.035	201111	110	0.13	5712
HDS1	1639	0.055	201111	-1281	-0.043	201111	110	0.13	5712
CDS1	1394	0.055	171112	-1065	-0.042	171113	110	0.13	5712
90									
HWU1	174	0.111	10578	-219	-0.14	10578	44	0.09	3332
CWU1	174	0.111	10578	-219	-0.14	10578	44	0.09	3332
HWS1	174	0.111	10578	-219	-0.14	10578	44	0.09	3332
CWS1	174	0.111	10578	-219	-0.14	10578	44	0.09	3332
HDS1	174	0.111	10578	-219	-0.14	10578	44	0.09	3332
CDS1	174	0.111	10578	-219	-0.14	10578	44	0.09	3332

Table 6.4: Cohesive layer parameters for ageing time ‘t₂’ for flexure test simulation at R₁=0.01in/min

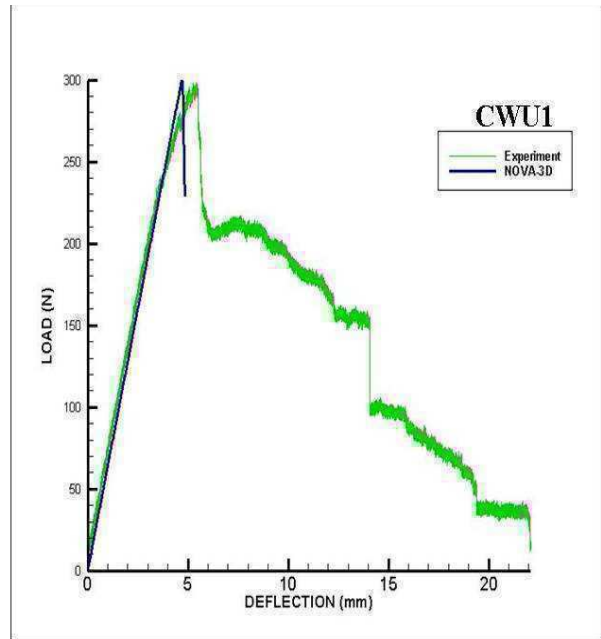
Condition	$\sigma_{\max T}$ (MPa)	$\epsilon_{\max T}$	E_T (MPa)	$\sigma_{\max C}$ (MPa)	$\epsilon_{\max C}$	E_C (MPa)	τ_{\max} (MPa)	γ_{\max}	G (MPa)
0									
HWU2	1598	0.055	196118	-1017	-0.035	196112	110	0.13	5712
CWU2	1193	0.05	161112	-1098	-0.046	161120	110	0.13	5712
HDU2	1490	0.05	201112	-1132	-0.038	201112	110	0.13	5712
CDU2	1394	0.055	171112	-1268	-0.050	171113	110	0.13	5712
HWS2	1883	0.055	231112	-1061	-0.031	231112	110	0.13	5712
CWS2	1639	0.055	201112	-1132	-0.038	201112	110	0.13	5712
HDS2	1883	0.055	231112	-1404	-0.041	231112	110	0.13	5712
CDS2	2616	0.055	321112	-1475	-0.031	321112	110	0.13	5712
90									
HWU2	174	0.111	10578	-219	-0.14	10578	44	0.09	3332
CWU2	174	0.111	10578	-219	-0.14	10578	44	0.09	3332
HWU2	174	0.111	10578	-219	-0.14	10578	44	0.09	3332
CWU2	174	0.111	10578	-219	-0.14	10578	44	0.09	3332
HWS2	174	0.111	10578	-219	-0.14	10578	44	0.09	3332
CWS2	174	0.111	10578	-219	-0.14	10578	44	0.09	3332
HDS2	174	0.111	10578	-219	-0.14	10578	44	0.09	3332
CDS2	174	0.111	10578	-219	-0.14	10578	44	0.09	3332

Table 6.5: Cohesive layer parameters for ageing time ‘t₃’ for flexure test simulation at R₁=0.01in/min

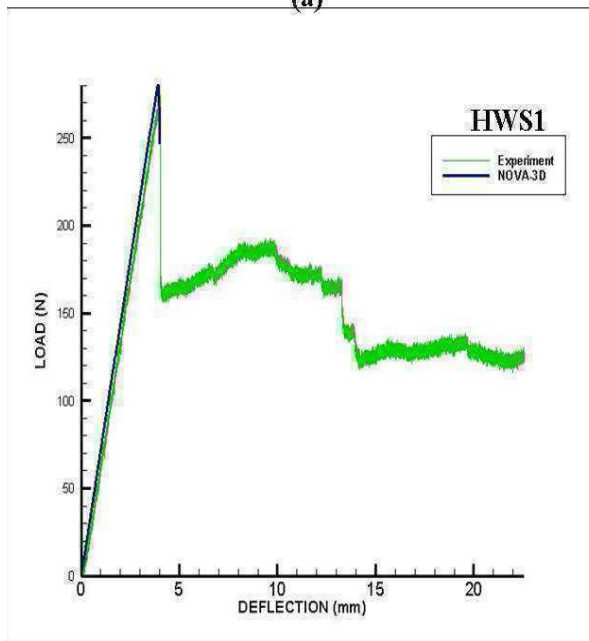
Condition	$\sigma_{\max T}$ (MPa)	$\varepsilon_{\max T}$	E_T (MPa)	$\sigma_{\max C}$ (MPa)	$\varepsilon_{\max C}$	E_C (MPa)	τ_{\max} (MPa)	γ_{\max}	G (MPa)
0									
HWU3	1598	0.055	196081	-1133	-0.039	196112	110	0.13	5712
CWU3	1476	0.055	181112	-1234	-0.046	181112	110	0.13	5712
HDU3	1490	0.05	201112	-1102	-0.037	201112	110	0.13	5712
CDU3	1557	0.055	191112	-1416	-0.050	191112	110	0.13	5712
HWS3	1476	0.055	181112	-1020	-0.038	181112	110	0.13	5712
CWS3	1802	0.055	221112	-1245	-0.038	221112	110	0.13	5712
HDS3	1883	0.055	231112	-1404	-0.041	231112	110	0.13	5712
CDS3	1802	0.055	221112	-1310	-0.040	221112	110	0.13	5712
90									
HWU3	174	0.111	10578	-219	-0.14	10578	44	0.09	3332
CWU3	174	0.111	10578	-219	-0.14	10578	44	0.09	3332
HWU3	174	0.111	10578	-219	-0.14	10578	44	0.09	3332
CWU3	174	0.111	10578	-219	-0.14	10578	44	0.09	3332
HWS3	174	0.111	10578	-219	-0.14	10578	44	0.09	3332
CWS3	174	0.111	10578	-219	-0.14	10578	44	0.09	3332
HDS3	174	0.111	10578	-219	-0.14	10578	44	0.09	3332
CDS3	174	0.111	10578	-219	-0.14	10578	44	0.09	3332



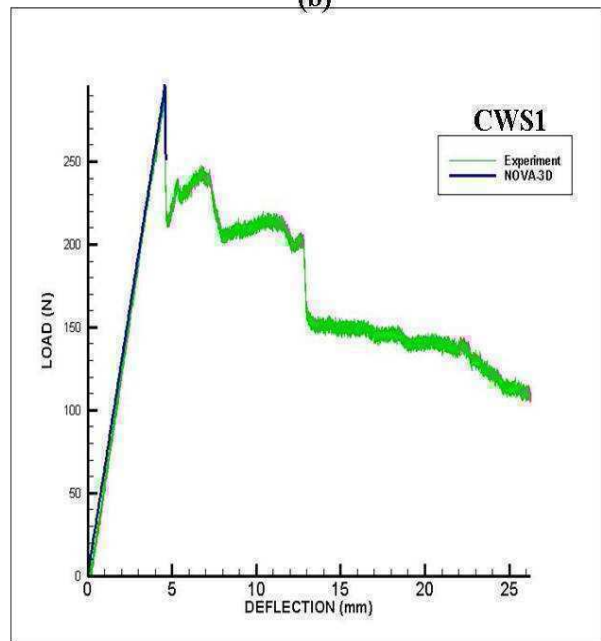
(a)



(b)



(c)



(d)

Figure 6.5: Experimental and NOVA-3D load-displacement curve for (a) HWU1 (b) CWU1 (c) HWS1 (d) CWS1 at displacement rate $R_1=0.01\text{in}/\text{min}$ for flexure test simulation

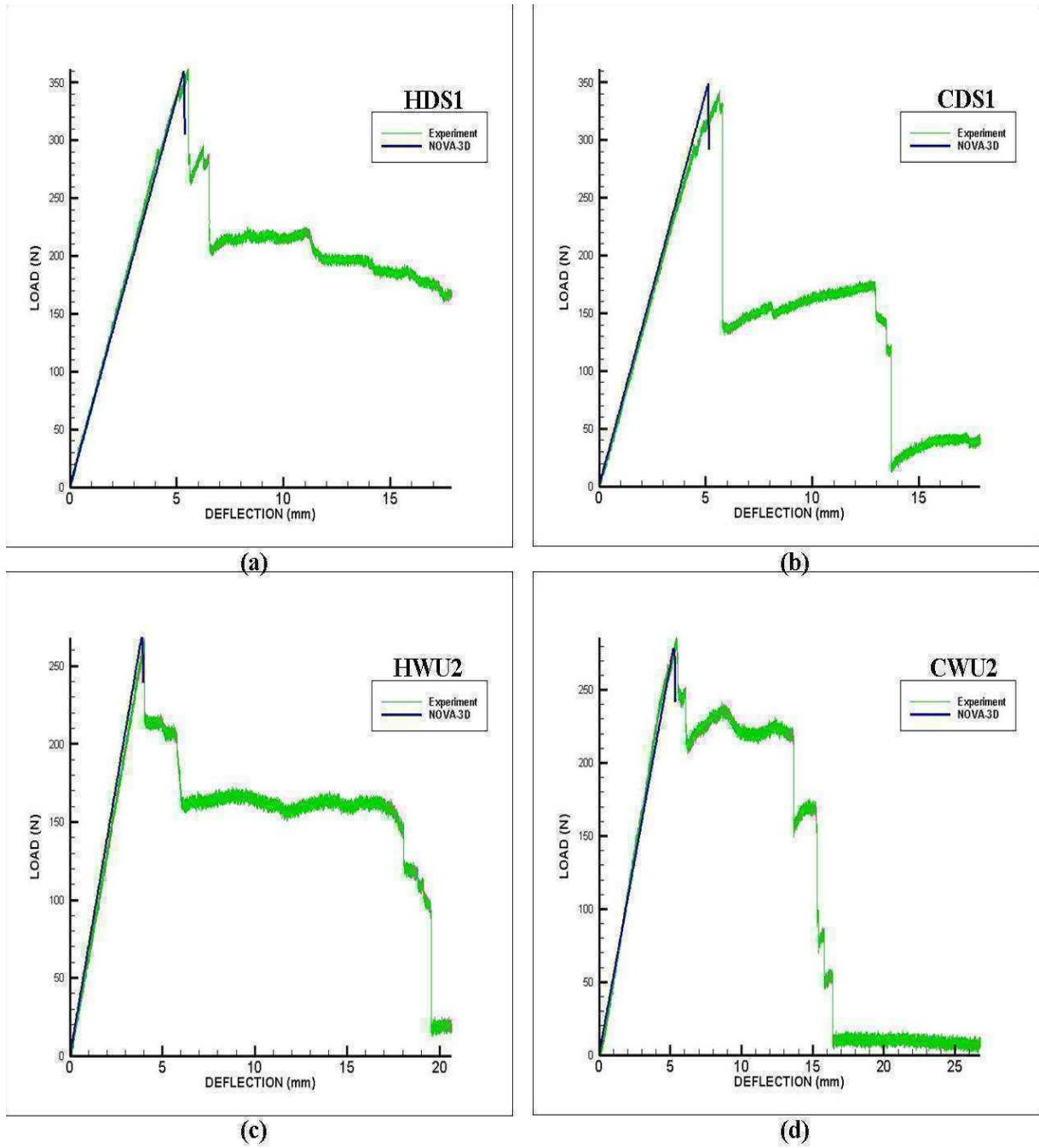


Figure 6.6: Experimental and NOVA-3D load-displacement curve for (a) HDS1 (b) CDS1 (c) HWU2 (d) CWU2 at displacement rate $R_1=0.01\text{in}/\text{min}$ for flexure test simulation

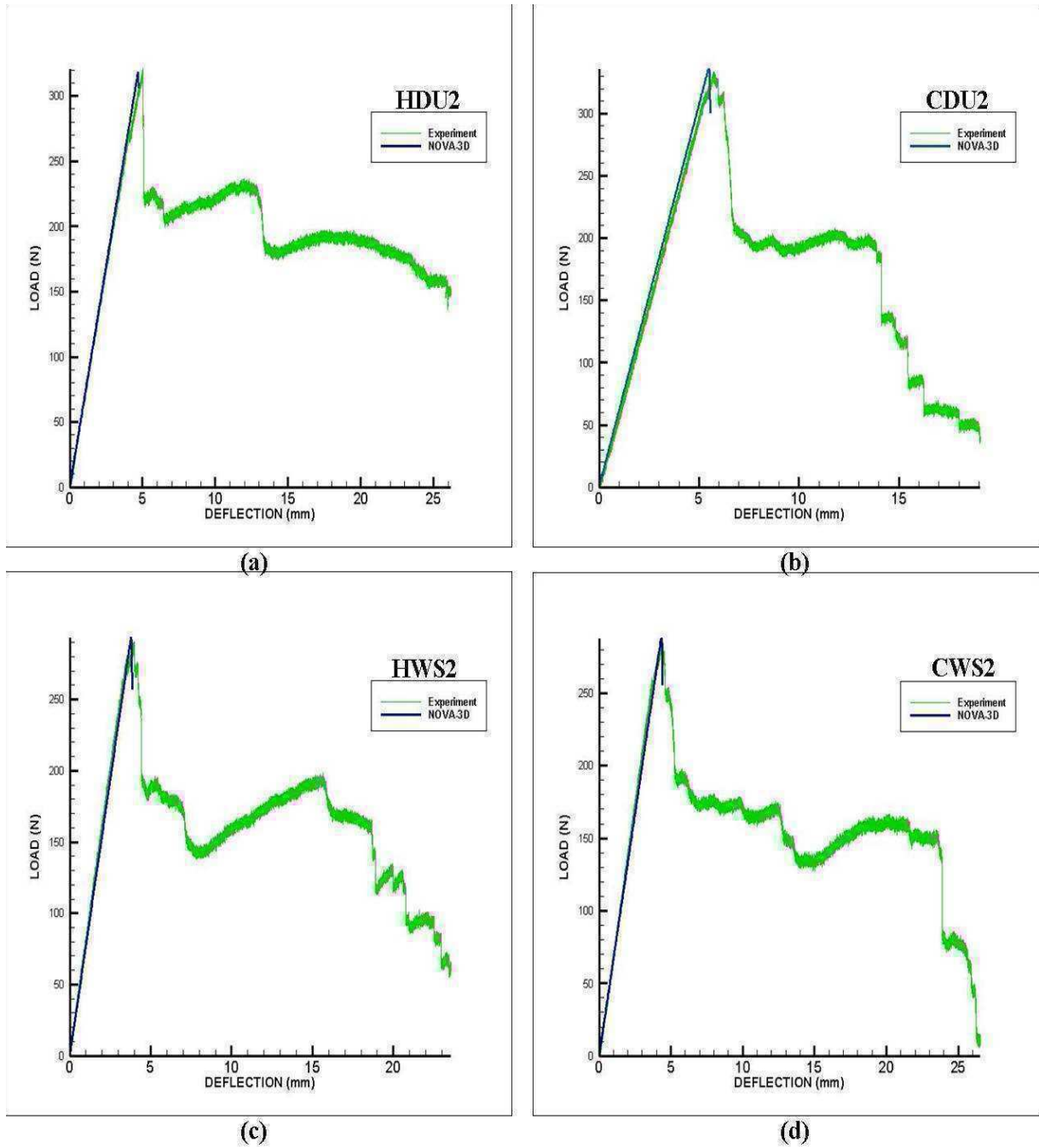


Figure 6.7: Experimental and NOVA-3D load-displacement curve for (a) HDU2 (b) CDU2 (c) HWS2 (d) CWS2 at displacement rate $R_1=0.01$ in/min for flexure test simulation

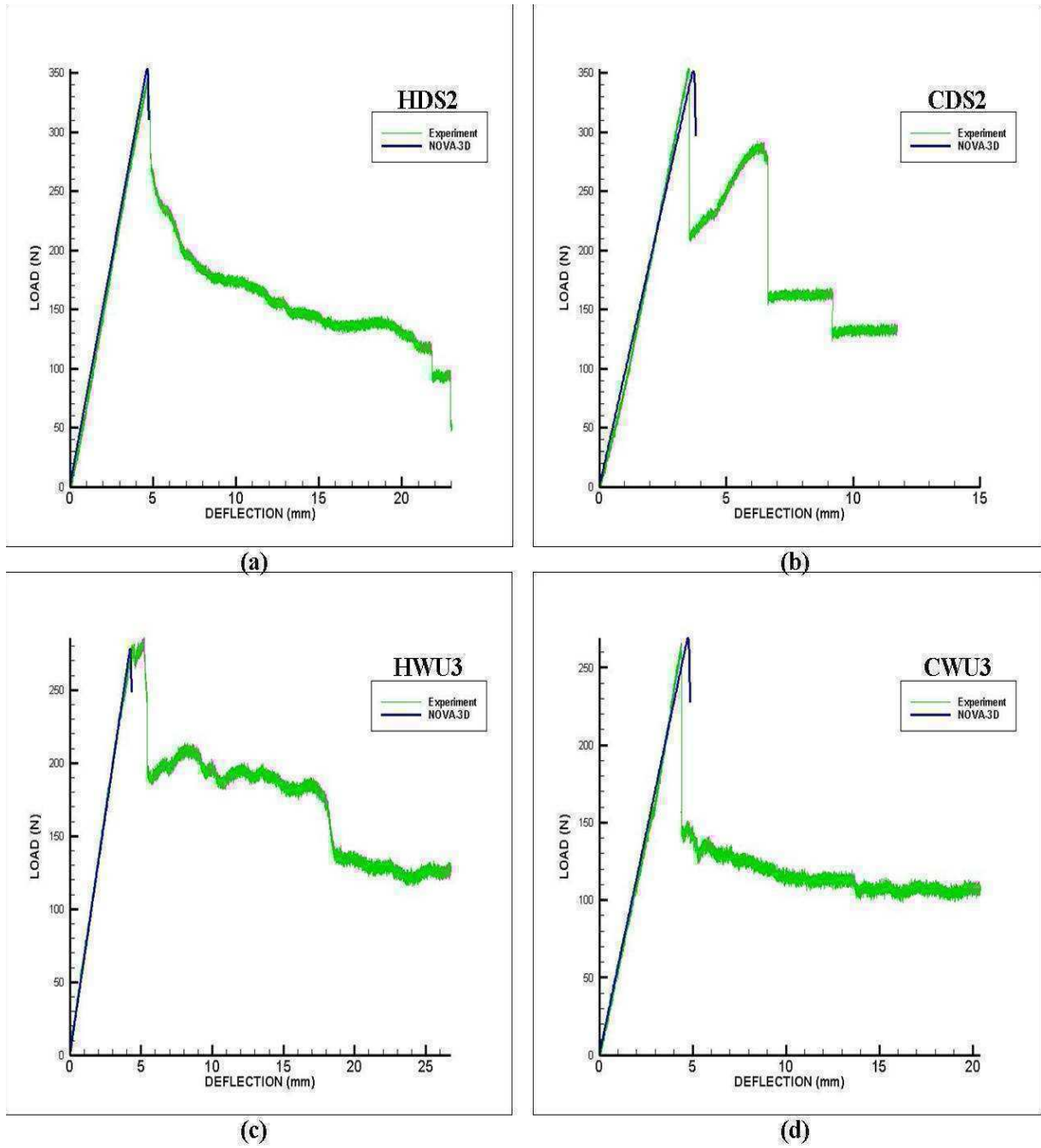


Figure 6.8: Experimental and NOVA-3D load-displacement curve for (a) HDS2 (b) CDS2 (c) HWU3 (d) CWU3 at displacement rate $R_1=0.01\text{in}/\text{min}$ for flexure test simulation

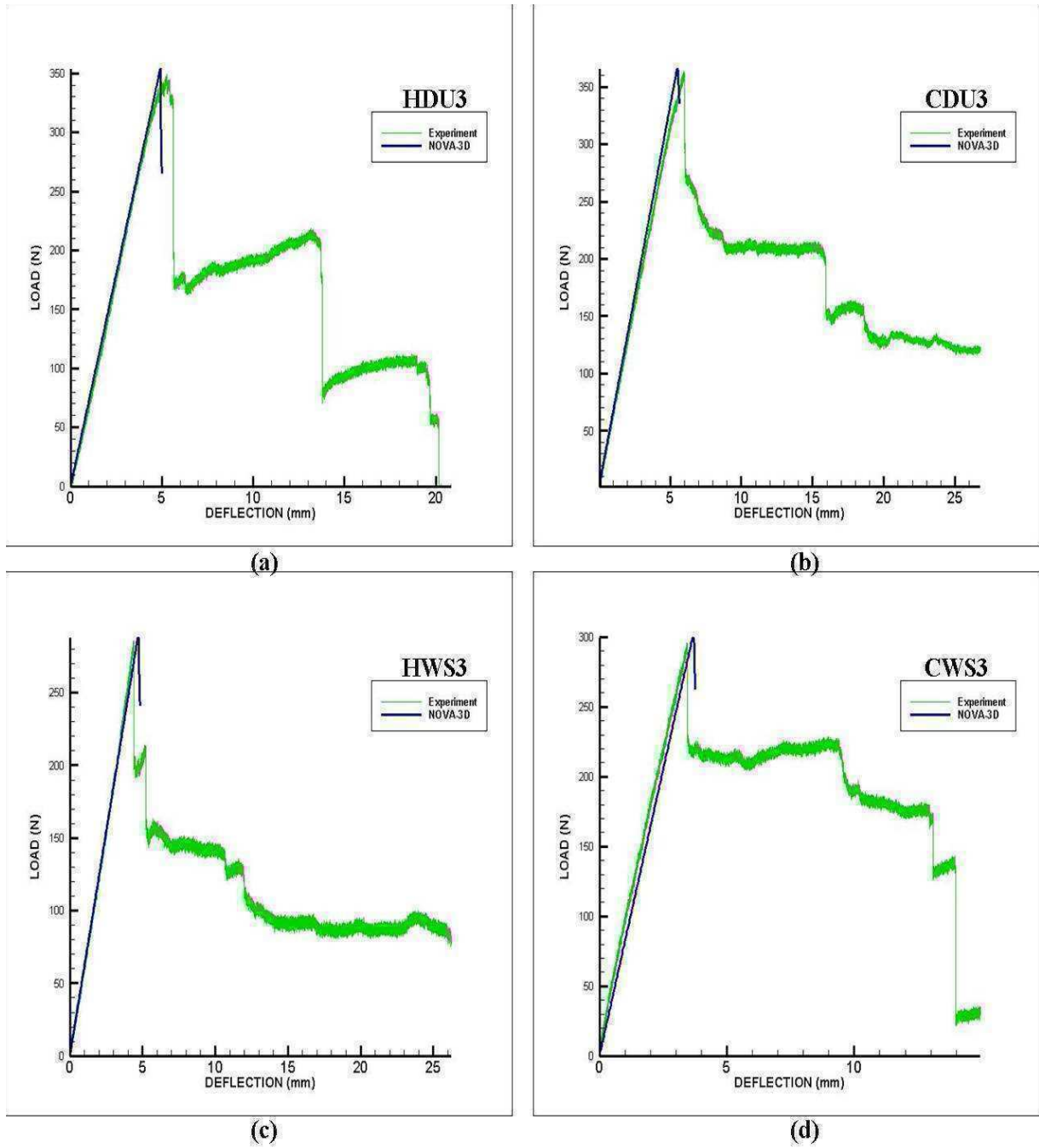


Figure 6.9: Experimental and NOVA-3D load-displacement curve for (a) HDU3 (b) CDU3 (c) HWS3 (d) CWS3 at displacement rate $R_1=0.01$ in/min for flexure test simulation

The cohesive layer parameters for the flexure tests at elevated displacement rate $R_2=1.00$ in/min are tabulated in Tables 6.6-6.8. The corresponding experimental and simulated load-deflection curves are shown in Figures 6.10 through 6.14. The simulations matched the experimental bending stiffness closely and the peak load in all cases matched within 3% error. Overall, good agreement between simulated and experimental values of bending stiffness, peak load and deflection at peak load was observed for all cases.

Table 6.6: Cohesive layer parameters for ageing time ‘t₁’ for flexure test simulation at $R_2=1.00$ in/min

Condition	$\sigma_{\max T}$ (MPa)	$\epsilon_{\max T}$	E_T (MPa)	$\sigma_{\max C}$ (MPa)	$\epsilon_{\max C}$	E_C (MPa)	τ_{\max} (MPa)	γ_{\max}	G (MPa)
0									
HWU2	1639	0.055	201112	-953	-0.032	201112	110	0.13	5712
CWU2	1639	0.055	201112	-924	-0.031	201112	110	0.13	5712
HWS2	1883	0.055	231112	-959	-0.028	231112	110	0.13	5712
CWS2	1313	0.055	161112	-764	-0.032	161112	110	0.13	5712
HDS2	1231	0.055	151111	-918	-0.041	151111	110	0.13	5712
CDS2	1394	0.055	171112	-913	-0.036	171112	110	0.13	5712
90									
HWU2	174	0.111	10578	-219	-0.14	10578	44	0.09	3332
CWU2	174	0.111	10578	-219	-0.14	10578	44	0.09	3332
HWU2	174	0.111	10578	-219	-0.14	10578	44	0.09	3332
CWU2	174	0.111	10578	-219	-0.14	10578	44	0.09	3332
HWS2	174	0.111	10578	-219	-0.14	10578	44	0.09	3332
CWS2	174	0.111	10578	-219	-0.14	10578	44	0.09	3332
HDS2	174	0.111	10578	-219	-0.14	10578	44	0.09	3332
CDS2	174	0.111	10578	-219	-0.14	10578	44	0.09	3332

Table 6.7: Cohesive layer parameters for ageing time ‘t₂’ for flexure test simulation at R₂=1.00in/min

Condition	$\sigma_{\max T}$ (MPa)	$\epsilon_{\max T}$	E_T (MPa)	$\sigma_{\max C}$ (MPa)	$\epsilon_{\max C}$	E_C (MPa)	τ_{\max} (MPa)	γ_{\max}	G (MPa)
0									
HWU2	1394	0.055	171112	-760	-0.030	171112	110	0.13	5712
CWU2	1313	0.055	161112	-859	-0.036	161112	110	0.13	5712
HDU2	1313	0.055	161112	-835	-0.035	161112	-	-	-
CDU2	1394	0.055	171112	-1267	-0.050	171112	-	-	-
HWS2	1476	0.055	181112	-859	-0.032	181112	110	0.13	5712
CWS2	1150	0.055	141112	-669	-0.032	141112	110	0.13	5712
HDS2	1313	0.055	161112	-1002	-0.042	161112	110	0.13	5712
CDS2	1639	0.055	201112	-924	-0.031	201112	110	0.13	5712
90									
HWU2	174	0.111	10578	-219	-0.14	10578	44	0.09	3332
CWU2	174	0.111	10578	-219	-0.14	10578	44	0.09	3332
HWU2	174	0.111	10578	-219	-0.14	10578	44	0.09	3332
CWU2	174	0.111	10578	-219	-0.14	10578	44	0.09	3332
HWS2	174	0.111	10578	-219	-0.14	10578	44	0.09	3332
CWS2	174	0.111	10578	-219	-0.14	10578	44	0.09	3332
HDS2	174	0.111	10578	-219	-0.14	10578	44	0.09	3332
CDS2	174	0.111	10578	-219	-0.14	10578	44	0.09	3332

Table 6.8: Cohesive layer parameters for ageing time ‘t₃’ for flexure test simulation at R₂=1.00in/min

Condition	$\sigma_{\max T}$ (MPa)	$\epsilon_{\max T}$	E_T (MPa)	$\sigma_{\max C}$ (MPa)	$\epsilon_{\max C}$	E_C (MPa)	τ_{\max} (MPa)	γ_{\max}	G (MPa)
0									
HWU2	1313	0.055	161112	-764	-0.032	161112	110	0.13	5712
CWU2	1476	0.055	181112	-537	-0.020	181112	110	0.13	5712
HDU2	1557	0.055	191112	-906	-0.032	191112	110	0.13	5712
CDU2	1394	0.055	171112	-1166	-0.046	171112	110	0.13	5712
HDS2	1883	0.055	231112	-856	-0.025	231112	110	0.13	5712
CDS2	1639	0.055	201112	-1192	-0.040	201112	110	0.13	5712
90									
HWU2	174	0.111	10578	-219	-0.14	10578	44	0.09	3332
CWU2	174	0.111	10578	-219	-0.14	10578	44	0.09	3332
HWU2	174	0.111	10578	-219	-0.14	10578	44	0.09	3332
CWU2	174	0.111	10578	-219	-0.14	10578	44	0.09	3332
HDS2	174	0.111	10578	-219	-0.14	10578	44	0.09	3332
CDS2	174	0.111	10578	-219	-0.14	10578	44	0.09	3332

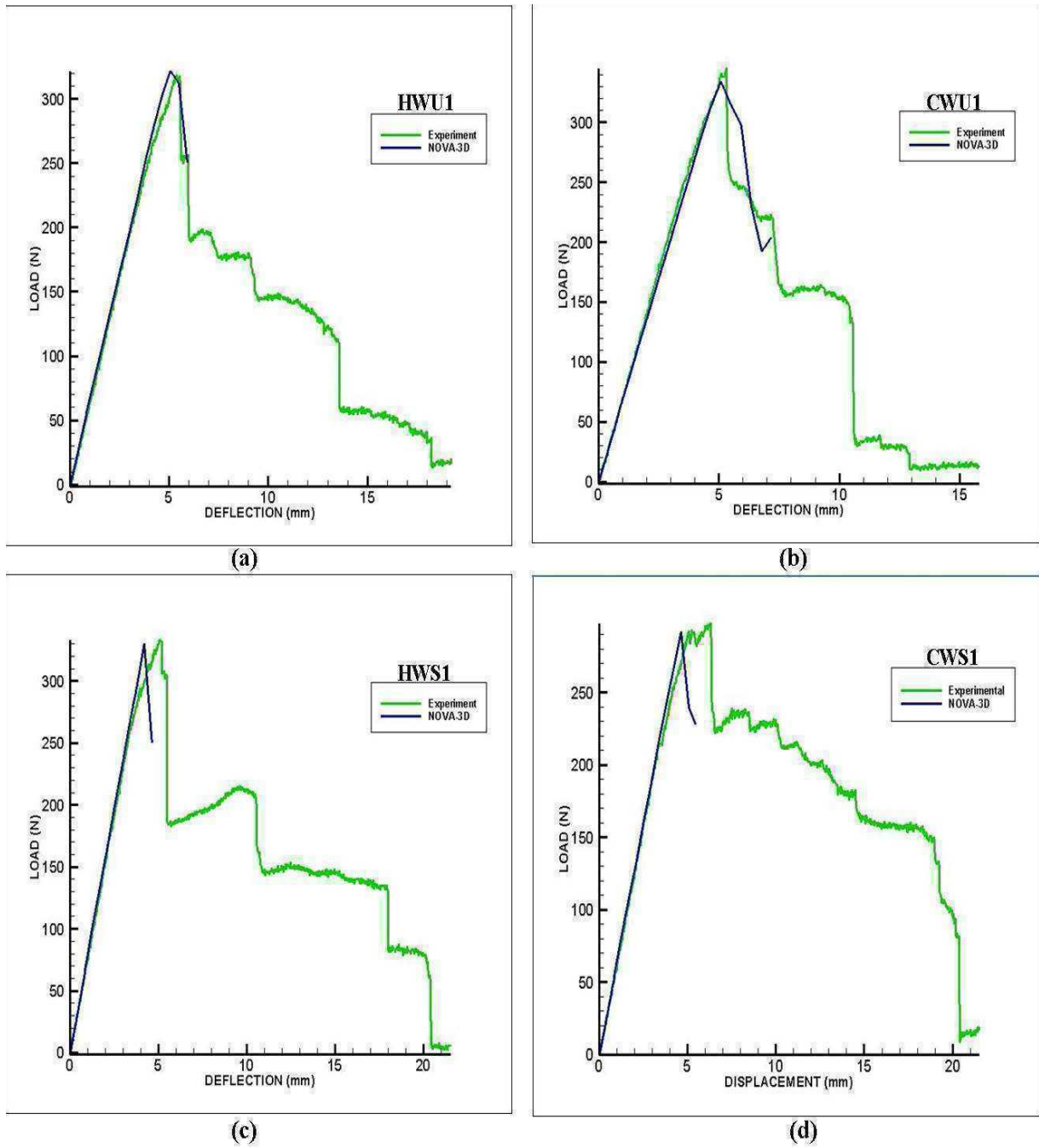


Figure 6.10: Experimental and NOVA-3D load-displacement curve for (a) HWU1 (b) CWU1 (c) HWS1 (d) CWS1 at displacement rate $R_2=1.00$ in/min for flexure test simulation

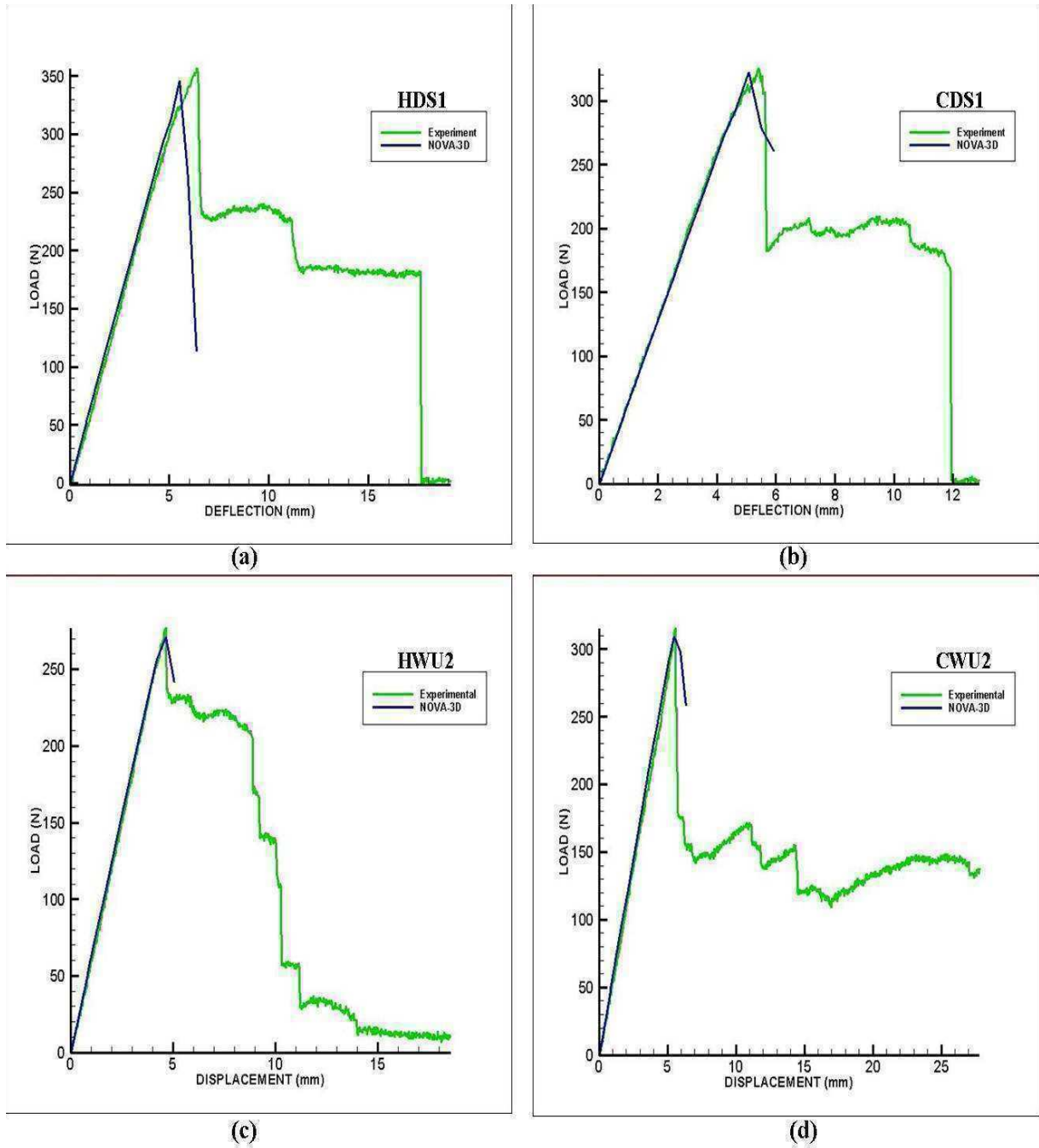


Figure 6.11: Experimental and NOVA-3D load-displacement curve for (a) HDS1 (b) CDS1 (c) HWU2 (d) CWU2 at displacement rate $R_2=1.00\text{in}/\text{min}$ for flexure test simulation

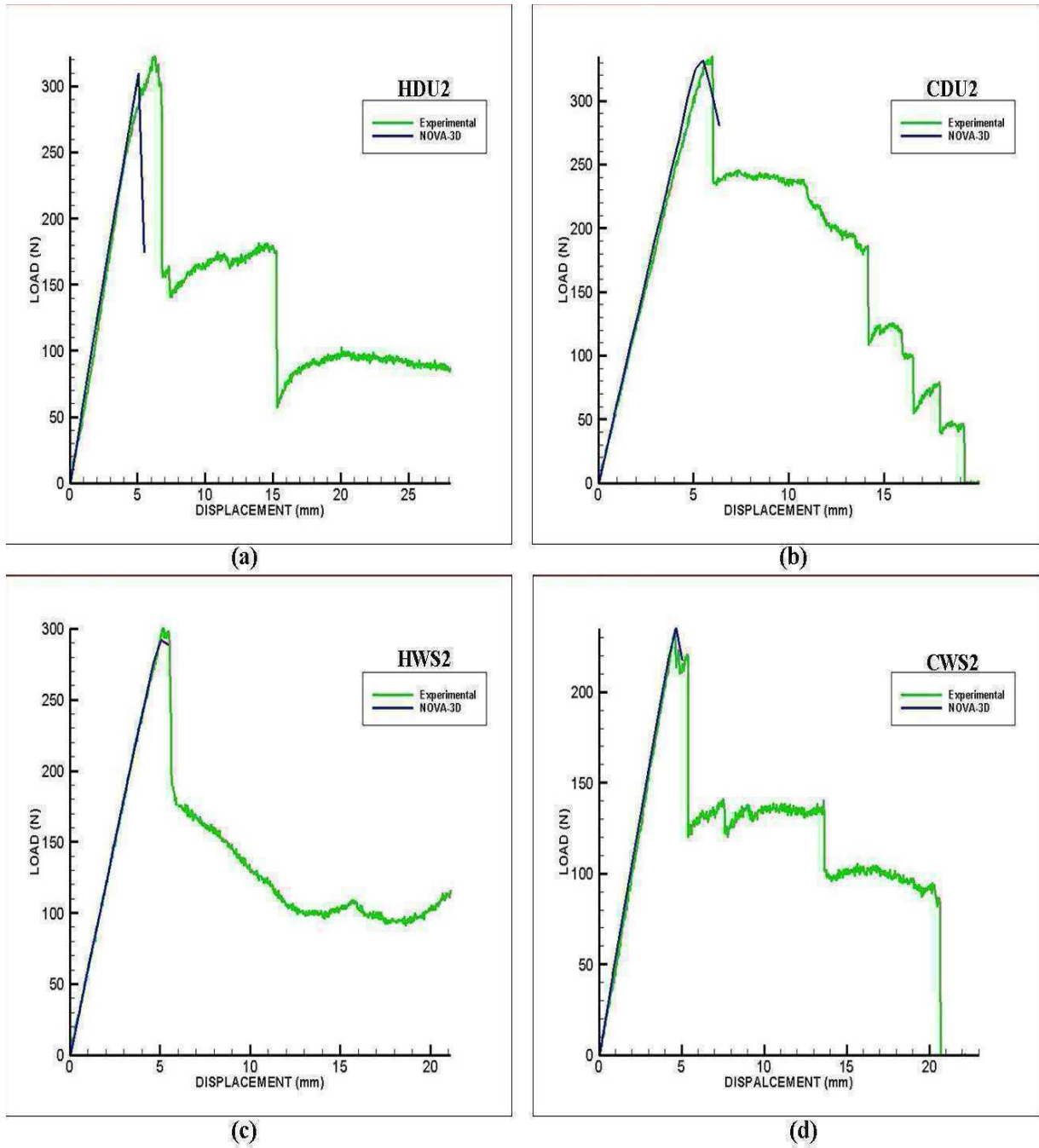


Figure 6.12: Experimental and NOVA-3D load-displacement curve for (a) HDU2 (b) CDU2 (c) HWS2 (d) CWS2 at displacement rate $R_2=1.00$ in/min for flexure test simulation

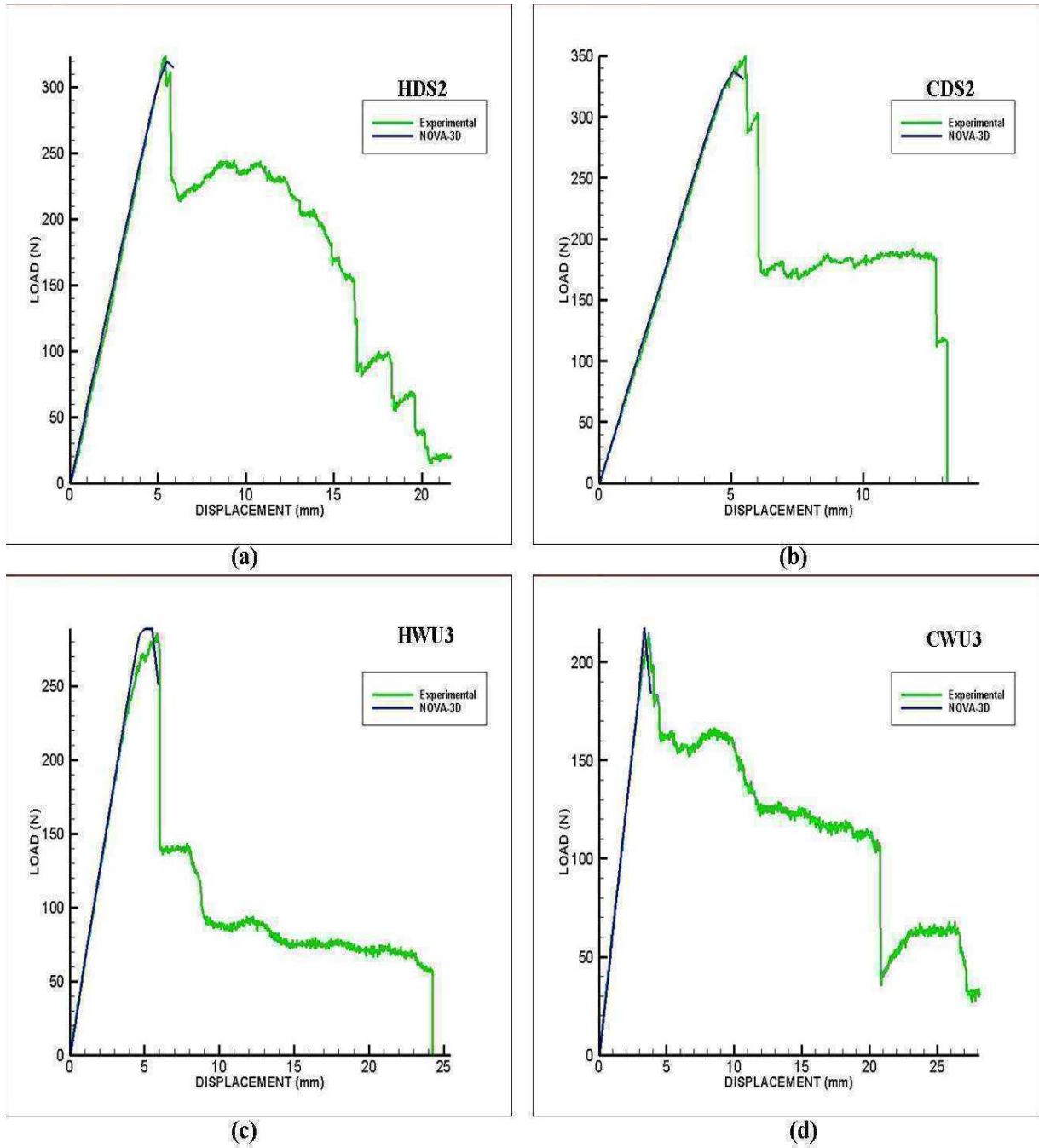


Figure 6.13: Experimental and NOVA-3D load-displacement curve for (a) HDS2 (b) CDS2 (c) HWU3 (d) CWU3 at displacement rate $R_2=1.00$ in/min for flexure test simulation

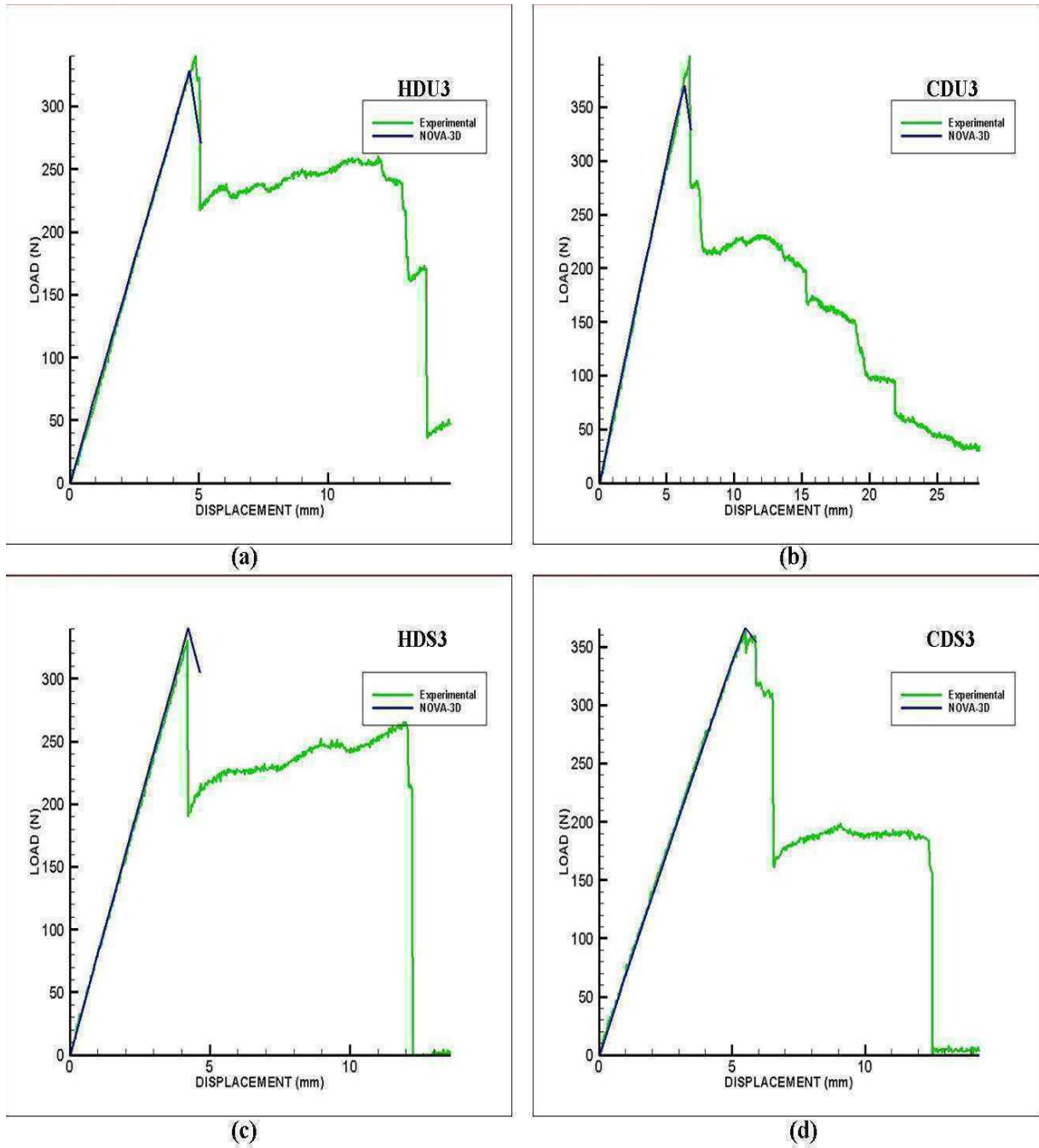


Figure 6.14: Experimental and NOVA-3D load-displacement curve for (a) HDU3 (b) CD3 (c) HDS3 (d) CDS3 at displacement rate $R_2=1.00$ in/min for flexure test simulation

6.2 Results and Discussion

The experimental and simulated values of displacement for tests at displacement rate $R_1=0.01\text{in/min}$ are tabulated in Table 6.9 and at displacement rate $R_2=1.00\text{in/min}$ in Table 6.10. The average error in displacements for both cases is 6% and 5% respectively.

Table 6.9: Comparison of experimental and NOVA-3D deflection at peak load for flexure test simulation at $R_1=0.01\text{in/min}$

Ageing Condition	Experimental deflection (mm)			NOVA-3D deflection (mm)			Percentage Error		
	t_1	t_2	t_3	t_1	t_2	t_3	t_1	t_2	t_3
CF00	4.430			4.610			4.06		
HWU	-4.56	-4.02	-4.35	-4.65	-3.90	-4.21	2.09	-2.99	-3.22
CWU	-5.36	-5.35	-4.30	-4.66	-5.15	-4.72	-13.14	-3.68	9.77
HDU	-	-5.03	-5.16	-	-4.60	-4.90	-	-8.55	-5.04
CDU	-	-5.68	-5.98	-	-5.47	-5.43	-	-3.66	-9.20
HWS	-4.00	-3.98	-4.32	-3.92	-3.75	-4.71	-2.00	-5.78	9.05
CWS	-4.51	-4.37	-3.42	-4.57	-4.27	-3.65	1.33	-2.29	6.73
HDS	-5.45	-4.72	-5.37	-5.29	-4.60	-4.67	-2.94	-2.54	-13.04
CDS	-5.53	-3.53	-5.15	-5.06	-3.66	-4.42	-8.55	3.68	-14.17

Table 6.10: Comparison of experimental and NOVA-3D deflection at peak load for flexure test simulation at $R_2=1.00\text{in/min}$

Ageing Condition	Experimental deflection (mm)			NOVA-3D deflection (mm)			Percentage Error		
	t_1	t_2	t_3	t_1	t_2	t_3	t_1	t_2	t_3
CF00	5.400			5.900			9.26		
HWU	-5.50	-4.63	-5.81	-5.04	-4.63	-5.47	-8.36	0.00	-5.85
CWU	-5.30	-5.55	-3.68	-5.06	-5.50	-3.32	-4.53	-0.90	-9.78
HDU	-	-6.24	-4.85	-	-5.00	-4.59	-	-19.87	-5.36
CDU	-	-5.95	-6.66	-	-5.43	-6.24	-	-8.74	-6.31
HWS	-5.14	-5.24	-	-5.18	-5.04	-	0.78	-3.82	-
CWS	-5.05	-4.58	-	-4.58	-4.56	-	-9.31	-0.44	-
HDS	-6.37	-5.39	-4.15	-6.34	-5.41	-4.18	-0.47	0.37	0.72
CDS	-5.41	-5.44	-5.46	-5.06	-5.02	-5.48	-6.47	-7.72	0.37

The experimental and simulated loads at low and elevated displacement rates are shown in Tables 6.11 and 6.12. The average error in load for all ageing conditions was approximately 1.58% and 3% respectively. This shows that the model has successfully been able to predict the maximum load and deflection at initial failure for flexure specimens at all ageing conditions.

Table 6.11: Comparison of experimental and NOVA-3D peak load of flexure test simulation at $R_1=0.01\text{in/min}$

Ageing Condition	Experimental Load (N)			NOVA-3D Load (N)			Percentage Error		
	t_1	t_2	t_3	t_1	t_2	t_3	t_1	t_2	t_3
CF00	301.19			305.36			1.39		
HWU	294.20	264.20	279.20	292.48	268.26	278.50	-0.58	1.54	-0.25
CWU	293.04	280.75	260.20	299.91	278.40	269.50	2.34	-0.84	3.57
HDU	-	317.00	342.57	-	315.00	354.10	-	-0.63	3.37
CDU	-	326.55	360.11	-	335.70	366.11	-	2.80	1.67
HWS	271.90	287.65	282.90	280.38	293.50	288.00	3.12	2.03	1.80
CWS	287.06	284.76	291.89	296.25	287.67	299.83	3.20	1.02	2.72
HDS	359.60	349.40	259.74	359.06	353.60	269.36	-0.15	1.20	3.70
CDS	335.36	350.94	327.15	347.74	351.51	325.45	3.69	0.16	-0.52

Table 6.12: Comparison of experimental and NOVA-3D peak load of flexure test simulation at $R_2=1.00\text{in/min}$

Ageing Condition	Experimental Load (N)			NOVA-3D Load (N)			Percentage Error		
	t_1	t_2	t_3	t_1	t_2	t_3	t_1	t_2	t_3
CF00	329.00			343.00			4.40		
HWU	318.42	277.34	286.64	321.97	270.15	289.54	1.11	-2.59	1.01
CWU	345.55	315.16	214.18	332.20	306.67	217.36	-3.86	-2.69	1.48
HDU	-	323.78	340.22	-	304.36	326.73	-	-6.00	-3.97
CDU	-	335.87	340.53	-	331.60	370.22	-	-1.27	8.72
HWS	333.12	300.92	-	328.43	291.87	-	-1.41	-3.01	-
CWS	308.65	235.01	-	291.39	235.37	-	-5.59	0.15	-
HDS	357.76	324.23	330.42	342.17	319.65	332.40	-4.36	-1.41	0
CDS	346.53	350.04	363.11	320.21	336.32	366.00	-7.60	-3.92	0.80

The values of experimental strains at initial failure and strains in cohesive elements at initial failure are tabulated in Tables 6.13 and 6.14. It must be noted that the NOVA-3D strain is the value at which damage initiates in the cohesive elements and is equal to $\frac{1}{3}\epsilon_{maxC}$ for the outermost [0] layer in compression. For example in Figure 6.15, damage initiates at point b, i.e. when $\epsilon = 0.0167$ and this value is compared to the experimental strain at initial failure. As seen in Tables 6.13 and 6.14, the error in experimental and simulated strains is very large. This error is attributed to the fact that there are localized strains present below the loading pin which are not taken into consideration when the experimental strains are calculated using the formula

$$\epsilon_{xC}^{(k)} = -\frac{PLh}{8bD_{11}} .$$

The NOVA-3D model, however, accounts for these stress concentrations and thus requires a higher cohesive element strain to match the experimental load-deflection curve.

In addition, in all cases, the simulation over-predicts the strains.

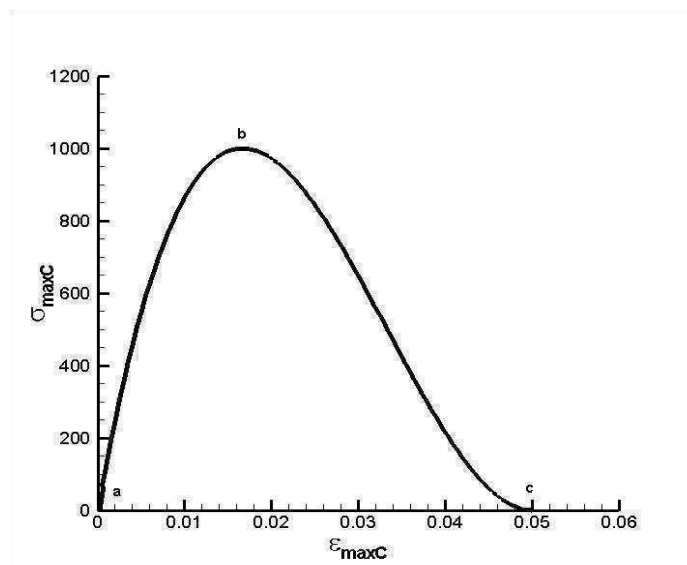


Figure 6.15: Cohesive traction separation law

Table 6.13: Comparison of Experimental and NOVA-3D strains at initial failure of flexure test simulation at $R_1=0.01\text{in/min}$

Ageing Condition	Experimental Strain			NOVA-3D Strain			Percentage Error		
CF00	-0.009			-0.017			79.92		
	t_1	t_2	t_3	t_1	t_2	t_3	t_1	t_2	t_3
HWU	-0.007	-0.007	-0.008	-0.013	-0.012	-0.013	89.39	73.95	73.23
CWU	-0.008	-0.008	-0.008	-0.013	-0.015	-0.015	59.15	82.59	103.12
HDU	-	-0.009	-0.008	-	-0.013	-0.012	-	47.63	53.02
CDU	-	-0.010	-0.010	-	-0.017	-0.017	-	72.09	63.40
HWS	-0.007	-0.006	-0.006	-0.012	-0.010	-0.013	74.40	62.81	95.89
CWS	-0.007	-0.007	-0.006	-0.012	-0.013	-0.013	63.91	74.75	110.80
HDS	-0.009	-0.008	-0.009	-0.014	-0.014	-0.014	59.63	76.34	53.06
CDS	-0.009	-0.006	-0.009	-0.014	-	-0.013	48.93	-	56.61

Table 6.14: Comparison of Experimental and NOVA-3D strains at initial failure of flexure test simulation at $R_2=1.00\text{in/min}$

Ageing Condition	Experimental Strain			NOVA-3D Strain			Percentage Error		
CF00	-0.010			-0.012			18.47		
	t_1	t_2	t_3	t_1	t_2	t_3	t_1	t_2	t_3
HWU	-0.009	-0.008	-0.010	-0.011	-0.010	-0.011	25.35	26.58	9.40
CWU	-0.008	-0.009	-0.006	-0.010	-0.012	-0.007	33.98	39.18	20.69
HDU	-	-0.011	-0.008	-	-0.012	-0.011	-	8.20	35.16
CDU	-	-0.010	-0.011	-	-0.017	-0.015	-	59.64	40.55
HWS	-0.009	-0.009	-	-0.009	-0.011	-	7.83	25.30	-
CWS	-0.008	-0.008	-	-0.011	-0.011	-	29.81	35.98	-
HDS	-0.011	-0.010	-0.007	-0.014	-0.014	-0.008	25.35	35.76	15.34
CDS	-0.009	0.009	-0.009	-0.012	-0.010	-0.013	32.95	10.12	45.87

CHAPTER 7

SUMMARY AND CONCLUSIONS

Carbon/epoxy cross-ply panels of $[0_2/90_2]_{2s}$ configuration used for the research work were manufactured using VARTM process. These panels were aged in different aggressive environmental conditions over a period of four to seven months to study the synergistic effect of temperature, moisture and stress on the flexure strength. The specimens were stressed at 5% UTS using a unique constant strain fixture while simultaneously undergoing hygrothermal ageing. During ageing, the panels immersed in water were weighed periodically to track the moisture absorption. At time intervals t_1 , t_2 , t_3 the panels were cut and the test specimens were tested at two displacement rates, 0.01in/min and 1.00in/min. The test results were analyzed to study the reduction in flexural strength of the cross-ply specimens as a result of accelerated degradation due to environment.

Finite element analysis was performed using cohesive elements along the probable failure path to track the mode of failure and failure strength. The analysis was performed in NOVA-3D using FORTRAN. The model was successfully able to predict the load and deflection at initial failure of flexure specimens under three-point bend configuration. Environmental effects were incorporated in the model by calibrating the cohesive element parameters and the bending stiffness of the beam.

7.1 Experimental Conclusions

An extensive array of tests was performed on flexure specimens aged at different environmental conditions. The tests showed a progressive failure pattern of the cross-ply specimens with initial failure due to compressive fiber wrinkling on the outer surface under the loading pin, second failure due to matrix cracks in the centre [90] layers and delaminations and final failure was due to fiber breakage on the tensile surface. The stress-strain plots obtained from these tests showed that moisture plays a key role in the degradation and loss of load carrying capacity of carbon/epoxy panels. While the strength degradation due to hygrothermal effects was approximately 26% in hot/wet/unstressed case and 22% in cold/wet/unstressed case, it was approximately 22% in hot/wet/stressed and 19% in cold/wet/stressed condition. The specimens under thermo-oxidative environment degraded between 2% to 6% which indicates that temperature does not cause significant degradation in the laminates. Stress did not have a significant effect on the degradation of the specimens.

Maximum change in strength was observed at time period ' t_1 ' i.e. upon saturation of the wet specimens. Thereafter, the moisture absorption in the panels remained constant and they did not show any further degradation in strength.

The specimens tested at elevated displacement rate showed consistently higher flexural strength compared to the tests at low displacement rate. The strength is approximately 5% higher at elevated displacement rate. The degradation mechanism in both cases showed progressive failure with compressive wrinkling on the top surface causing initial failure, delamination and matrix cracking and final failure due to fiber failure on the tensile surface.

7.2 Modeling Conclusions

The model was able to successfully capture the synergistic effect of environment and preloading on the flexural strength of carbon/epoxy composites and predicted the peak load and deflection at peak load for the various environmental conditions. Only initial failure due to fiber wrinkling was modeled to maintain a conservative approach in predicting the life of the specimen. The average error between the experimental and simulated peak load was approximately 1.58% while that between deflections at peak load was 8%.

The failure was modeled by adjusting the values of maximum stress and strain in the cohesive layer. A large error is observed between the strain values obtained from experiments and the cohesive failure strain used in the analysis. This has been attributed to the fact that during simulations, load is applied at three nodes which leads to a stress concentration which are similar to those in experiments. However, the experimental calculation for strain does not allow calculation of strain concentrations under the loading pin due to which the initial failure occurs. As a result, the values of strain used in the simulation are much larger than those observed in the experiments. This anomaly could have been avoided through the use of four-point bend loading. However, due to experimental and other constraints, three point bend loading was used in the work. A correlation between the NOVA-3D strains and the experimental strain has yet to be determined.

7.3 Summary

Synergistic effect of hygrothermal conditions and preloading has been observed through determination of degradation in flexural strength by three point bend loading. The stiffness and

maximum load and deflection at initial failure has been successfully captured through the use of a prescribed cubic cohesive traction-separation law modeled in NOVA-3D.

REFERENCES

- Allred, R.E., "The Effect of Temperature and Moisture Content on the Flexural Response of Kevlar/Epoxy Laminates: Part I. [0/90] Filament Orientation," *Journal of Composite Materials*, Vol. 15 No. 3, 1981, pp.100
- Almen, G. R., Byrens, R. M., MacKenzie, P. D., Maskell, R. K., McGrail, P. T., and Sefton, M. S. "977 – A family of new toughened epoxy matrices," *34th International SAMPE symposium*, Covina, CA: SAMPE, 1989, pp. 259-270
- Almen, G., MacKenzie, P., Malhotra, V., and Maskell, R. "977: Characterization of a family of new toughened epoxy resins," *35th International SAMPE Symposium, 1990*, pp. 419-431
- Asp, L. E. "The effects of moisture and temperature on the interlaminar delamination toughness of a carbon/epoxy composite," *Composites Science and Technology*, Vol. 58 (1998), pp.967-977
- Birger, S., Moshonov, A., and Kenig, S., "The effects of thermal and hygrothermal ageing on failure mechanisms of graphite-fabric epoxy composites subjected to flexural loading," *Composites*, Vol. 20, No. 4, July 1989, pp. 341-348
- Blikstad, M., Sjoblom, P.O.W., and Johannesson, T.R., *Journal of Composite Materials*, Vol.18 No. 1, 1984, pp.32
- Browning, C. E. and Hartness, j. T., *Composite materials: Testing and Design (Third Conference)*, American Society for Testing and Materials, 1974, pp. 284-302
- Browning, C.E., and Whitney, J.M., *Fillers and Reinforcements for Plastics, Advances in Chemistry Series, No. 134*, American Chemical Society, 1974, pp. 137-148
- Browning, C.E., Husman, G.E., and Whitney, J.M., "Moisture Effects in Epoxy Matrix Composites," *Composite materials: Testing and Design*, American Society for Testing and Materials, 1977, pp.481-496

- Camanho, P.P. and F.L. Matthews, "A Progressive Damage Model for mechanically Fastened Joints in Composite Laminates," *Journal of Composite Materials*, 1999, Vol. 33(24), 2248-2280
- Chang, T.J. and Bradshaw, R.J., *Journal of Composite Materials*, Vol.15 No. 11, 1981, pp.502
- Cirisciogli, P.R., *Journal of Composite Materials*, Vol. 21 No. 3, 1987, pp.225
- Demonet, C. M. "Interaction of moisture with resin matrix composites," 21st International SAMPE Technical Conference, 1989, pp. 231-238.
- Demuts, B., and Shyprykevich, P., *Composites*, Vol.15, No.1, 1984, pp. 25.
- Detassis, M., Pegoretti, A., and Migliaresi, C. "Effect of temperature and strain rate on interfacial shear stress transfer in carbon/epoxy model composites," *Composites Science and Technology*, Vol. 53 (1995), pp. 39-46
- Dewumille, B., and Bunsell, A.R., *Composites*, Vol.1, No. 35, 1983
- Dutta, P.K. 1992. "Tensile strength of unidirectional fiber composites at low temperatures." Proceedings, Sixth Japan-U.S. Conference on Composite Materials, June 22-24, Orlando, 782-792
- Dutta, P.K. 1994. "Low-temperature compressive strength of glass-fiber-reinforced polymer composites," *Journal of Offshore Mechanics and Arctic Engineering*, 116, 167-172
- Dutta, P.K., and Hui, D., 1996. "Low temperature and freeze-thaw durability of thick composites," *Composites: Part B: Engineering*, Elsevier Science Limited, Vol. 27B, No. 3/4, p. 371-379
- Fried, N., Proceedings of the Fifth Symposium on Naval Structural mechanics, Philadelphia, Pa., 8-10 May 1967
- G.H. Nie, S. Roy, P.K. Dutta, "Failure in Composite Materials due to Volumetric Expansion of Freezing Moisture," *Journal of Cold Regions Engineering*, Vol. 18, No. 4, pp. 135-154 , December 2004

Gillat, O. and Broutman, I. J. "Effect of an External Stress on Moisture Diffusion and Degradation in a Graphite-Reinforced Epoxy Laminate," ASTM STP 658, Philadelphia, PA: ASTM (1976), pp. 61-83

Hahn, H. T. "Residual Stresses in Polymer Matrix Composite Laminates," *Journal of Composite Materials*, Vol. 10 (1976), pp. 266-278

Hertz, J., *Space Shuttle Materials*, Vol. 3, Society of Aerospace materials and Process Engineers, Oct. 1970, pp. 9-16

Joshi, O., *Composites*, Vol.14, No.3, 1983, pp. 196

Massiv, V. F. and Mehan, R.L. "Effects of thermal cycling on the properties of graphite-epoxy composites," *Composite Material Testing*, ASTM STR 617 (1977), pp. 466

McKague, E.L., Jr., Halkias, J.E., and Reynolds, J.D., *Journal of Composite Materials*, Vol. 9, 1975, pp. 2-9

McKague, E.L., Jr., Reynolds, J.D., and Halkias, J.E., *ASME Journal of Engineering Materials and Technology*, Vol. 98, series H, 1976, pp. 92-95

McLaughlin, P. V. D. Jr., McShane, H. A., Cochran, R., and Armstrong-Carroll, "Effects of High Heat on the Strength and Fatigue Life of Unidirectional Polymer-Matrix Composites," *Proceedings of the ASME Aerospace and Materials Divisions*, AD Vol. 51/MD Vol. 73 (1996), pp. 427-441

Myer, M. W., Herakovich, C.t. , Milkovich, S.M. and Short, J. S. "Temperature dependence of mechanical and thermal expansion properties of T-300/5208 graphite epoxy," *Composites*, Vol. 14 3, July 1983, pp.276-280

Needleman, A., "A Continuum Model for Void Nucleation by Inclusion Debonding," *Journal of Applied Mechanics*, 1987, Vol.54, pp. 525-531

- Obst, A. W., VanLandingham, M. R., Eduljee, R. F., Gillespie, J. W., Griesheim, G. E., and Tosi, K. F. "The effect of hygrothermal cycling on the microcracking behavior of fabric laminates," *Technology Transfer in a Global Community International SAMPE Technical Conference*, Vol. 28 (1996), pp. 994-1002
- Patel, S. and Case, S. "Durability of hygrothermally aged graphite/epoxy woven composite under combined hygrothermal conditions," *International Journal of Fatigue*, Vol. 24 (2002), pp. 1295-1301
- Reifsnider, K. L. and Case, S. W. "Mechanics of Temperature-Driven Long-Term Environmental Degradation of Polymer-Based Composite Systems," *ASME Materials Division American Society of Mechanical Engineers, MD-Vol. 69-1* (1995), pp. 225-230
- Roy, S and Xu, W., "Modeling of diffusion in the presence of damage in polymer matrix composites," *International Journal of Solids and Structures*, Vol. 38 (1), pp. 115-125
- S. Roy, Y. Wang, S. Park, and K. M. Liechti, "Cohesive Layer Modeling of Time-Dependent Debond Growth in Aggressive Environments," *ASME Journal of Engineering Material and Technology*, 2006, Vol. 128, No. 1, pp 11-17
- S. Roy and J.N. Reddy, "A Finite Element Analysis of Adhesively Bonded Composite Joints with Moisture Diffusion and Delayed Failure," *Computers & Structures*, 1988, Vol.29, No. 6, pp. 1011-1031
- S. Roy, S. Singh, G. Schoeppner, "Modeling of evolving damage in high temperature polymer matrix composites subjected to thermal oxidation," *Journal of Material Science*, 2008, Vol. 43, pp.6651–6660
- S.Roy, G.H. Nie, R. Karedla, L. Dharani, "Matrix Cracking and Delamination in Orthotropic Laminates Subject to Freeze-Thaw: Model Verification", *Polymer and Polymer Composites*, 2002, Vol. 10, No.8, pp. 571-587
- S.Roy, W. Xu, S. Patel, and S. Case, "Modeling of Moisture Diffusion in the Presence of Biaxial Damage in Polymer Matrix Composite Laminates," *International Journal of Solids and Structures*, 2001, Vol. 38, issue 42-43, pp. 7627 – 7641
- S.Roy, W. Xu, S.J. Park, and K.M. Liechti "Anomalous Moisture Diffusion in Viscoelastic Polymers: Modeling and Testing", *Journal of Applied Mechanics*, Vol. 67, June 2000, pp. 391-396

- Shen, C. and Springer G.S., *Journal of Composite Materials*, Vol. 11 No. 2, 1983, pp.180
- Shen, C. and Springer, G. S. “Effects of moisture and temperature on the tensile strength of composite materials,” *Environmental Effects on Composite Materials*, Westport, CT: Technomic Publishing Company, Inc. (1981), pp. 79-93
- Shen, Chi-Hung and Springer, G.S., *Journal of Composite Materials*, Vol.0, 1976, pp. 2-20
- Shih, G.C. and Ebert, L.J., “Flexural failure mechanisms and global stress plane for unidirectional composites subjected to four point bending tests,” *Composites*, Vol. 17, 1986, pp. 309-320
- Sihna S., Tsai S. W., “Prediction of fatigue S–N curves of composite laminates by Super Mic–Mac,” *Composites: Part A*, Vol. 36, 1381–1388 (2005)
- Singh, A.K. and Singh, R.P., “Synergistic effect of mechanical loading and environmental degradation on carbon fiber reinforced composites,” *Composites Science and Technology*, 2008
- Song, Xiaolan, “Vacuum Assisted Resin Transfer Molding (VARTM):Model Development and Verification,” *Dissertation*, Virginia Polytechnic Institute and State University, 2003
- Takeda, N. and Ogihara, S. “In situ observation and probabilistic prediction of microscopic failure processes in CFRP cross-ply laminates,” *Composites Science and Technology*, 1994, Vol. 52, pp. 183-195
- Weitsman, Y. J. and Elahi, M. “Effects of Fluids on the Deformation, Strength and Durability of Polymeric Composites – An Overview,” *Mechanics of Time Dependent Materials*, Vol. 3, 2000, pp. 107-126
- Xiao, G. Z., Shanahan, M.E.R., “Irreversible effects of hygrothermal ageing on DGEBA/DDA Epoxy Resin,” *Journal of Applied Polymer Science*, Vol. 69, 1998, pp. 363–369
- Xiao, G. Z., Shanahan, M.E.R., “Water Absorption and Desorption in an Epoxy Resin with degradation,” *Journal of Polymer Science*, 1997, Vol. 35, 2659–2670

Zhang, Y., Liao, Z., and Liu, P., "Study on the behavior of accelerated ageing fabric- reinforced epoxy composites," Society for the Advancement of Material and Process Engineering, 1977, pp. 197-206

Zhou, J. and Lucas, J. P., "Hygrothermal effects of epoxy resin. Part I: the nature of water in epoxy," *Polymer*, Vol. 40 (1999), pp. 5505-5512